TOWARDS LOW TEMPERATURE SINTERING METHODS FOR DYE SENSITIZED SOLAR CELLS

by

SUKANYA MURALI

A Dissertation submitted to the

Graduate School-New Brunswick

Rutgers, The State University of New Jersey

In partial fulfillment of the requirements

for the degree of

Doctor of Philosophy

Graduate Program in Materials Science and Engineering

Written under the direction of

Dr. Dunbar P. Birnie, III

And approved by

_____

_____

_____

_____

New Brunswick, New Jersey

May, 2011

ABSTRACT OF THE DISSERTATION

TOWARDS LOW TEMPERATURE SINTERING METHODS FOR

DYE SENSITIZED SOLAR CELLS

By SUKANYA MURALI

Dissertation Director:

Dr. Dunbar P. Birnie, III

Access to economically viable renewable energy sources is essential for the development of a globally sustainable society. Solar energy has a large potential to satisfy the future need for renewable energy sources.

Dye sensitized solar cells are a third generation of photovoltaic technologies with the potential for low cost environmentally safe energy production. Commercialization of this technology requires that dye sensitized solar cells with higher efficiencies can be fabricated on flexible substrates.

The commonly used material for the anode in a Dye Sensitized Solar Cell consists of titanium dioxide nanoparticles covered with a layer of light sensitizing dye. For efficient electron transport throughout the nanoparticle network, good particle interconnections are necessary. For low temperature processing these interconnections can be achieved through a hydrothermal process. The focus of this research is to understand at a fundamental level this reaction-based sintering process.

A titanium alkoxide precursor was mixed with commercial titania nanoparticles and coated on a transparent conductive oxide substrate. The product of the hydrolysis and

condensation of the alkoxide served to connect the nanoparticles thus improving the electrical conduction of the titania electrode; this was confirmed by solar cell testing and electrochemical impedance spectroscopy.

To further understand the formation of interconnections during reactive sintering, a model system based on inert silica particles was investigated. Titanium alkoxide precursor was mixed with commercial silica particles and reacted. Three different types of silica particles were used: each with a different morphology. The silica-titania multilayers/powders were characterized using SEM, XRD and BET. The efficiency of DSSCs is higher when larger non-porous silica particles are used and thin nanocrystalline titania is coated on this superstructure. This gave insight into the locations where the reactive liquid finally goes as these reactions are carried out.

As a further extension of this study, thin layers of this same kind of silica-titania composite were obtained by spin coating a titanium alkoxide sol mixed with monosized 500nm silica particles. SEM was used to examine the morphology of the contact/neck formation. Image analysis was done to quantify the effect of key process parameters on the average neck width at 2-particle contact points.

The use of image analysis to study mixed oxide sub-monolayers in this way is the first of its kind. These observational tools and the model system approach developed in this research could be applied to many systems that are of interest for optical and mechanical applications.

ACKNOWLEDGEMENTS

I would like to express my sincere gratitude to my advisor Dr.Dunbar P.Birnie III for his guidance, support and encouragement throughout my graduate study. He gave me the freedom to pursue my research interests and shared his vast knowledge on the subject and I am very grateful for the same.

I would like to thank my committee members Dr.Aurelien Du Pasquier, Dr.Adrian B. Mann and Dr. Paolina Atanassova for their time and valuable comments on my thesis. I would especially like to thank Dr.Aurelien Du Pasquier for training me on making solar cells and allowing me to use the characterization equipment in his lab.

I would like to thank Dr. Beda Mohanty for his assistance with the AFM instrumentation. I am very grateful to Dr. Jafar Al-Sharab for the TEM analysis. I would like to thank Dr. Jennifer Czerepinski and Dr. Mustafa Tuncer for training me on the BET analyzer. Many thanks to Sau Pei Lee and Tiffany Huang for assisting with the lab experiments.

Special thanks to fellow graduate students Dr. Sarika Phadke, Dr. Judith D. Sorge, Dr. Sara Reynaud, Dr. Wojtek Tutak, Dr. Maryam Abazari, Dr. Jingjing Sun, Saquib Ahmed and Vishnuvardhanan Vijayakumar for making the Rutgers experience so wonderful.

I gratefully acknowledge the funding support I received from the Rutgers Academic Excellence Fund, the Malcolm G. McLaren fellowship, and the NSF Ceramic Composite and Optical Materials Center.

I owe a lot to my parents who have always supported my career choices. I would like to especially thank them and my parents in law and my husband for taking care of our son during the long hours I was away.

I am very grateful to be blessed with my son who inspires me to do my best everyday. It is my sincere hope that my journey will inspire him to aim higher.

TABLE OF CONTENTS

LIST OF TABLES

LIST OF FIGURES

Chapter 1

Chapter 2

Chapter 3

Chapter 4

Chapter 5

CHAPTER 1. INTRODUCTION

We get most of our energy from nonrenewable energy sources, which include the fossil fuels - oil, natural gas, and coal [1]. The increasing costs and environmental impact of these energy sources has brought greater focus on the development of renewable energy technologies using wind, hydroelectricity, biomass, geothermal and solar. Alternate energy technologies such as solar can diversify our energy supply, reduce our dependence on imported fuels, improve air quality, and offset greenhouse gas emissions.

1.1 Solar cells

Solar energy refers to the utilization of energy from the Sun. The sun's heat and light are an abundant source of energy that can be harnessed in various ways such as concentrating solar power systems, photovoltaic systems and solar heating. One of these applications, the photovoltaic system, converts sunlight into electrical energy. Photovoltaic cells are semiconductor devices that generate direct current when they are illuminated by photons. They can be used in a wide range of products, from small consumer items to large commercial solar electric systems. Photovoltaic systems have no moving parts, are modular and easily expandable. These advantages combined with the benefits of energy independence and environmental compatibility make this a very attractive technology.

Crystalline silicon PV cells are the most common photovoltaic cells in use today. They are also the earliest successful PV devices [2]. Although crystalline silicon devices have dominated the commercial marketplace for over two decades, manufacturing is

highly capital intensive, as the cells require extremely clean Si wafers and very stringent processing conditions.

The high cost of crystalline silicon has led to the development of less expensive materials such as cadmium telluride (CdTe) and copper indium (gallium) diselenide (CIGS).

Although these thin film technologies are very promising, the limited availability of indium and tellurium and toxicity issues related to cadmium are some of the challenges that need to be addressed.

Photo-electrochemical cells such as dye sensitized solar cells (DSSC) are a more cost effective alternative to p-n junction based silicon or CdTe/CIGS solar cells. They offer many advantages such as: fabrication without expensive and energy-intensive high temperature and high vacuum processes, compatibility with rigid as well as flexible substrates, easy availability of raw materials and fewer significant health and environmental issues. Lower costs of production may compensate for moderate efficiencies of dye sensitized solar cells (~11%) [3] as compared to silicon solar cells (>20%) [4]. However, to enable long-term use of Dye Sensitized Solar Cells in electricity generation, e.g., in grid-connected or stand-alone rooftop applications; significant progress in cell efficiency, stability, and lifetime are needed [5].

1.2 Background on Dye sensitized solar cells (DSSC)

Dye sensitized solar cells (or Grätzel cells) were developed by Michael Grätzel and Brian O'Regan in 1991 [6]. In contrast to the all-solid conventional semiconductor solar cells, the dye-sensitized solar cell is a photoelectrochemical cell; i.e., it uses a liquid

electrolyte or other ion-conducting phase as a charge transport medium. Unlike a silicon solar cell, the task of light absorption and charge carrier transport are separated in a DSSC. Light is absorbed by a sensitizer, which is anchored to the surface of a wide band-gap semiconductor, such as titanium dioxide. Charge separation takes place at the interface via photo-induced electron injection from the dye into the conduction band of the semiconductor. Carriers are transported in the conduction band of the semiconductor to the charge collector.

DSSCs are extremely promising because they require low cost materials and can be fabricated with cost effective approaches onto glass or flexible substrates. However a lot of challenges in commercialization of this technology remain. These include:

a. Exploring new dye photo-sensitizers with reduced HOMO–LUMO[1] gap energy which can lead to absorption of broad range of light, associated with improved photocurrent density.

b. Exploring new room temperature ionic liquids to replace electrolytes containing volatile solvents, to improve stability of the cell.

c. Developing low temperature approaches to manufacture titania electrodes onto flexible substrates.

This research work is focused on "c"; the development of low temperature sintering methods for titania electrodes to improve the stability and efficiency of flexible DSSCs.

[1] HOMO- highest occupied molecular orbital; LUMO-lowest unoccupied molecular orbital

1.3 Operating principle of a dye sensitized solar cell

In its most common form, a dye sensitized solar cell consists of a transparent conducting oxide (TCO) coated with a mesoporous semiconductor layer. As the name implies, the transparent conducting oxide allows for light transmission and electron conduction. The TCO layer is usually fluorine doped tin oxide or indium tin oxide sputtered onto a substrate such as glass or a polymer such as PET (polyethylene terephthalate).

The semiconductor layer is composed of oxide nanoparticles sintered for electronic conduction. Anatase titania is the most widely used material for the oxide layer; though other wide band gap semiconductors such as ZnO and Nb_2O_5 have been investigated [7].

Attached to the oxide particles is a monolayer of a charge transfer dye (typically a bipyridine metal complex). Photoexcitation of the dye results in the injection of an electron into the conduction band of the oxide [7]. Since only dye molecules in direct contact to the semiconductor electrode surface can separate charges and contribute to the current, a porous nanocrystalline TiO_2 electrode structure is used to increase the internal surface area of the electrode and, thus, increase the number of dye molecules adsorbed on the oxide.

The dye is regenerated by electron donation from the electrolyte, usually an organic solvent containing a redox system, such as the iodide/triiodide couple. The iodide is regenerated in turn by the reduction of triiodide at the counter electrode, the circuit being completed via electron migration through the external load [7].

The difference in the Fermi level of the oxide and the redox potential of the electrolyte corresponds to the maximum open circuit output voltage of the cell. The electron injection to the semiconductor is much faster than electron relaxation in the sensitizer, thus charge separation occurs with a high efficiency.

A schematic of the regenerative working cycle of the dye-sensitized solar cell is shown in Figure 1.1 [8]. The arrows in the schematic illustrate the direction and series of electron movement when the cell is light activated.

The incoming photon is absorbed by the dye molecule which is transformed from a molecular ground state S to an excited state S^*. The electron is injected into the conduction band of the oxide leaving the dye molecule in an oxidized state S^+. The injected electron percolates through the porous nanocrystalline structure to the transparent conducting oxide (TCO) layer of the substrate and through an external load to the counter electrode. At the counter electrode the electron is transferred to the triiodide (I_3^-) in the electrolyte to yield iodide (I^-), and the cycle is closed by reduction of the oxidized dye by the iodide (I^-) in the electrolyte [9].

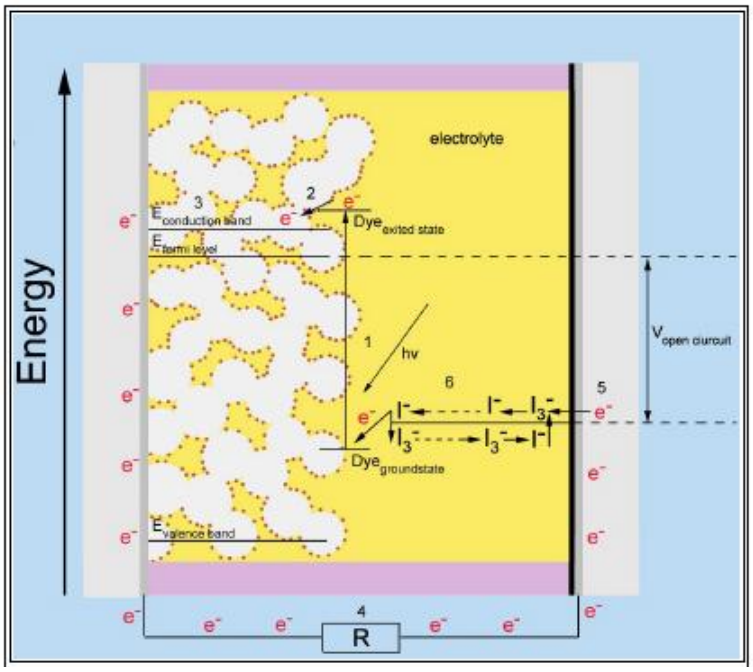

Figure 1.1: Schematic of a dye sensitized solar cell [8].

The operating cycle [10] can be summarized in chemical reaction terminology as follows:

Anode:

$$S + h\nu \rightarrow S^* \qquad \text{Absorption}$$

$$S^* \rightarrow S^+ + e^-(TiO_2) \qquad \text{Electron injection}$$

$$2S^+ + 3I^- \rightarrow 2S + I_3^- \qquad \text{Dye Regeneration}$$

Cathode:

$$I_3^- + 2\,e^-(Pt) \rightarrow 3I^- \qquad \text{Electrolyte Regeneration}$$

Cell:

$$e^-(Pt) + h\nu \rightarrow e^-(TiO_2)$$

An in-depth look at the important steps in the operating cycle of the DSSC follows:

1.3.1 Light absorption

Dye sensitizers serve as the solar energy absorber in DSSC and their properties will have a significant effect on the light harvesting efficiency and the overall photoelectric conversion efficiency [11]. The ideal sensitizer for dye-sensitized solar cells should absorb all light below a threshold wavelength of about 920 nm (or energy > 1.35eV). The dye should be firmly attached to the semiconductor oxide surface and inject electrons to the conduction band with a quantum yield (electrons injected per absorbed photon) of unity. It's redox potential should be sufficiently high so that it can be regenerated rapidly via electron donation from the electrolyte.

The best photovoltaic performance in terms of both conversion yield and long-term stability has so far been achieved with polypyridyl complexes of ruthenium and osmium [11]. The molecular structure of one such ruthenium based dye *cis*-bis(isothiocyanato)bis(2,2'-bipyridyl-4,4'-dicarboxylato)-ruthenium(II)bis-tetrabutylammonium, commonly known as "N719" is shown in Figure 1.2.

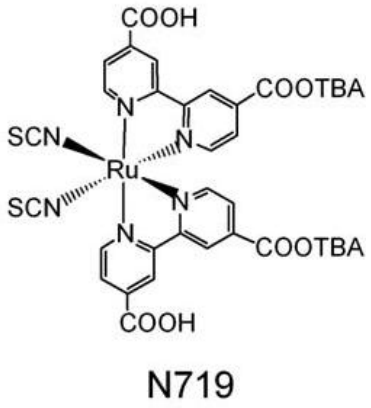

Figure 1.2: Chemical structure of "N719" dye [12].

1.3.1.1 Spectral response and IPCE (incident photon-to-current efficiency)

The spectral response of the N719 dye used in a majority of experiments in this research work is shown in Figure 1.3. The absorption maxima of the dye in an ethanolic solution are located at ~518nm and ~380nm, with the former being more important for a range of visible wavelengths.

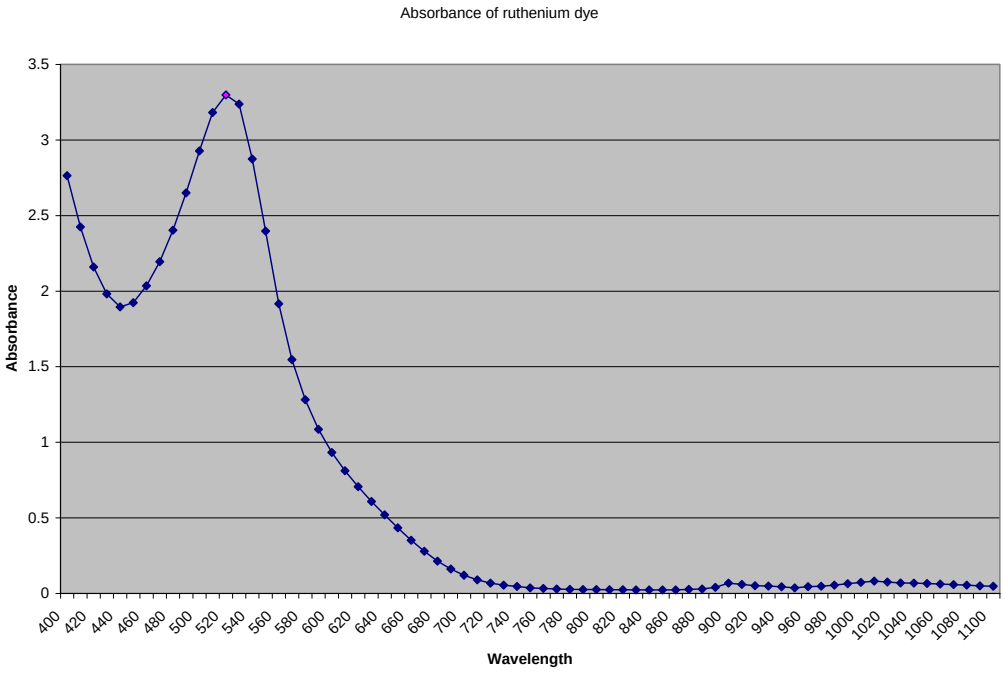

Figure 1.3: Spectral response of the N719 dye.

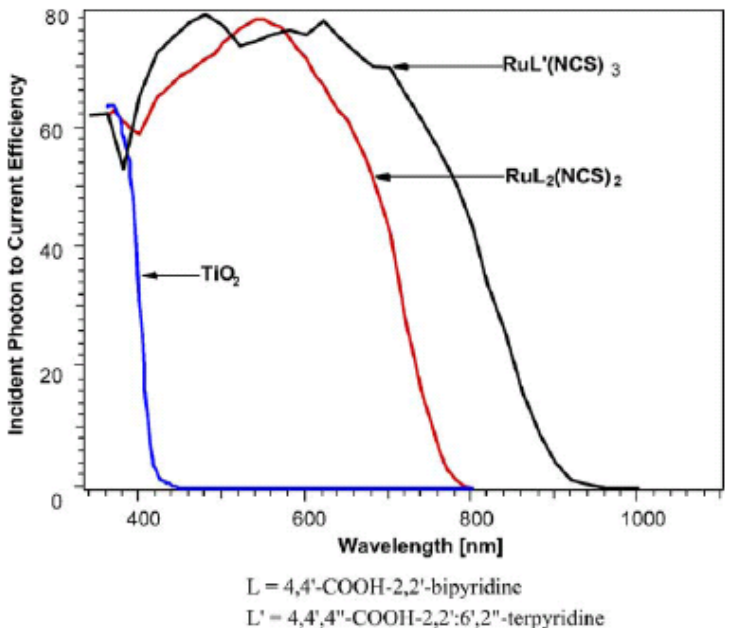

Figure 1.4: Photocurrent action spectra of the "N3 dye" (ligand L-indicated by red line) and the "black dye" (ligand L'-indicated by black line) [13].

Figure 1.4 compares the incident photon-to-current efficiency for two dyes, the N3 dye (*cis*-bis(isothiocyanato)bis(2,2'-bipyridyl-4,4'-dicarboxylato)-ruthenium(II)) and the "black dye" tri(cyanato)-2.2'2"-terpyridyl-4,4'4"-tricarboxylate)Ru(II).

The ruthenium based bipyridyl complexes such as the N719 have given the best efficiencies so far but other dyes based on Fe-bipyridyl complexes and organic dyes based on cyanine or merocyanine sensitizers have been investigated [14]. This remains a fertile area for research.

1.3.2. Charge transfer

The charge transfer processes in the N719 dye are shown in Figure 1.5. The COOH groups of the dye form a bond with the TiO_2 surface by donating a proton to the

TiO_2 lattice. The absorption of a photon by the dye molecule happens via an excitation between the electronic states of the molecule [9]. The excitation of the Ru complexes via photon absorption is a metal to ligand charge transfer (MLCT). This means that the highest occupied molecular orbital (HOMO) of the dye is localized near the metal atom, Ru in this case, whereas the lowest unoccupied molecular orbital (LUMO) is localized at the ligand species, in this case at the bipyridyl rings.

At the excitation, an electron is lifted from the HOMO level to the LUMO level. Furthermore, the LUMO level, extending even to the COOH anchoring groups, is spatially close to the TiO_2 surface, which means that there is significant overlap between the electron wave functions of the LUMO level of the dye and the conduction band of TiO_2. This directionality of the excitation is one of the reasons for the fast electron transfer process at the dye-TiO_2 interface [9].

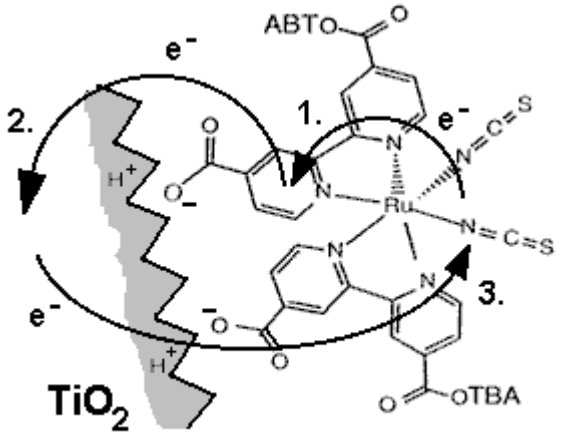

Figure 1.5: Charge transfer processes between dye and the TiO_2 lattice: 1. MLCT excitation, 2. Electron injection and 3. Charge recombination [9].

1.3.3. Charge Transport

In the DSSCs charge transport occurs by electron transport in the nanostructured TiO_2 electrode and hole transport in the electrolyte as I_3^-. Injected electrons in the conduction band of titania are transported by diffusion towards the back contact and reach the counter electrode through the external load. Although the electron transport process has been studied more extensively than the hole transport process because of several interesting fundamental questions, both charge transport mechanisms are equally important for the operation of the solar cell [9].

1.3.3.1 Electron transport in the titania layer

The mesoporous semiconductor nanoparticle layer has three main functions: it provides a high surface area for dye molecules, it accepts electrons from the dye and it conducts electrons to the TCO layer.

The mesoporosity of this layer is important for two reasons:

a. it provides a high surface area for dye adsorption which is important since electron injection into the semiconductor only happens when the dye molecules are bonded to the surface.

b. it provides a high surface area for the electrolyte ions. The electrolyte penetrates the porous film all the way to the back-contact making the semiconductor/electrolyte interface essentially three-dimensional [13].

The mesoporosity allows for effective screening by electrolyte ions of any charged species in the nanoparticles [15]. The electrolyte causes a screening effect

because of its overall negative charge so that even though it conducts holes away from the titania, it actually keeps the electrons from recombining with these holes as well.

Effect of Morphology and Crystal Structure of titania

A desirable morphology of the films would have the mesoporous channels or nanorods aligned in parallel to each other and vertically with respect to the TCO glass current collector. This would facilitate charge diffusion in the pores and the mesoporous film, give easier access to the film surface, avoid grain boundaries and allow the junction to be formed under better control [13]. A number of groups have worked on producing titania nanorods and nanotube arrays, a review on fabrication methods and applications of titania nanotube arrays can be found in this reference [16].

TiO_2 exists in three different crystalline polymorphs: rutile, anatase and brookite. For dye-sensitized solar cells (DSSC) the use of nanoporous anatase has been proven to be superior to rutile; this is believed to be related to the structure and chemical composition of the TiO_2 surface. The band-gap of rutile titania is 3.0 eV and that of anatase is 3.2 eV. Therefore, rutile has better visible light response and anatase has better photocatalytic activity [17]. The commonly used commercial titania nanopowder “P25” (Evonik Degussa) has a composition of ~70% anatase and ~30% rutile. The phase transition from anatase to rutile needs significant thermal activation and occurs between 700 - 1000 °C depending on the crystal size and the impurity content.

1.3.3.2 Ion transport in the electrolyte

The electrolyte in DSSCs is usually an organic solvent containing the redox pair I^-/I_3^-, which works as a hole-conducting medium. At the TiO_2 electrode the oxidized dye, left behind by the electron injected to the TiO_2, is regenerated by the electrolyte in the reaction:

$$2S^+ + 3I^- \rightarrow 2S + I_3^- \qquad \text{Dye Regeneration}$$

while at the counter-electrode I_3^- is reduced to I^- in the reaction

$$I_3^- + 2\ e^-(Pt) \rightarrow 3I^- \qquad \text{Electrolyte Regeneration}$$

The reduction reaction is catalyzed by a thin layer of platinum. The efficiency of a DSSC is based on different rate constants for iodine reduction at the front- and counter electrode. The iodine reduction at the counter electrode has to be orders of magnitude faster than the recombination at the TiO_2/electrolyte interface [8].

The viscosity of the solvent in the electrolyte should be preferably low in order to fill large modules by capillary forces. An electrolyte with lower viscosity helps to fill all of the pores and small crevices in the mesoporous electrode, allowing for rapid reduction of the dye in all places. Today, nitriles are commonly used as a solvent in DSSC modules: acetonitrile, propionitrile, 3-methoxypropiontrile. The disadvantage of using such a low viscosity solvent is that it often degrades in air and perfect sealing of the cell is critical. The liquid electrolytes are also very susceptible to degradation under thermal stresses. Upon exposure for prolonged periods to higher temperatures, i.e. 80–85°C, degradation of performance has frequently been observed [13]. Research has been carried out on electrolytes that contain ionic liquids, which exhibit a negligible vapor pressure and a high conductivity at room temperature. Combined with the low-flammability and a

wide electrochemical window, ionic liquids are promising candidates to replace the organic solvent. The use of ionic liquids such as derivatives of imidazolium salts has been widely studied in DSSCs [18-21].

Recombination:

The dye-sensitized solar cell is based on photoelectrochemical reactions at the semiconductor-electrolyte interface, and the operation of the cell is an outcome of competing opposite chemical reactions having differing rate constants.

The kinetic rates important for the DSSC are shown schematically in Figure 1.6 [22].

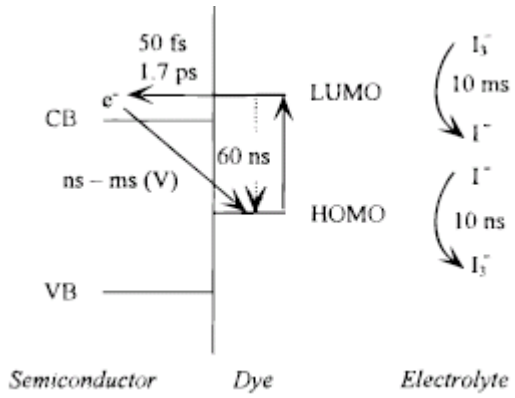

Figure 1.6: Schematic of the kinetics at the TiO_2/N3 dye/electrolyte interface [22]

As the figure illustrates, the rate of electron injection from the excited dye into the conduction band of the TiO_2 is one of the fastest chemical processes known occurring in the femtosecond time regime. The rate of back-electron-transfer from the conduction band to the oxidized sensitizer follows a multiexponential time law, occurring on a microsecond to millisecond time scale [22].

The electron-transfer rate from the I^- ion into cations of the N3 dye was estimated to be 100 nanoseconds [23]. This is important for obtaining a high cycle life for the dye, since lack of adequate conditions for the regeneration can lead to dye degradation. The electron conduction through the nanostructured TiO_2 has been estimated to occur in the millisecond time range.

1.4 Performance characteristics of a DSSC

1.4.1 I-V characteristics

A typical I-V curve for a Grätzel cell that used the "black" dye as a sensitizer is shown in figure 1.7 [22].

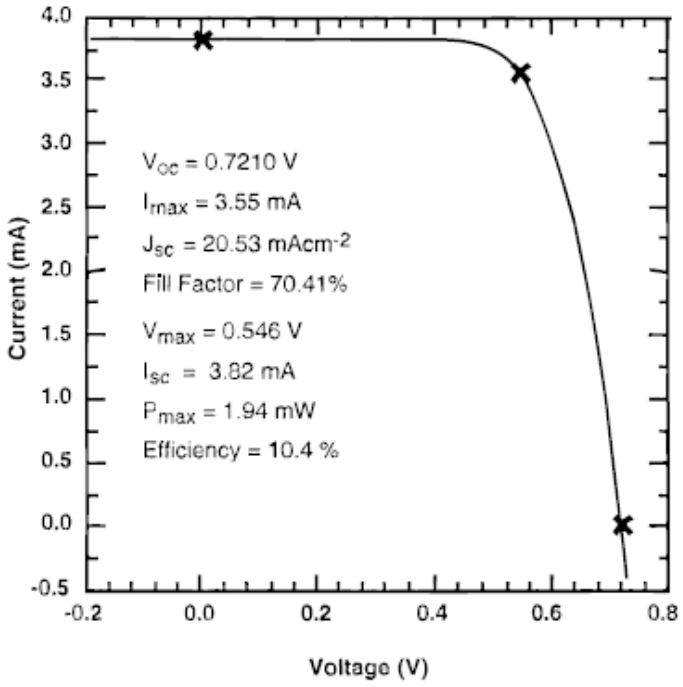

Figure 1.7: Photocurrent voltage characteristics of a DSSC sensitized with the "black" dye [22]

The overall conversion efficiency of the dye sensitized cell is determined by the photocurrent density measured at short circuit (I_{sc}), the open circuit photo-voltage (V_{oc}), the fill factor of the cell (FF) and the incident power P_{in}.

$$\eta = I_{sc} \times V_{oc} \times FF/P_{in}$$

The fill factor is a measure of the squareness of the I-V characteristic curve and is defined as:

$$FF = PP / (V_{oc} * I_{sc})$$

where PP is the peak power (the maximum power generated by the cell). FF is always less than 1.

The incident photon to current conversion efficiency is represented as a function of wavelength and is given by [23]:

$$IPCE[\%] = 100* \{1240[eV \cdot nm] \times J_{sc}[\mu A/cm^2] \} / \{\lambda[nm] \times \Phi[\mu W/cm^2] \}$$

where J_{sc} is the short-circuit photocurrent density for monochromatic irradiation, λ is the wavelength, and Φ is the monochromatic light intensity.

1.5 Motivation for this research work

Ultimately, the mass production of DSSCs will depend not only on the energy conversion efficiency of these devices, but also on how quickly this technology can be commercialized; and currently several companies are working in this direction. G24 Innovations Limited manufactures and designs solar modules using proprietary dye sensitized thin film technology. The company uses an automated "roll-to-roll" manufacturing process similar to inkjet printing to produce Dye Sensitized Thin Films [24]. Solaronix S.A. makes dye solar cell modules that use screen printing technique to

make titania electrodes. One of their prototype solar cell modules is shown in Figure 1.8 [25]. Dyesol Limited develops dye solar cell technology that can be directly incorporated into buildings by replacing conventional glass panels. Dyesol develops devices for the full range of PV applications using glass, metal, ceramic and plastic substrates. One of its interconnected solar cell module designs is shown in Figure 1.9 [26].

Large-scale commercialization of dye solar cell technology demands the use of conductive polymer substrates which allow roll-to-roll production to achieve high throughput. The use of polymer substrates also facilitates fabrication of flexible, light-weight and thin DSSCs. Currently, there is a tremendous focus on making such flexible solar cells using conductive polymer substrates; and low temperature processing methods need to be developed that are compatible with polymer materials.

This research work is focused on the development of low temperature processing methods for titania electrodes to improve the stability and efficiency of flexible DSSCs.

Figure 1.8: SERIO 3030W31 – Interconnected dye solar cell module (Solaronix SA) [25]

Figure 1.9: Dyesol Series Interconnect Glass Module [26]

1.5.1 Low temperature processing of titania electrode

For efficient electron transport throughout the TiO_2 nanoparticle network, and ultimately good power conversion efficiency, good electrical interconnection of the nanoparticles is a necessary prerequisite. In devices prepared on glass/FTO substrates, best performance is obtained by annealing the electrodes at 450°C which causes necking of the TiO_2 nanoparticles. This process cannot be used with low-cost flexible plastic substrates that cannot sustain temperatures higher than 150°C [27]. Therefore it is essential to develop low temperature sintering processes for preparation of the nanostructured titania films.

A variety of methods have been proposed for the low-temperature post-treatment of the nanostructured TiO_2 films, including room temperature compression techniques [28,29] microwave irradiation [30], UV irradiation [31,32] and hydrothermal crystallization [33,34].

This research is focused on chemical methods involving the reaction of a titanium alkoxide precursor to prepare nanostructured titania films with good particle-particle interconnections that are essential to achieve good power conversion.

An important goal of this research is to gain a fundamental understanding of the processes that lead to these particle interconnections (necking) and thereby illustrate the kinds of hydrothermal treatments that can ultimately be applied to flexible substrates used in DSSCs.

Chapter 2 of this thesis focuses on low temperature processing of titania photoanodes by combining commercial titania nanoparticles with a titanium alkoxide in a hydrothermal system. Chapter 3 is an overview of the concepts of reactive sintering as

applied to dye solar cell fabrication. Chapter 4 focuses on understanding the interparticle necking and pore structures created by the titania formation from the alkoxide at the macro-level; by substituting the commercial titania nanoparticles with monosized silica particles. The effect of silica morphology on the efficiency of silica-titania dye sensitized solar cells is discussed. Chapter 5 focuses on further investigations of the neck region created by the reactive sintering process; by preparing sub-monolayers of silica-titania using monosized 500nm silica particles. Scanning electron microscopy was used to look at the morphology of the sub-monolayers and atomic force microscopy was used to observe surface topography. Image analysis was done to study the effect of alkoxide concentration on the average neck width in 2-particle silica-titania chains. This work provides a greater insight into the formation of particle-particle interconnections with applications even beyond DSSCs. Concluding remarks are presented and future areas of work are outlined in Chapter 6.

Chapter 2. Low temperature hydrothermal processing of titania electrodes

2.1 Background

The conventional methods of preparing titania electrodes for dye sensitized solar cells involve coating a precursor, usually a colloidal suspension of titania nanoparticles onto glass substrates using coating techniques such as doctor-blading, dip-coating or screen printing. Organics are added to the TiO_2 precursor formulations to improve the quality of the film by breaking down agglomerates, to stabilize TiO_2 suspensions, and to increase the wetting capacity of the precursor mixture [35]. The titania film is then sintered at high temperatures of 400-500 °C in order to remove the organic additives from the precursor and improve interconnection of the particles.

Sintering enables the production of more uniform TiO_2 thick films without large pores or cracks. Sintering also improves the connection between the nanocrystallites that constitute the film (necking), and the adherence of the film to the transparent conducting oxide (TCO) coated substrate [35].

The disadvantage of a high temperature sintering process is that it cannot be applied to substrates such as plastic that are polymers which can be deformed/damaged at high temperatures. Polyethylene terephthalate (PET) is one of the plastic substrate materials that has been tested in DSSCs. The PET substrates are coated with a transparent conductive oxide such as indium tin oxide (ITO) to make them conductive.

Use of high temperature sintering is not viable in the case of PET substrates as they can damage the substrate and increase the resistivity of the ITO layer. It

is therefore necessary to develop low temperature sintering methods for flexible DSSCs; but significant challenges remain in improving the performance and stability of these cells as compared to DSSCs fabricated on rigid glass substrates.

Several research groups have studied the change in the efficiency of DSSCs with different sintering temperatures [36,37]. For example, Nakade et al [36] have studied the energy conversion efficiencies of solar cells sintered at 150 °C and 450 °C for three different TiO_2 synthesis methods (hydrolysis of aqueous $TiCl_4$ solution, hydrolysis of titanium tetraisopropoxide in nitric acid and use of commercial titania nanoparticle (P25)). In all three cases, the efficiency of films annealed at 150 °C is lower than those annealed at 450 °C. The lower efficiencies were attributed to lower short circuit current values. The diffusion lengths of the 150 °C annealed films were much lower than those of 450 °C annealed films. The longer diffusion lengths of high-temperature annealed films were attributed to the neck growth between particles and a decrease in charge trap density. Lowering the annealing temperature while improving the efficiency is one of the key challenges toward the commercialization of DSSCs.

2.2 Literature Review

A number of different low temperature annealing routes have been proposed. Mechanical compression of the TiO_2 films for short time intervals has been demonstrated on glass and plastic substrates; and efficiencies of 5.5% have been reported for titania pressed onto ITO-PET substrates [29].

UV irradiation followed by a low temperature annealing at 140 °C has been used to remove organic residues and improve the performance of the TiO_2 electrode used in

flexible DSSCs [31]. UV irradiation allowed degradation of surfactants used in the titania suspensions, but the efficiency of these cells was quite low (0.23%) compared to the electrodes prepared on glass substrates (0.45%).

UV irradiation has also been studied in experiments using a mixture of a commercial TiO_2 powder (Degussa P25) and a titania precursor (titanium(IV)*bis*(ammonium lactato)dihydroxide) by Gutiérrez-Tauste et al. [35]. UV treatment leads to decomposition of the titania precursor as a result of the photocatalytic activity of nanocrystalline TiO_2 present in the mixture, thus producing titania electrodes at low temperatures of 80 °C.

Miyasaka et. al. have reported the use of an aqueous colloidal sol of titanium oxide containing brookite-type nanocrystalline TiO_2, used as an interparticle connection agent [38]. Interparticle connection was assumed to proceed by dehydration of the hydrogen-bonded network of TiO_2 nanoparticles. DSSC efficiencies as high as 6.4% have been reported on ITO coated PEN (polyethylene naphthalate) plastic sheets prepared by this method.

While these studies all show promise, much improvement in efficiency with lower temperature processing is still necessary to reach a viable flexible DSSC cell.

2.2.1 Hydrothermal treatments using strong acid and/or strong base

There is a large literature base on the formation of high surface area titania using acid or base chemistries in which titania nanoparticles (such as P25) dissolve and reprecipitate and form nanofibers, nanorods or nanotubes at temperatures below 150 °C. Kasuga et al [39] reported that when anatase-phase or rutile-phase-containing TiO_2 was

treated with an aqueous solution of NaOH for 20 h at 110 °C and washed with HCl and distilled water, needle-shaped TiO_2 products were obtained. They report that the crystalline raw material is first converted to an amorphous product through alkali treatment, and subsequently, titania nanotubes are formed after treatment with distilled water and HCl aqueous solution.

Similarly Nian et al [40] have reported that the hydrothermal treatment of titanate nanotube suspensions under an acidic environment resulted in the formation of single-crystalline anatase nanorods. The nanotube suspensions were prepared by treatment of TiO_2 in NaOH, followed by mixing with HNO_3 to different pH values. These suspensions upon a hydrothermal treatment at 175 °C formed anatase titania nanorods.

2.2.2 Hydrothermal treatments at ~neutral pH

Although the acid-base chemistries give high aspect ratio nanostructures that improve performance in a DSSC (due to greater dye adsorption and faster electron conduction), the processes involved are mostly batch-type and cannot be used with substrates such as ITO coated PET which are affected by strong acid or strong base. Hence the need for processing methods that can be carried out at neutral pH, without acids or bases that can damage the polymer substrate.

A few studies have focused on the hydrothermal treatment of a titania precursor (under neutral pH) mixed with a commercial titania powder such as P25 (Degussa). The precursor is converted to titania through a sol-gel condensation process and the titania thus formed serves as interconnections between the P25 particles. In one approach,

titanium tetraisopropoxide[2] (TTIP) has been used as a cross-linking agent mixed with a slurry of Degussa P25 TiO_2 nanoparticles dispersed in methanol. When the coatings were exposed to moderate heat (50 °C) and moisture (20%RH), sol-gel condensation between the TiO_2 nanoparticles and the TTIP resulted in improved electrical interconnection of the particles. A large increase in short-circuit current and fill factor was observed in DSSCs using FTO coated glass substrates when 25wt% of titanium tetraisopropoxide was added to P25 particles and the efficiencies increased from 1.01% for cells with no TTIP added to 2.43% for cells with 25wt% TTIP added [27].

Zhang et al. have used an aqueous or ethanolic paste of nanocrystalline titania P25 and titanium salts such as $TiCl_4$, $TiOSO_4$ and alkoxides of titanium in a steam treatment process at 100 °C [41]. They claim that under hydrothermal treatment at 100 °C in the solid-gas (film-water vapor) interphase, the added titanium salts hydrolyzed or crystallized into either anatase or rutile TiO_2 acting as "glue" to chemically connect the titania particles to form mechanically stable porous films. DSSCs employing these porous electrodes achieved efficiencies of up to 4.2%. A schematic of the process is shown in figure 2.1.

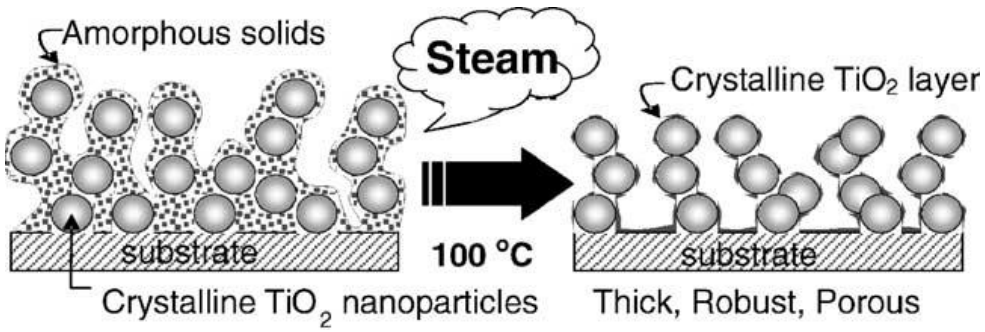

Figure 2.1: Schematic of the film formation during hydrothermal crystallization at the gas/solid interface [41]

[2]TTIP: Titanium tetraisopropoxide; chemical formula: $Ti\{OCH(CH_3)_2\}_4$

2.2.3 Chemistry and Mechanism

The mechanism proposed for the hydrothermal process using a titanium alkoxide precursor is a sol-gel condensation between the TiO_2 nanoparticles and the alkoxide in the presence of water [27].

$4TiO_2 + Ti(OR)_4 + 4H_2O \rightarrow Ti(OTi)_4 + 4ROH$ (where R = C3H7) [27]

which can be written in two separate steps as follows:

Hydrolysis Reaction: Ti-OR +H_2O → Ti-OH +ROH

Condensation: Ti-OH + Ti-OR → Ti-O-Ti + ROH

Miyasaka et al [38] have proposed an alternate mechanism for interparticle connection based on a hydrogen-bonded network of particles with surfaces covered with hydroxyl groups. Instead of a molecular titania precursor, a colloidal sol of brookite-type nanocrystalline TiO_2 is used as the interparticle connection agent. Figure 2.2 illustrates this mechanism.

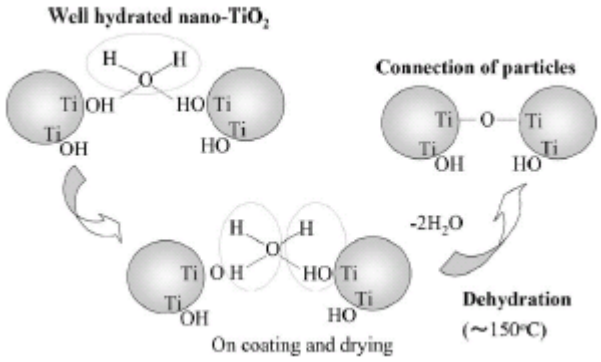

Figure 2.2: A mechanism for interparticle connection of nanocrystalline TiO_2 particles dispersed in an aqueous medium via formation of a hydrogen-bonded network [38].

2.3 System of approach

The low temperature method followed in our experiments involves the hydrothermal treatment of a titania precursor (under neutral pH) mixed with a commercial titania powder such as P25 (Degussa). The precursor is converted to titania through a sol-gel condensation process and the titania thus formed serves as interconnections between the P25 particles.

2.3.1. Materials and Methods

Commercial titania P25[3] nanopowder (Aeroxide P25) was purchased from Evonik Degussa. TTIP and ethanol (99.5% pure) were purchased from Sigma-Aldrich. The substrates used for the experiments were FTO coated glass ($10<R<20\Omega$/sq) obtained from Flexitec Eletrônica Orgânica Ltda.

The steam treatment was performed by preparing a 1M (molar) solution of TTIP in ethanol and adding the required amount of P25 powder. To 3.6g of the TTIP solution, 0.1g of P25 is added. This gives a weight ratio of 0.95:0.1 for TTIP:P25 in the dispersion. There should be minimal amount of TTIP exposure to the atmosphere during the preparation of this dispersion to prevent hydrolysis of TTIP. The mixture of TTIP solution and P25 is then blade coated onto the FTO glass substrates. Blade coating is performed by placing a few drops of the dispersion on the FTO glass slide and using a sharp blade to spread the dispersion onto the glass slide. This process can be repeated depending on the desired thickness of the films. The blade coated samples are placed on a Petri dish and steam treated at the desired temperature (110-130 °C) by placing the Petri dish in a beaker containing DI water. The procedure is shown schematically in Figure 2.3. After steam treatment, the samples are dried at room temperature. The dried samples

[3] P25 is a highly dispersed titanium dioxide available from Evonik Degussa

are then used for different characterization studies. To obtain powder samples for XRD characterization, the same procedure was used but instead of blade coating the dispersion onto FTO coated glass slides; the dispersion was directly treated under steam while being constantly stirred at a speed of 200rpm.

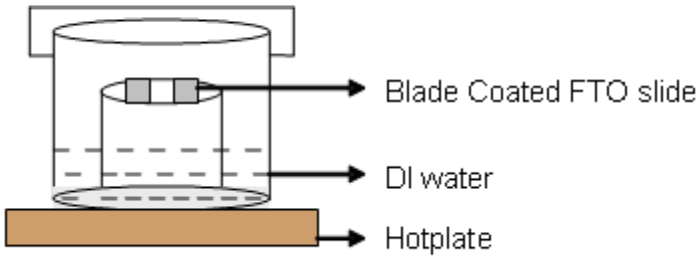

Figure 2.3: Schematic of experimental setup for steam treatment method

2.3.2 Physical characterization (Morphology and Phase)

The thickness of the films was determined using a Tencor alpha-step200 profilometer. Scanning electron microscope (GEMINI ZEISS FESEM) with an Everhart-Thornley (E-T) detector was used to study morphology of nanoparticle structures and interconnections. Carbon tape was used to stick the samples onto the aluminum SEM studs. Gold coating using a sputter deposition system was done on the samples to make them conductive. XRD (Siemens Kristalloflex diffractometer : Cu Kα source at 40kV and 30mA) was used to study crystallinity and phase of titania.

The SEM images of the reactant mixture before steam treatment and product obtained after steam treatment for two magnification settings (10000 and 30000) are shown in Figure 2.4. In the SEM image on the left, it appears that the unreacted titania precursor is covering all the P25 particles, and the image on the right shows the

transformation of this precursor after steam treatment. A number of larger aggregates in various sizes and smaller particles are also seen. The image at 30KX magnification reveals in greater detail the rough surface of the titania obtained after steam treatment. It can be noted from the image on the right in Figure 2.3 that the P25 aggregates are not easily distinguishable from any titania that is formed by hydrothermal treatment of the titania precursor.

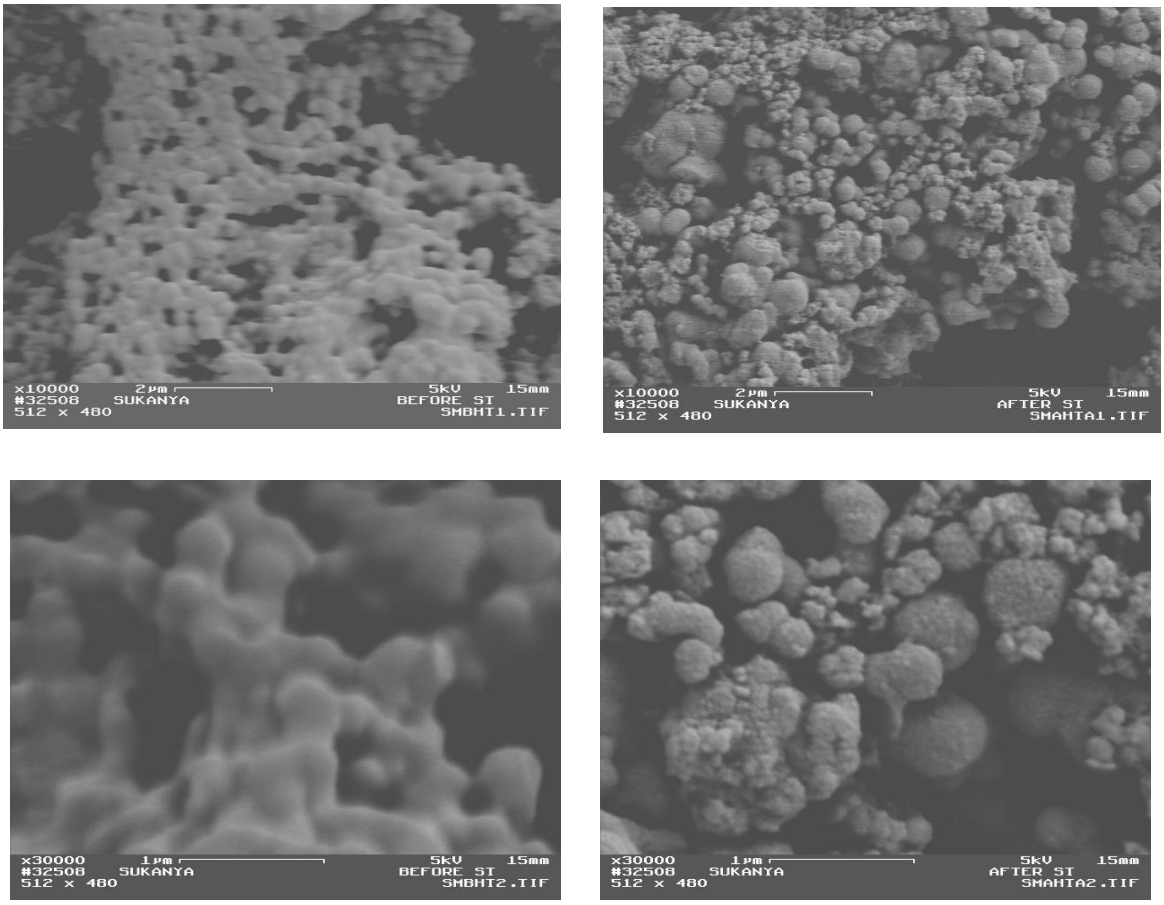

Figure 2.4: SEM image of titania precursor + P25 mixture before (left) and after (right) steam treatment.

To determine the phase of the reactant mixture before steam treatment and product obtained after steam treatment, an XRD of the material was performed before and after steam treatment and the result is presented in Figure 2.5. The XRD pattern shows anatase and rutile TiO_2 peaks as well as several smaller peaks. From the XRD pattern of the powder obtained after steam treatment, the distinction between the TiO_2 peaks from the P25 powder and any possible TiO_2 peaks from the titania precursor is not clear. The appearance of several smaller peaks also points to the presence of organics/impurities that have not been completely removed from the powder. It is worth noting that the commercial Degussa P25 TiO_2 consists of ~70%anatase and ~30% rutile phases.

.

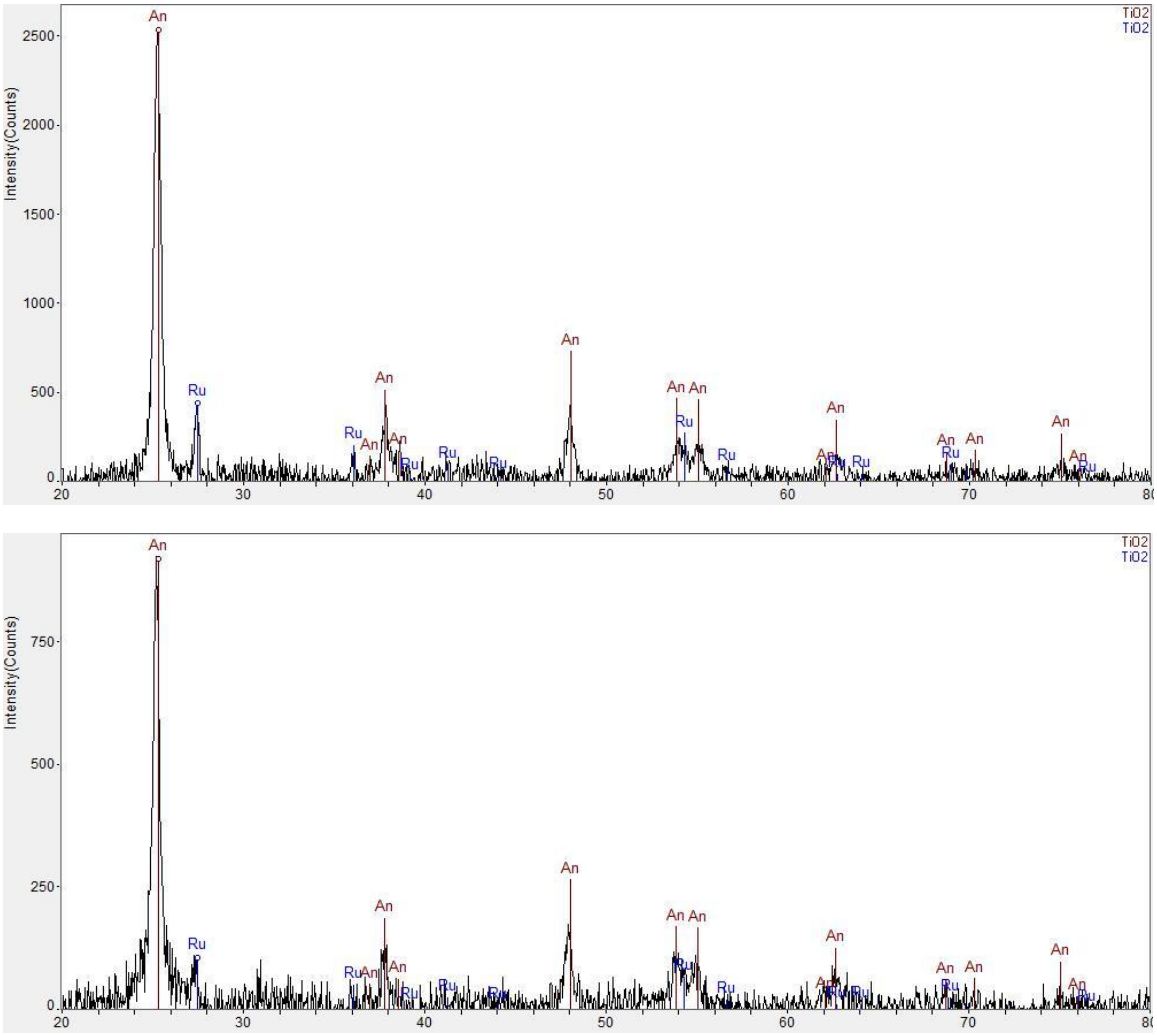

Figure 2.5: XRD before (top) and after (bottom) steam treatment.

2.3.3 Electrical characterization (I-V characteristics and electrochemical impedance spectroscopy)

To determine the effect of the steam treatment on the efficiency of dye sensitized solar cells; a number of samples were blade coated, steam treated, dyed and tested. For these experiments, a mixture of P25 and titanium tetra isopropoxide (TTIP) was prepared in 5 ml methanol (99.8% pure) for five different weight ratios of P25:TTIP; namely 1:0, 1:0.25, 1:0.5, 1:0.75 and 1.0:1.0g. This dispersion is blade coated onto clean FTO

(fluorine doped tin oxide) glass slides; the number of coatings determines film thickness. A drop of TritonX-100 surfactant is added to the dispersion to improve adhesion of the films to the substrate.

The thickness of all the coatings are maintained in the range of 14-17 μm by varying the number of times the sample is blade coated. The films are treated in air for 30 minutes and dried at 150 °C for 30 minutes. The dried coatings are placed in a solution of 0.28mM ruthenium dye in ethanol overnight. The ruthenium dye used is Ruthenizer 535 bis-TBA (N719); a commercial dye available from Solaronix. The dyed samples are rinsed with ethanol, dried at room temperature and used as the anode. Platinum sputtered on FTO coated glass is used as the cathode.

Dye sensitized solar cell assembly

The dye sensitized solar cells were assembled by sandwiching the electrolyte between the photocathode and photoanode. A 25μm thick polyolefin separator membrane approximately 1 square inch in area is dipped into the electrolyte solution and placed on the photoanode. The electrolyte used for the I-V characterization has the following composition: LiI (0.5M), I_2 (0.05M), 4-tert-butyl-pyridine (0.5M) in 5mL of methoxypropionitrile solvent. On the top of this assembly the platinum coated FTO glass slide (photocathode) was placed in such a way that some bare FTO substrate was exposed for making external electrical connections. In the end, a mask with 0.25 cm^2 area hole was placed on the back side of the photoanode and the whole assembly was held together using two binder clips. The process of assembling the solar cell is shown stepwise in Figure 2.6.

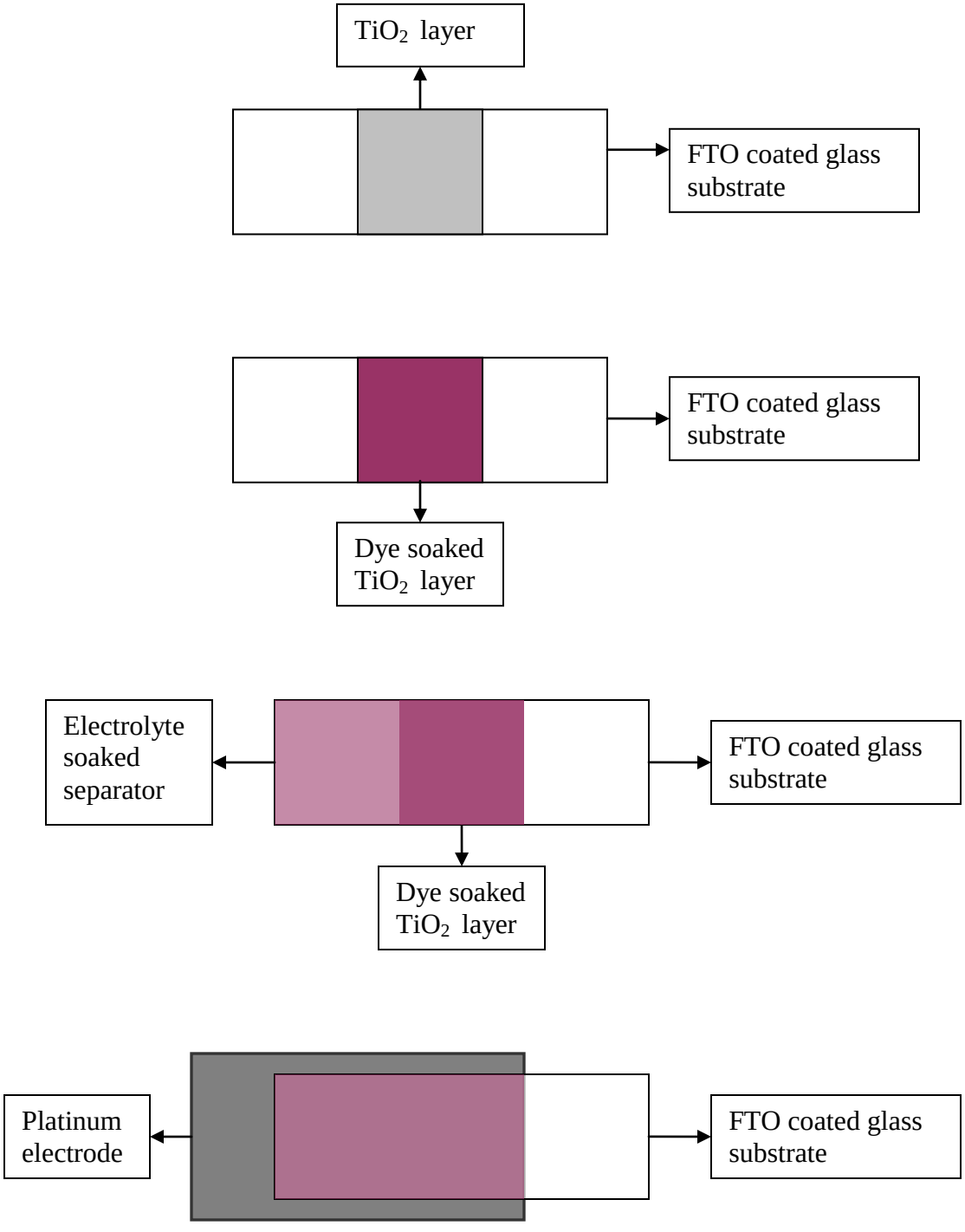
TiO_2 layer
FTO coated glass substrate
FTO coated glass substrate
Dye soaked TiO_2 layer
Electrolyte soaked separator
FTO coated glass substrate
Dye soaked TiO_2 layer
Platinum electrode
FTO coated glass substrate

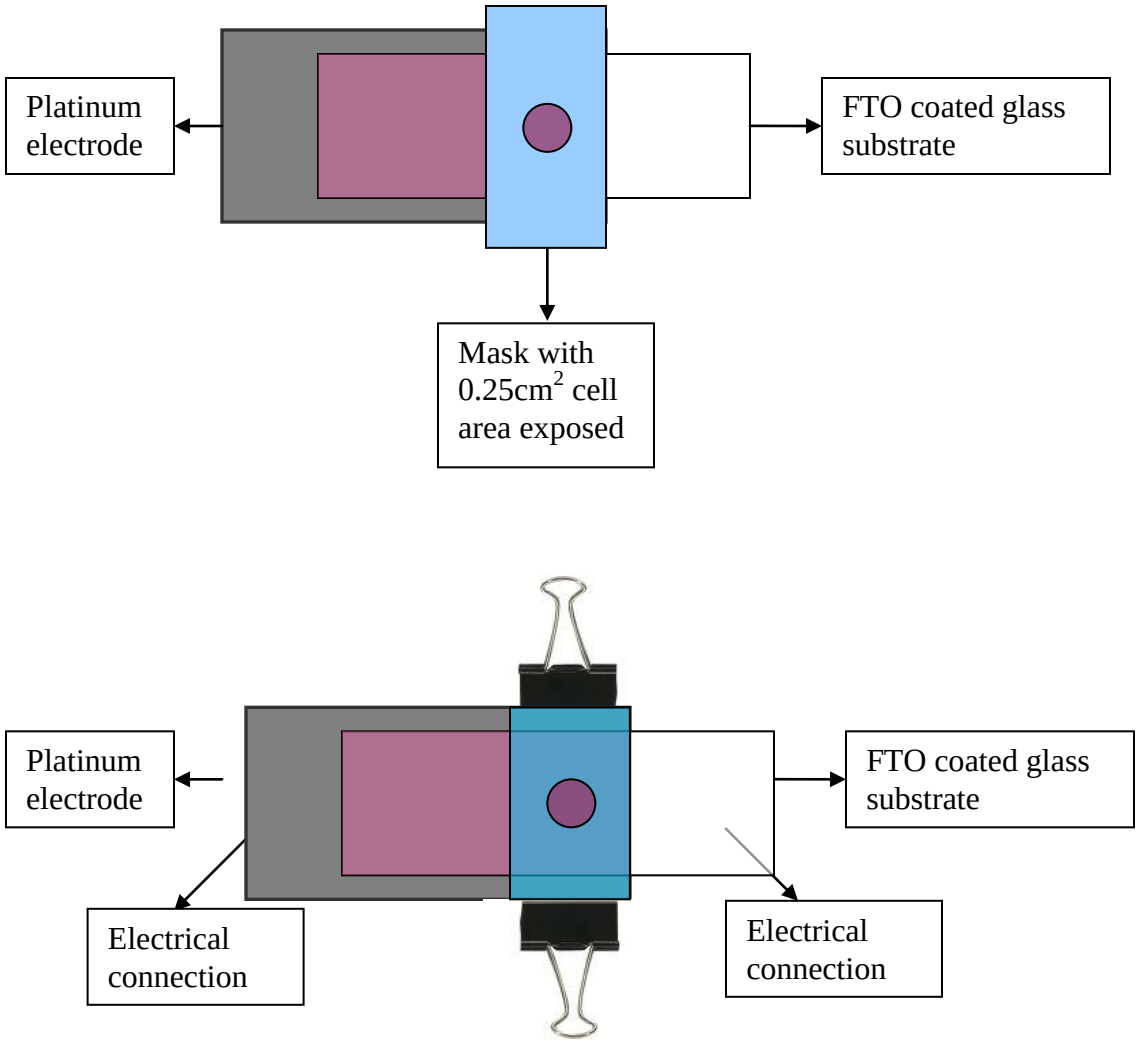

Figure 2.6: Schematic of a step-by-step assembly of a DSSC

2.3.3.1 I-V characteristics

A solar simulator is used to obtain I-V characteristics of the DSSC. Since the cells were not completely sealed, but just held together using the binder clips, they were assembled in the solar simulator lab just before measuring the current-voltage characteristics. This was done to reduce the effect of electrolyte evaporation on solar cell performance. The assembled solar cells were placed on a table at a fixed height in such a way that the light output from the 300 W Xenon solar simulator (Newport, Oriel 91160A) [42] on the cell was 90 W/m^2 measured by an irradiance meter (Daystar, Solaqua). The entire simulator setup is shown in Figure 2.7. The light was passed through the 0.25 cm^2 mask on the photoanode. Alligator clips were used to make the electrical connections. They were connected on the other side to a voltage source (HP 4140B pA meter/voltage source). A Labview program was used on the solar simulator as well as on the electrical characterization equipment through which -0.3 to 1.0 volts were fed to the solar cell with a step size of 10 mV. The photo current was collected in the dark and under 90 W/m^2 illumination. The output was represented in two formats: current vs. voltage data points and calculated solar cell characteristics such as efficiency, fill factor, short circuit current, and open circuit voltage.

Figure 2.7: a. Newport solar simulator and computer and b. the voltage supply.

The I-V characteristics obtained for 5 different TTIP:P25 weight ratios are shown in figure 2.8 and table 2.1. Generally speaking, the addition of the TTIP has increased the performance, at least up to a point where the addition is pushing the P25 particles apart from each other and lowering the current output.

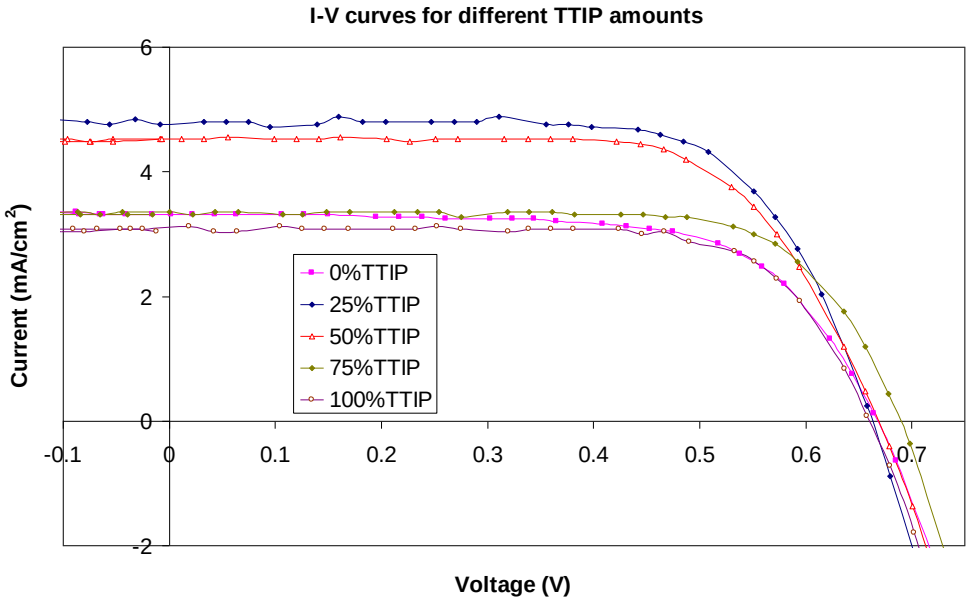

Figure 2.8: I-V characteristics of DSSCs for 5 different TTIP:P25 weight ratios.

Table 2.1: I-V characteristics of DSSCs for 5 different TTIP:P25 weight ratios.

TTIP:P25 (wt%)	**Isc (mA/sq.cm)**	**Voc (V)**	**FF**	**Efficiency=η (%)**
0%	3.28	0.67	0.68	1.48
25%	4.76	0.67	0.69	2.09
50%	4.64	0.67	0.63	1.85
75%	3.28	0.68	0.75	1.69
100%	3.08	0.65	0.74	1.46

From the I-V characteristics of the DSSCs it can be seen that the addition of TTIP (25 wt%) improves the efficiency of DSSCs. We infer that this is due to the improvement in the P25 particle interconnections. The increase in efficiency on addition of TTIP is mainly due to the increase in short circuit current in the cell. However, there is an optimum TTIP amount beyond which efficiency decreases probably due to more amorphous titania covering the P25 particles. The addition of more TTIP could also lead to lower porosity which can then cause lower dye adsorption and, thus, lower short circuit current.

2.3.3.2 Electrochemical impedance spectroscopy (EIS)

EIS is a steady state method used to obtain the electrical response of an electrochemical cell to an applied AC potential over a range of frequencies [43]. Electrochemical impedance is usually measured with a very small input signal, which does not perturb the system much. The data is represented as the Nyquist plot or Bode plot and analyzed by fitting to an equivalent electrical circuit model, based on the physical electrochemistry of the system.

EIS was used to study charge transport processes in a DSSC as the weight ratio of TTIP to P25 is varied. The electrochemical impedance spectroscopy was performed using an impedance analyzer (Solartron analytical, 1255B) connected to a potentiostat (Solartron Analytical, 1287). The EIS spectra were measured over a frequency range of 10^{-1} to 10^{6} Hz at 298 K under open circuit condition with 10 mV amplitude. The electrical impedance spectra were characterized using the *Z*-View software (ZView Version 3.1 Scribner Associates Inc.)

EIS data are usually represented in the form of either a Nyquist plot or a Bode plot. Nyquist Plots are a way of showing frequency responses of linear systems. Nyquist plots display both amplitude and phase angle on a single plot, using frequency as a parameter in the plot. Bode plots use frequency as the horizontal axis and use two separate plots to display amplitude and phase of the frequency response. Bode plots are really log-log plots, so they collapse a wide range of frequencies (on the horizontal axis) and a wide range of gains (on the vertical axis) into a viewable whole [44].

Figures 2.9 and 2.10 show the Nyquist and Bode plots for DSSCs prepared for five different TTIP:P25 weight ratios.

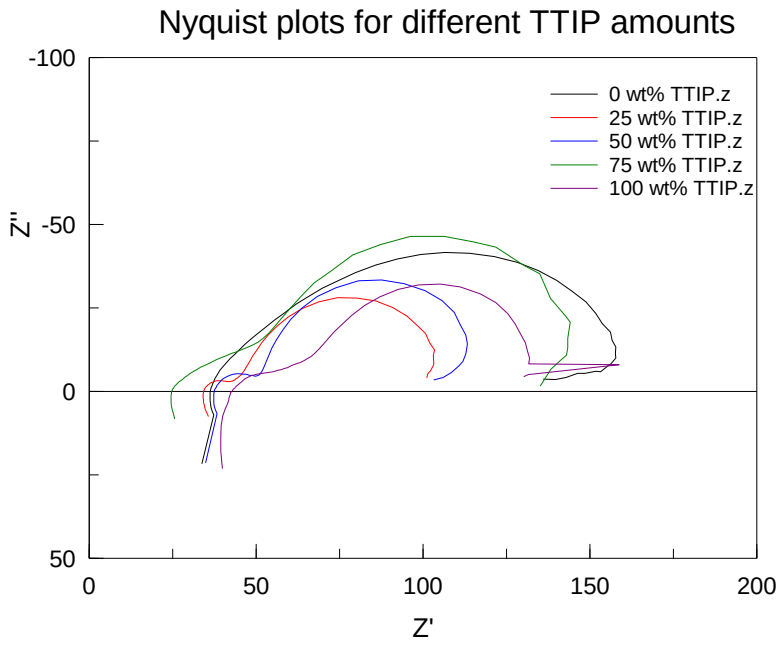

Figure 2.9: Nyquist plot of impedance spectra for DSSCs prepared for 5 different TTIP:P25 ratios

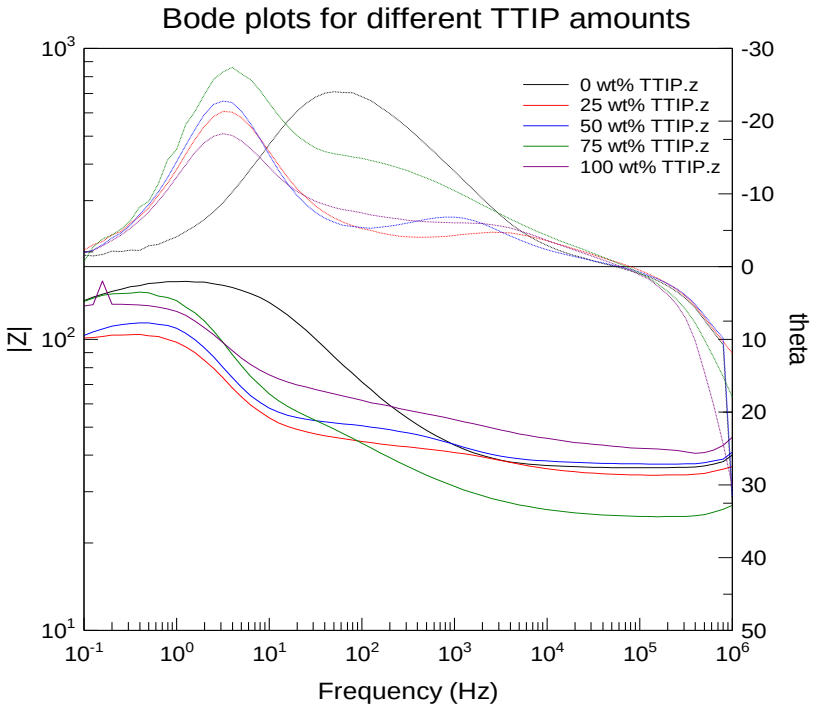

Figure 2.10: Bode plots of impedance spectra for DSSCs prepared for 5 different TTIP:P25 ratios

Under ideal conditions, the Nyquist plot of a typical dye sensitized solar cell shows three semicircles, corresponding to the three main photoelectrochemical processes occurring during the cell operation: Nernst diffusion of iodine/iodide species through the electrolyte and titania coating, electron transfer at the titania/dye/electrolyte interface and electron transfer at the counter electrode [45-47]. The semicircle associated with the Nernst diffusion process is usually seen at frequencies between 0.01 to 0.1 Hz and therefore requires a long recording time. The cells tested in the present research were not completely sealed; therefore the EIS data acquisition time was limited to a couple of minutes per cell. Therefore the frequency range selected for the EIS data acquisition was from 0.1 Hz to 10^6 Hz, which means, only two semicircles associated with the Pt electrode interface and the TiO_2/dye/electrolyte interface were usually observed.

- The semicircle in the low frequency region (larger semicircle) is attributed to the charge transfer in the TiO_2/dye/electrolyte layer
- The semicircle in the high frequency region (smaller semicircle) is attributed to the electrochemical reaction at the Pt counter electrode

In the Nyquist plot of figure 2.9, the 25wt% TTIP cell showed the least impedance as seen from the diameter of the low frequency semicircle which suggests that the addition of 25 wt% TTIP has improved the particle interconnections in the titania electrode.

In the Bode plot of figure 2.10, it can be seen that the characteristic frequency is higher for the 0%TTIP sample showing that the electron lifetime in the TiO_2 layer is lowest when no TTIP is added. This helps explain how the addition of TTIP helps increase short circuit current.

The impedance plots are fitted to an equivalent circuit model (Figure 2.11) using the Zview software (Scribner Associates Inc.) and the model parameters are shown in Table 2.2.

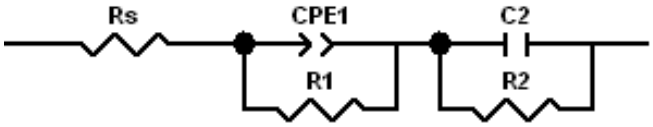

Figure 2.11: Equivalent circuit model used to represent interfaces in DSSCs

Table 2.2: R and C parameters obtained from fitting the data to the equivalent circuit model

%TTIP	Rs(Ω)	R1(Ω)	R2(Ω)	C2(F)	t=R2*C2(s)
0%	34.67	106.9	27.7	0.0004	0.011
25%	31.89	21.38	54	0.0013	0.070
50%	37.03	16.04	65.5	0.0011	0.073
75%	24.01	43.72	83.9	0.0009	0.077
100%	40.27	43.15	55.2	0.0013	0.074

In Table 2.2 Rs represents impedance of FTO layer and FTO/TiO_2 interface, R1 and CPE1 (constant phase element) together represent the electrochemical reaction at the Pt counter electrode, and R2 and C2 represent the transfer in the TiO_2/dye/electrolyte layer. Variation in Rs (25-40Ω) is partly attributed to variation in the resistivity of the FTO glass substrates; variation in R1 is attributed to the separator area between the titania layer and the Pt electrode. The gradual increase in the R2 value as %TTIP goes from 0% to 75% may be associated with a lower level of crystal perfection of the crystallized

titania that is formed and possibly lower conduction rate between the P25 particles in the coating.

2.3.4 Effect of cell illumination on DSSC performance

In section 2.3.3, we discussed the performance of dye sensitized solar cells for an illumination intensity of 90 mW/cm^2. In this section we will discuss the performance of dye sensitized solar cells with varying illumination intensities. For this study, solar cells were prepared and assembled as discussed in section 2.3.3. The illumination was adjusted on the simulator and the following intensities were used: 60,100,150 and 200 mW/cm^2. The results of I-V characterization for these 4 intensities are shown in Table 2.3 for 5 weight ratios of TTIP:P25.

From the table it can be noted that an increase in illumination causes an increase in short circuit current for all ratios of TTIP:P25 tested. This is probably due to the proportionately larger number of electrons being injected into the TiO_2 particles at higher illumination intensities. The highest short circuit current density of 8.24 mA/cm^2 was obtained for the cell prepared with 25wt% TTIP. This increase in short circuit current density is mainly responsible for the increasing efficiency of the cell when the illumination is higher. A slight increase in V_{oc} was also observed with increasing illumination intensity. No particular trend was observed with respect to the fill factor. The maximum DSSC efficiency of 1.92% was obtained for the 25 wt% TTIP cell under an illumination of 100 mW/cm^2.

Table 2.3: Solar cell efficiencies at different illumination intensities

	P_{in}(mW/cm^2)	V_{oc}(V)	I_{sc}(mA/cm^2)	FF	Eff (%)
0%TTIP					
	60	0.59	1.03	0.52	0.53
	100	0.61	1.70	0.56	0.59
	150	0.63	2.48	0.61	0.63
	200	0.64	3.16	0.61	0.62
25%TTIP	60	0.66	2.26	0.72	1.80
	100	0.68	3.98	0.71	**1.92**
	150	0.69	6.09	0.69	1.92
	200	0.7	**8.24**	0.65	1.87
50%TTIP	60	0.6	1.72	0.54	0.92
	100	0.63	3.01	0.63	1.20
	150	0.65	4.58	0.66	1.30
	200	0.66	6.02	0.67	1.33
75%TTIP	60	0.62	1.82	0.73	1.37
	100	0.66	3.19	0.70	1.47
	150	0.68	4.75	0.68	1.47
	200	0.69	6.53	0.65	1.46
100%TTIP	60	0.6	1.65	0.72	1.19
	100	0.67	2.50	0.71	1.19
	150	0.7	3.74	0.72	1.26
	200	0.71	5.07	0.70	1.25

2.3.5 Effect of type of alkoxide on DSSC performance

Dye sensitized solar cells were prepared and assembled as described in section 2.3.3 with a different titanium dioxide precursor (titanium butoxide[4] instead of titanium isopropoxide). As with the TTIP, five weight ratios of titanium butoxide (TB):P25 were tested. The thickness of the coatings as measured in the profilometer was in the range of 40-45μm. The thickness of the layers prepared with titanium butoxide were thicker than those prepared with TTIP. The solar cell test data for five ratios of TB:P25 at an illumination of 90 mW/cm^2 is shown in Table 2.4.

Table 2.4: I-V characteristics of DSSCs for 5 different TB:P25 weight ratios

TB:P25 (wt%)	**I_{sc} (mA/sq.cm)**	**V_{oc} (V)**	**FF**	**Efficiency=η (%)**
0%	0.90	0.65	0.79	0.51
25%	3.30	0.66	0.72	**1.75**
50%	3.42	0.61	0.66	1.54
75%	2.38	0.60	0.74	1.18
100%	1.96	0.60	0.70	0.91

From the table, we can see that the efficiency is highest for a 25wt% addition of titanium butoxide and the trend is similar to that observed with TTIP (Table 2.1). However, the overall efficiencies are lower than 2%. One reason for this could be the higher thickness of these films. Optimum thickness is very important as a thinner coating does not absorb the incident light completely. Thicker coatings capture the light completely, but add too much conduction distance through the sintered titania matrix. Generally it has been observed that a 10 to 15 μm thick film is optimum [6].

[4] Titanium (IV) butoxide (TB): chemical formula: $Ti(OCH_2CH_2CH_2CH_3)_4$

2.4 Summary

From the I-V and EIS characterization it is clear that although the addition of TTIP or TB enhances the short circuit current of the DSSC (up to a certain weight ratio); the overall efficiencies of the best performing cells were still only around 2%. To be competitive with other solar cell technologies, we believe that the efficiencies of these low temperature sintered cells should be at least 7-10%. It would be interesting to see if this could be achieved by tailoring the microstructure of the titania electrode so that the low temperature sintering process creates better particle interconnections which can then lead to higher short circuit currents.

It is therefore useful to look into the role of the reactive titania precursor in greater detail; particularly relating to the formation of the interconnections between the host particles (such as P25). In chapter 3 we have developed a theoretical framework to understand the formation of such interconnections. In chapters 5 and 6 we have aimed our experiments to understand how the reacted material collects at the interparticle necks. This was studied by using an oxide material (silica) in place of the P25 to be able to clearly pinpoint the titania signal from the TTIP without any interference due to the titania signal from the P25 nanopowder.

Chapter 3. Chemical Sintering Applied to Dye Solar Cell Fabrication

In Chapter 2, the low temperature processing of titania electrodes using a reactive titanium alkoxide precursor was discussed. The focus of chapter 2 was on improving the efficiency of the dye sensitized solar cell by the addition of varying amounts of a titanium alkoxide precursor. While it is very important that the addition of the reacted titania improve the efficiency of the dye sensitized solar cells, several other characteristics of the titania electrode also need to be considered. These include: surface area, porosity, and interconnectivity in the microstructure (particle necking). A high surface area and porosity can allow a large quantity of dye to be adsorbed, which means a large quantity of photons are available for dye excitation. Good interconnections between TiO_2 particles are essential to ensure rapid electron transport in the TiO_2 film.

3.1 Surface Area

The electron-collecting layer in a DSSC is typically a 10 μm thick nanoparticulate film, with a three-dimensional network of interconnected 15–20nm sized nanoparticles [48]. The surface area of widely used Degussa P25 titania nanoparticles is in the range of 50-60 m^2/g [49,50]. Higher surface area of titania nanoparticles would allow more dye adsorption and light harvesting. Because of the importance of microstructure in influencing the performance of DSSCs, a variety of approaches have been used to try and reach improved cells. Two of the distinctly novel ways will be reviewed here, followed by a detailed discussion of how nominally spherical particles “fit” together in more conventional microstructures. The two novel approaches are:

1. Ordered titania nanotube or nanorod arrays
2. Core-shell particles with a mesoporous titania shell layer

3.1.1 Nanotubes/Nanorods

Nanotubes and nanorods of titania have been widely studied in DSSCs due to their high surface-to-volume ratios and size dependant properties. The arrangement of highly ordered titania nanotube arrays perpendicular to the surface of the substrate permits facile charge transfer along the length of the nanotubes from the solution to the conductive substrate, thereby reducing the losses incurred by charge-hopping across the nanoparticle grain boundaries. Easier access to the nanotube array surface, as well as better control of the interface makes this morphology desirable for DSSCs. The enhancement in the electronic transport also allows for improved light harvesting as thicker films can be used to increase the optical density, thus improving the absorption of low-energy photons in the red and infrared without losing the additionally harvested charge carriers to recombination [16]. Figure 3.1 shows a schematic of a nanotube array based DSSC.

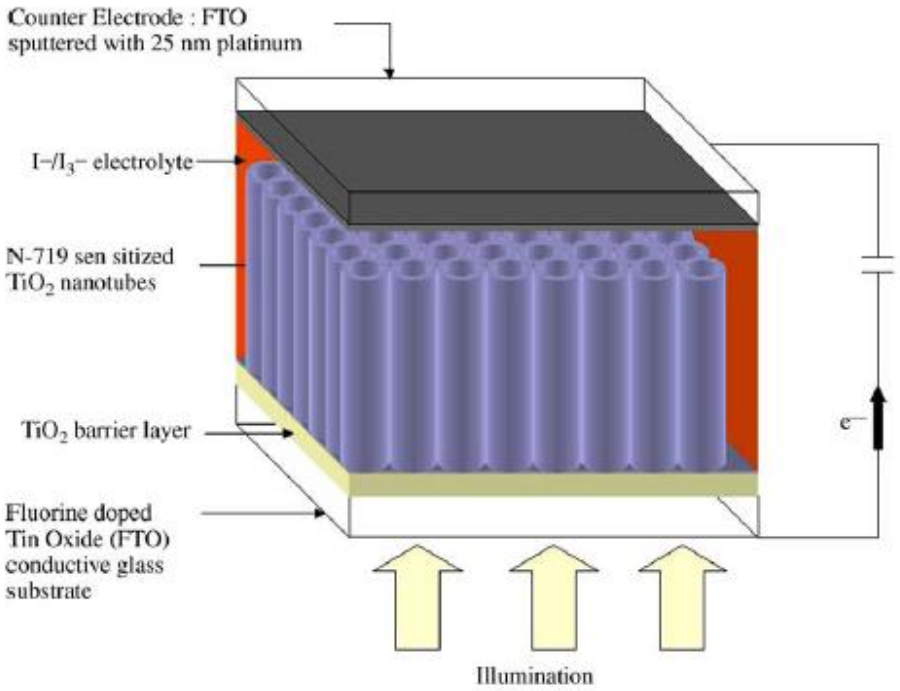

Figure 3.1: Illustration of a DSSC based on a titania nanotube array architecture [16].

Titania nanotubes and nanoarrays can be produced by a variety of methods such as sol-gel, seeded growth, hydrothermal processes and anodization in fluoride baths. Although efficiencies of around 7% have been demonstrated [51,52] the processing methods generally involve harsh chemicals and moderate to high temperatures and are thus not suitable for polymer substrates.

3.1.2 Core-shell structures

Several core-shell structures based on an oxide core and oxide shell have been used in dye sensitized solar cells [53,54]. Silica has also been used as an oxide core due to its inertness and ease of availability. Silica-titania core-shell materials have been shown to have high photocatalytic activity [55]. Lim et al. [56] obtained homogeneous and highly dispersed titania shells on silica spheres by a sol-gel method. The surface areas of titania-coated spheres (ST-4x) calcined at 400-600 °C ranged from 107.5 to 44.3 m^2/g. In addition, the surface area of the titania shell (44.3 m^2/g) calcined at 600 °C was substantially more than for the free powder (3.8 m^2/g). Due to the ease of manufacture and control over shell thickness that can be achieved by sol-gel synthesis, core-shell powders of increased surface area have found a lot of applications. With a suitable titania precursor, core-shell powders can be prepared by a chemical sintering method involving an inert core such as silica. We have used this approach, as reported in detail in Chapter 4 and Chapter 5.

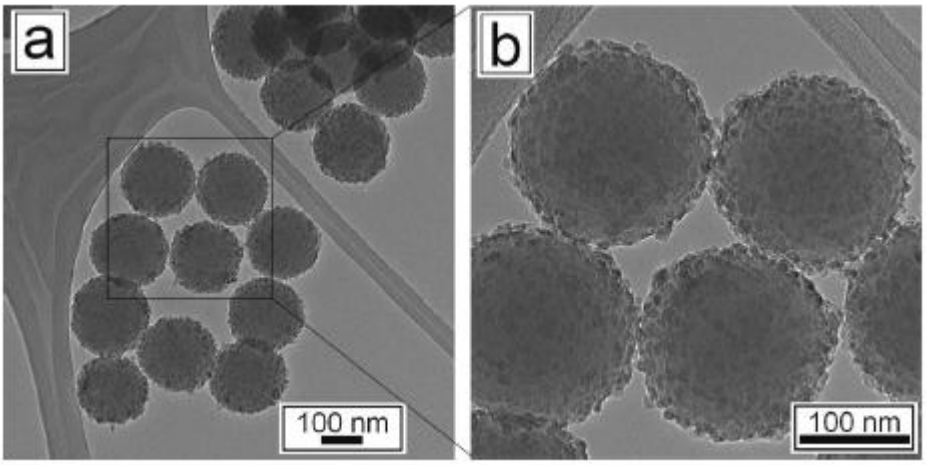

Figure 3.2: TEM images of ST-4x catalyst after calcination at 600°C [56].

3.2 Porosity and pore size distribution

The typical nanostructured titania film in a dye sensitized solar cell consists of a large network of interconnected particles about 20 nm in diameter. The film porosity is typically in the range of 50-65%, showing that pores can constitute more than half of the volume of the film – though having the porosity is critically important for placement of the dye and for interconnecting the system with the iodide electrolyte.

3.2.1 Porosity:

To obtain the optimum porosity in a chemically sintered film containing P25 and smaller titania particles (such as those obtained by hydrothermal processing) Li et al. [57] designed a binary graded structure by theoretical calculation. In their calculation, they consider the volume of the film as unity; and the porosity of P25 particles and the small particles (with a particle diameter of 12 nm) as ε_1 and ε_2, respectively. Assuming that the small particles would exist in the voids between P25 particles, the overall porosity of the

graded film is $\varepsilon_1\varepsilon_2$. When the volume fraction of P25 particles is set as φ_1 and that of the small particles as φ_2 ($\varphi_1 + \varphi_2 = 1$), we get $\varphi_1 = (1- \varepsilon_1)/(1- \varepsilon_1\varepsilon_2)$. To simplify the calculation it was assumed that $\varepsilon_1=\varepsilon_2= \varepsilon$. This then simplifies the volume fractions to $\varphi_1=1/(1+ \varepsilon)$ and $\varphi_2= \varepsilon/(1+ \varepsilon)$.

To identify the range of ε, two pileup modes for particles was considered, cubic and tetrahedral pileup modes which represent the highest and lowest ε for regular packing of uniform spheres. The schematic for these two packing modes is shown in Figure 3.3.

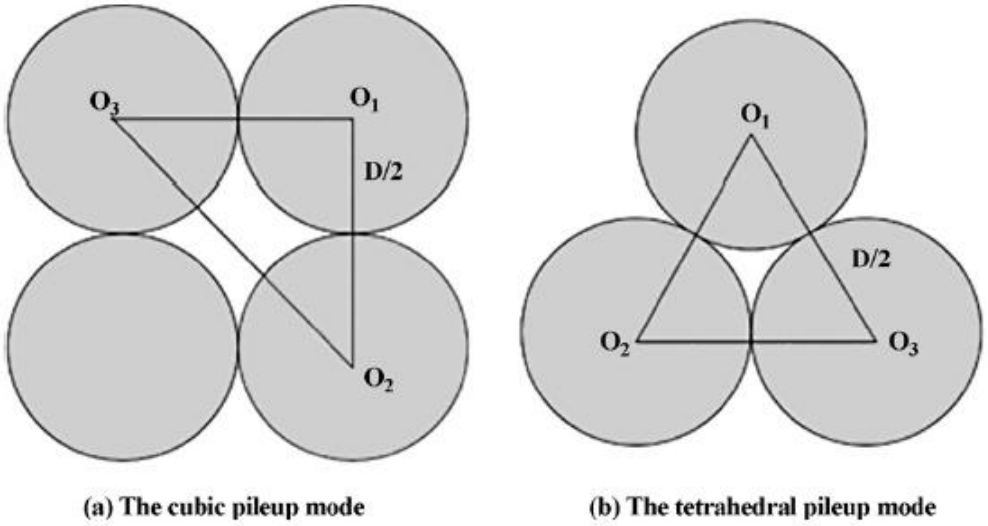

Figure 3.3: Schematic of the particle pileup modes: O_i (i=1-3) represents particle centers and D represents particle diameter [57].

The porosity for the cubic mode of packing is 0.4764 and that for the tetrahedral mode is 0.2595 [58]. Substituting these values into φ_2 would give φ_2=32% when ε=0.4764 and φ_2=20.5% when ε=0.2595. Li et al. [57] conclude that the optimum ε should be in the range between 0.2595 and 0.4764 and the optimum volume fraction of

the small particles should be in the range between 20.5% and 32%. Since the density of the two kinds of TiO_2 particles can be regarded as the same, the optimum weight content of the small particles is also in the range between 20.5% and 32%. Experimentally the optimum weight content of the small particles was found to be 28.5% for maximum DSSC efficiency [57]. This value is consistent with our experiments where the 25wt% TTIP sample was our best, as described above in section 2.3.3.

3.2.2 Pore size distribution:

In a low temperature chemical sintering process such as the one being discussed, two significant processes are happening simultaneously:

a. The redistribution of the reactive solution within the microstructure due to surface tension factors and

b. Reaction of the precursor (hydrothermal process) to give the desired product (titania)

The redistribution of the liquid phase around the host particles (say P25) determines to a large extent the final pore size distribution in the layer. Figure 3.4 [59] shows the different stages in the filling of interstices in a 2-D array of circular particles with a liquid. As the volume of liquid is increased, first the filling of isolated necks happens and then the filling of pores occurs. In the regime where the liquid is situated only at isolated necks, there is a driving force to redistribute an inhomogeneous distribution of liquid homogeneously because the curvature of the contact points (neck regions) between the spheres is very high [59]. The liquid phase can distribute itself in one of three ways as indicated in Figure 3.5.

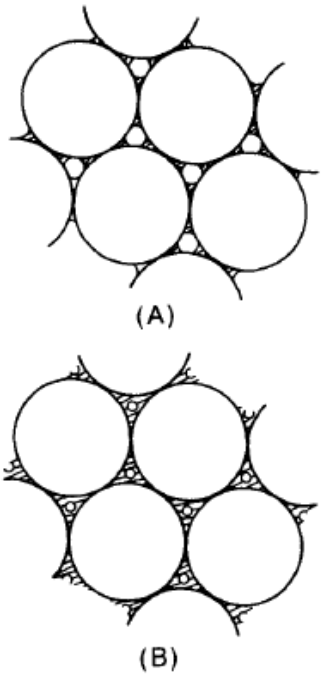

Figure 3.4: Different stages in filling of interstices in two-dimensional array of circular particles with liquid; (A) filling of isolated necks and (B) filling of pores [59].

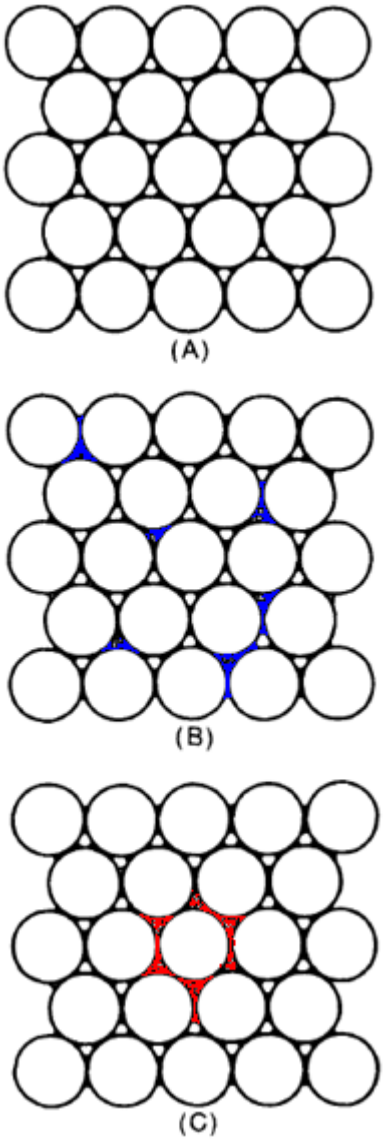

Figure 3.5: Possible equilibrium configurations that can be adopted by liquid in close-packed array of particles; (A) isolated necks filled with liquid (B) fraction of pores completely filled with liquid (pore filling shown in blue coloration) and (C) same as (B) but with inhomogeneous liquid distribution (pore filling shown in red coloration) [Figure adapted from Ref. 59].

In a dye sensitized solar cell, the pore size distribution is also important. It affects the dye adsorption process and limits the mass transport in the redox system that regenerates the dye after the photoinduced electron transfer to the TiO_2 . Both mesoporosity and macroporosity of the titania electrode have been found to be important. [60,61]. The TiO_2 layer needs to be *mesoporous* (2-50 nm range of pores) to allow effective adsorption of dye molecules across the TiO_2 surface [62,63]. The photocurrent output of the solar cell is directly related to the light harvesting efficiency of the dye which in turn depends on the amount of dye adsorbed on the surface of TiO_2. The TiO_2 layer needs to be macroporous (>50nm sized pores) to allow the redox electrolyte to permeate into the entire structure of the TiO_2 coating and be in intimate contact with the TiO_2 nanoparticles [62,63].

3.3 Particle interconnections

To achieve good interconnections (necking) between particles in a chemical sintering process with a liquid titania precursor, it is important to have the liquid wet the particles completely. Figure 3.6 shows the contact angles for good wetting and poor wetting. A low contact angle induces liquid spreading over the solid providing capillary attraction to bring the particles (aggregates) together. A high contact angle indicates poor wetting, so the liquid retreats from the solid [64] and can even push the solid particles apart.

When a small amount of liquid is introduced between solid surfaces a stable liquid bridge can form. An effect of the capillary action of the liquid is to produce a resultant force between the bodies. The capillary force arising from the liquid-vapor

surface tension is shown in Figure 3.7. For a wetting liquid, the capillary forces pull the particles together and causes pore filling. Small pores fill first since they have the highest capillary attraction for the wetting liquid [64]. The challenge in a sintered microstructure is to provide an interconnected network of particles while still maintaining the desired porosity in the film.

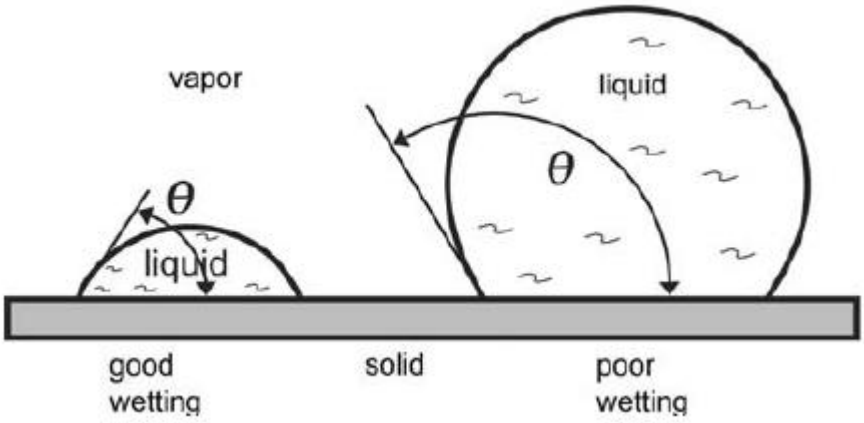

Figure 3.6: Wetting behavior for a liquid on a horizontal plane showing how a low contact angle supports wetting while a high contact angle resists wetting [64].

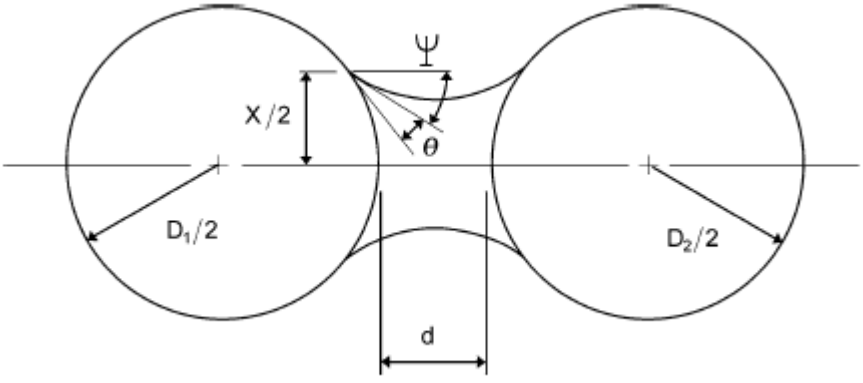

Figure 3.7: Schematic of two spheres of size D_1 and D_2 with a connecting liquid bridge – d is the interparticle distance [64].

In chapters 4 and 5, we will discuss all the above factors using silica as a host material. In chapter 4 we will discuss the effect of silica particle morphology, surface area and pore structure on the performance of dye sensitized solar cells in silica-titania core-shell type structures. In chapter 5 we will probe deeper into the silica-titania microstructure in order to better understand the process of formation of interconnections in a chemical sintering process.

Chapter 4. Silica-titania multilayers prepared using silica particles and titanium alkoxide

In this chapter, the preparation and characterization of silica-titania DSSC microstructures is discussed. In the P25:TTIP system described in Chapter 2, it is difficult to distinguish what part of the microstructure came from the initially crystalline P25 titania and that which has formed from the TTIP. Both titania sources are very similar in the SEM or XRD because of lack of clear contrast between the commercial P25 and the hydrothermally formed material. In order to understand the formation of particle interconnections due to the hydrothermal treatment of the titanium alkoxide, we have designed model experiments where we substituted the P25 commercial nanopowder with monosized silica spheres. Silica was chosen because it is inert under the experimental conditions of this study. Initially, 500 nm size spherical silica particles were used to enable easy identification of titania formed by reaction of the TTIP. Further experimentation was performed with silica particles of different sizes and morphologies to understand the effect of the solid matrix particle morphology on the placement of the reacted material and the performance of dye sensitized solar cells that are formed.

Figure 4.1 shows a schematic of a dye sensitized solar cell with a pure titania based DSSC and a silica-titania based DSSC. The silica particle framework of the composite electrode provides an additional process variable that can help deliver an increased surface area of titania for dye attachment and can reduce the amount of titania required as compared to the conventional titania-based electrodes. In addition, if the titania has good coverage of the silica skeleton, then the conduction pathway to the transparent front electrode may be well interconnected and allow for good current harvesting.

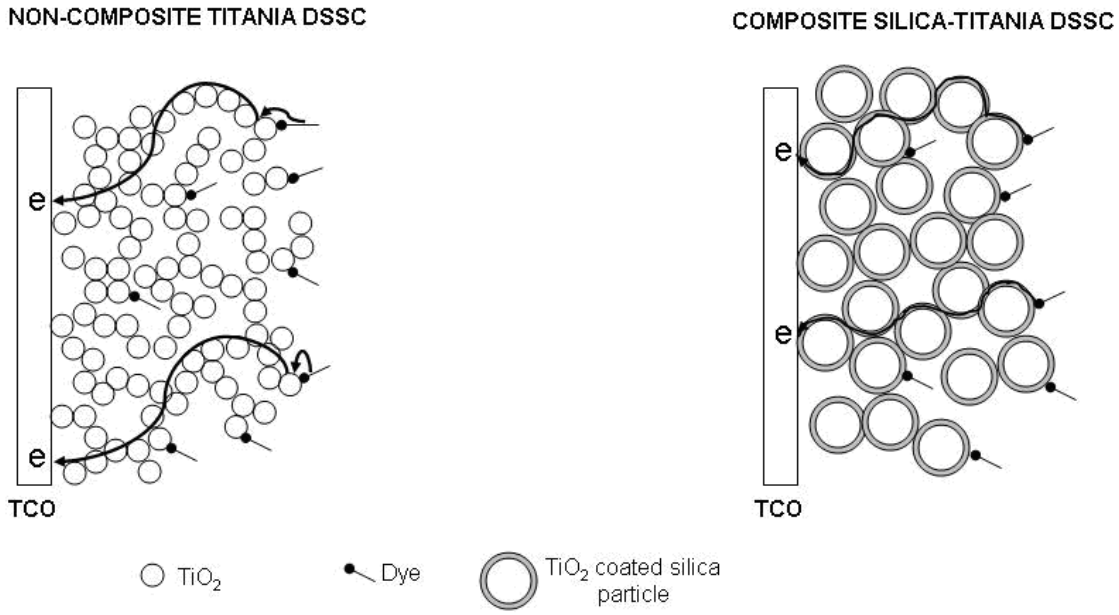

Figure 4.1: Schematic of a titania based DSSC and a silica-titania based DSSC.

4.1 Preparation of silica-titania powders and multilayers

TTIP and ethanol were purchased from Sigma-Aldrich. The substrates used for the experiments were FTO coated glass ($10<R<20\Omega$/sq) obtained from Flexitec Eletrônica Orgânica Ltda. Silica particles of various sizes and morphologies were purchased from Alfa Aesar. Ruthenium-535 bis TBA dye and sealing material (SX1170-25) for dye sensitized solar cell assembly were obtained from Solaronix SA. Chemicals used for the electrolyte, namely LiI, I_2, acetonitrile, 3-methoxypropionitrile and 4-tertiary butyl pyridine, were purchased from Sigma-Aldrich.

A 1M solution of titanium tetraisopropoxide (TTIP) in ethanol was prepared. A well-mixed dispersion of silica particles in 1M titanium isopropoxide solution was prepared in the desired weight ratio (i.e. for a weight ratio of 1:9 of silica:TTIP; 0.4g of

silica powder is added to 3.6g of 1M TTIP solution)[5]. Initially 500 nm mono-sized silica particles were used. There should be minimal amount of TTIP exposure to the atmosphere during the preparation of this dispersion to prevent hydrolysis of TTIP. Blade coating is performed by placing a few drops of the dispersion on the FTO glass slide and using a sharp blade to spread the dispersion onto the glass slide. This process can be repeated depending on the desired thickness of the films. The substrates were placed on a Petri dish and exposed to steam by suspending them on a beaker containing approximately 50 mL DI water. The hotplate was set to 130 °C to boil the water and provide a steam treatment to the coating. This treatment was carried out for 2 hours. It is believed that the steam treatment helps with the hydrolysis of the precursor probably due to the large availability of 'OH' groups for reaction. The possible reaction steps have been elucidated in Chapter 2. (Section 2.2.3: Chemistry and Mechanism). Upon condensation, the Ti-monomers are converted to TiO_2 at the grain boundaries creating the necking of the particles [41]. At the end of this process, the samples were removed and heated in air at 500 °C for 30 minutes, to completely convert any amorphous titania formed to its crystalline phase. The microstructure of the coatings was analyzed using the SEM. To determine the crystalline phase of titania by XRD and to obtain specific surface area, silica-titania powders were prepared by subjecting the silica-TTIP dispersion to the same heating/chemical schedule. Although the broader focus of this study is in low temperature chemical processing methods to make titania interconnections, higher sintering temperatures were used to get crystalline titania.

[5] This translates to an expected silica:titania volume ratio of 2.7:1.0.

4.2 Characterization of silica-titania powders and multilayers

4.2.1 Physical characterization (Morphology, phase and surface area)

The thickness of the silica-titania layers was determined using a Tencor Alphastep 200 profilometer. Scanning electron microscope (GEMINI ZEISS FESEM) with an Everhart-Thornley detector was used to study morphology of nanoparticle structures and interconnections. All samples were coated with a thin layer of gold using a sputter deposition system. X-ray diffraction using a Siemens Kristalloflex diffractometer with a Cu Kα source at 40 kV and 30 mA was used to study composition and crystallinity of the silica-titania materials. The specific surface area of the powders was obtained using a Micromeritics Gemini 2375 BET surface area analyzer.

The SEM images of the silica-titania multilayers for high and low magnification is shown in Figure 4.2. The formation of a chain of interconnected silica particles bound together by the titania is clearly seen. The titania formed by the hydrolysis of titanium isopropoxide and further oxidation serves to form interconnections between the silica particles leading to neck region bridges between the silica particles. The smooth surface shapes near the necks suggest that the titania wets the silica surface well. Also, the lack of compositional contrast in this image supports the conclusion that titania has covered the silica particles well.

To confirm that the interconnections (necking) are indeed the result of titania formation, we looked at a silica layer that was prepared exactly as described in section 4.1 except that no TTIP (titania precursor) was used in the solution. The SEM images of these pure silica layers are shown in Figure 4.3. As can be seen from this figure, no long range connectivity is observed thus confirming that the titania formed from the steam

treatment/heat treatment process serves to connect the silica to each other. For the silica-titania layer to be used as an anode in a DSSC, it is required that the long range connectivity provided by the titania extends throughout the silica-titania layer so that electron conduction to the FTO substrate can occur. To confirm this we looked at cross-sectional SEM of the silica-titania layers. Figure 4.4 depicts the cross sectional images. It can be seen that the necking is continuous throughout the thickness of the coating reaching down to the FTO coated substrate.

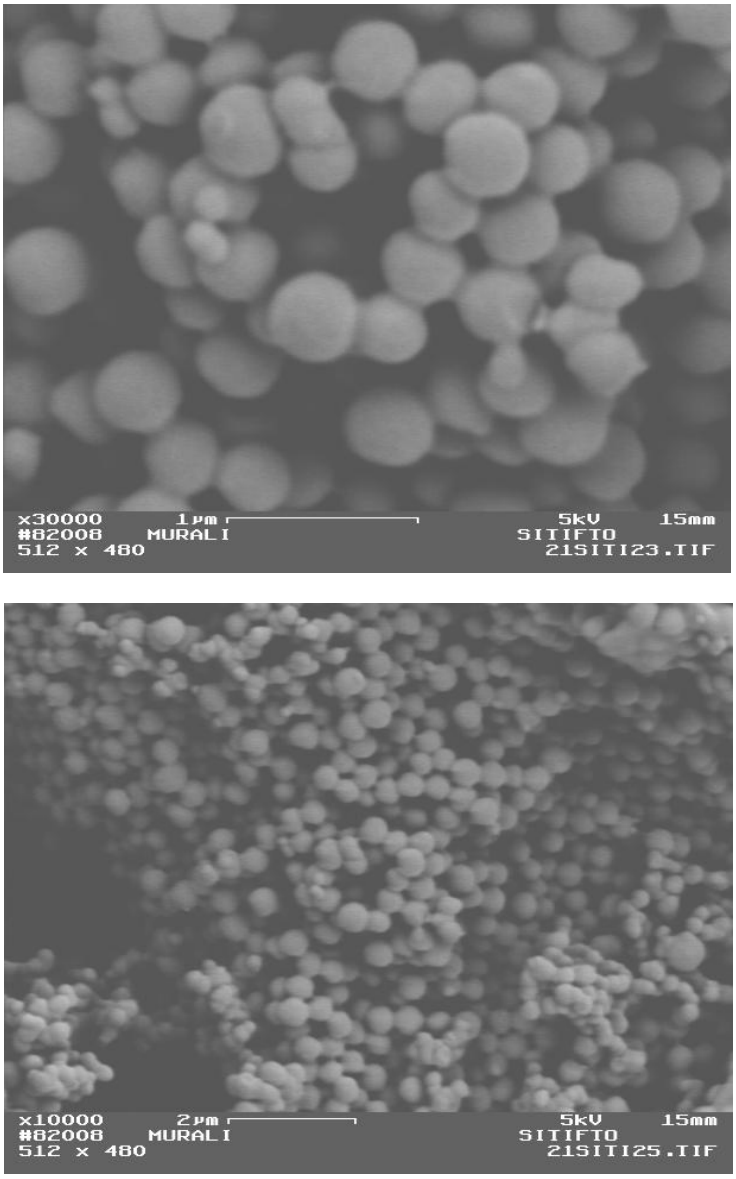

Figure 4.2: SEM images of silica-titania layers.

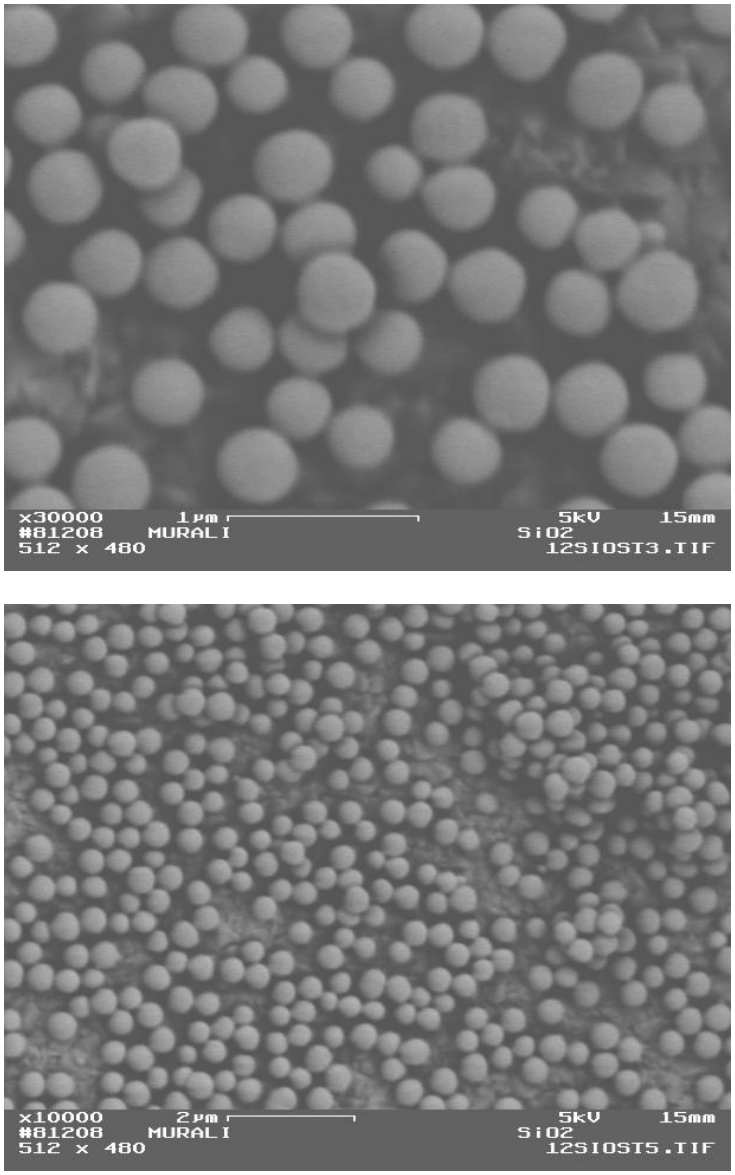

Figure 4.3: SEM images of silica layers.

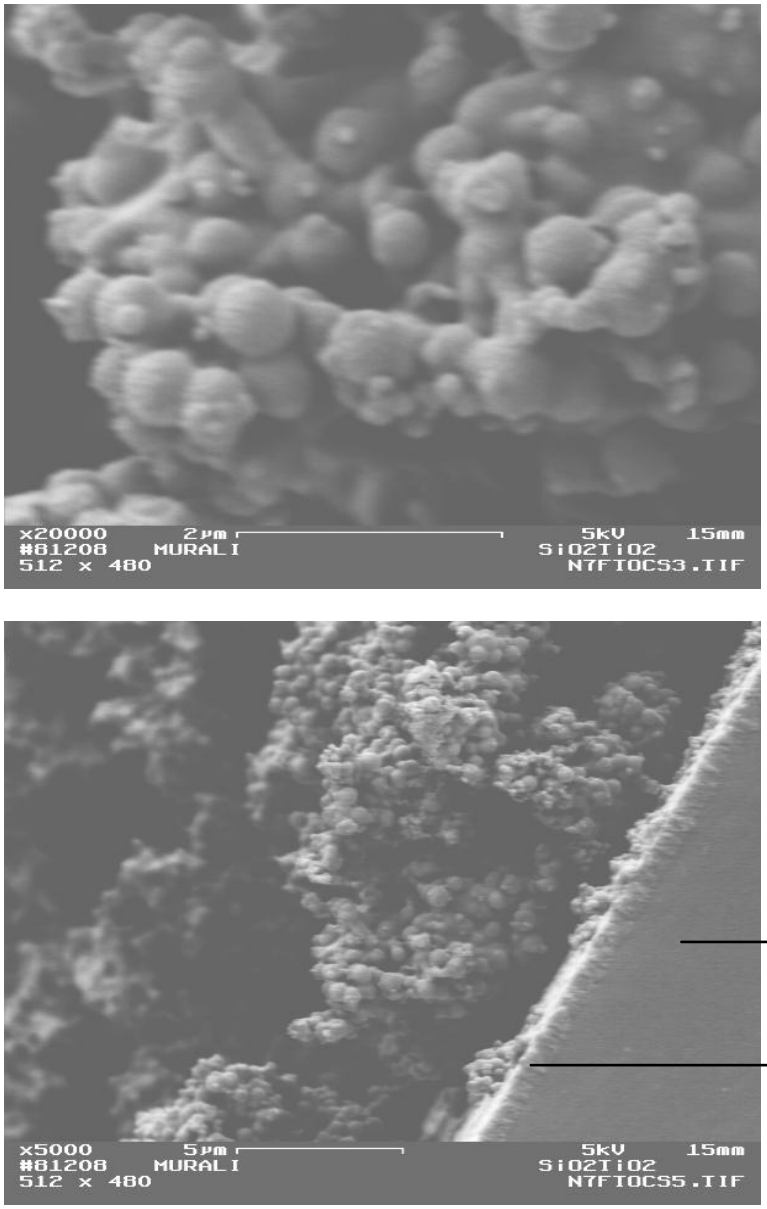

Figure 4.4: Cross-sectional SEM of a silica-titania layer.

The necking of silica particles with titania has also been observed by other research groups. Hanprasopwattana et al. [65] used Stober silica spheres and titanium butoxide for their coatings. They report that the ratio of titanium butoxide to water and the dilution of the reactant mixture in ethanol control the nature of the coatings. If the alkoxide concentration is too high, precipitation of second phase titania particles occurs

rather than a uniform coating. A higher water concentration led to aggregated spheres being connected with titania necks. Isolated silica spheres with uniform coatings of titania were obtained when the alkoxide concentration is kept low.

Khalil et al. [66] prepared silica-titania materials via hydrolyzation of titanium tetra-isopropoxide in a sol of spherical silica particles (Stober particles), followed by drying and calcination of the xerogels at 400 and 600 ˚C. Although they report that some titania particles were aggregating between the spherical silica particles, the necking patterns similar to that shown in Figure 4.2 of this paper were not observed. Instead they observed that the materials consist of a composite of two distinct phases, a spherical silica particles matrix and titania particles between or on the surface of the silica particles.

Fu and Qutubuddin [67] prepared silica-titania by controlled hydrolysis of titanium n-butoxide on monodisperse spherical silica particles also prepared by Stober method. Isolated silica particles with uniform titania nanocoating were obtained by the reaction of butoxide and water at ambient temperature. Higher loadings of titanium butoxide caused necking between silica particles and formation of second phase titania particles.

Thus the formation of interconnections or necking in the silica-titania materials depends on several factors such as concentration of alkoxide, processing temperature and method of preparation of the silica-titania films.

The crystalline phase of the silica-titania powders was obtained by XRD. Since the silica particles are amorphous, XRD characterization would indicate the phase of titania obtained by this method. The XRD pattern of this powder (Figure 4.5) shows the

presence of 100% anatase titania in the powder. The aluminum peaks seen in Figure 4.5 are from the Al sample holder.

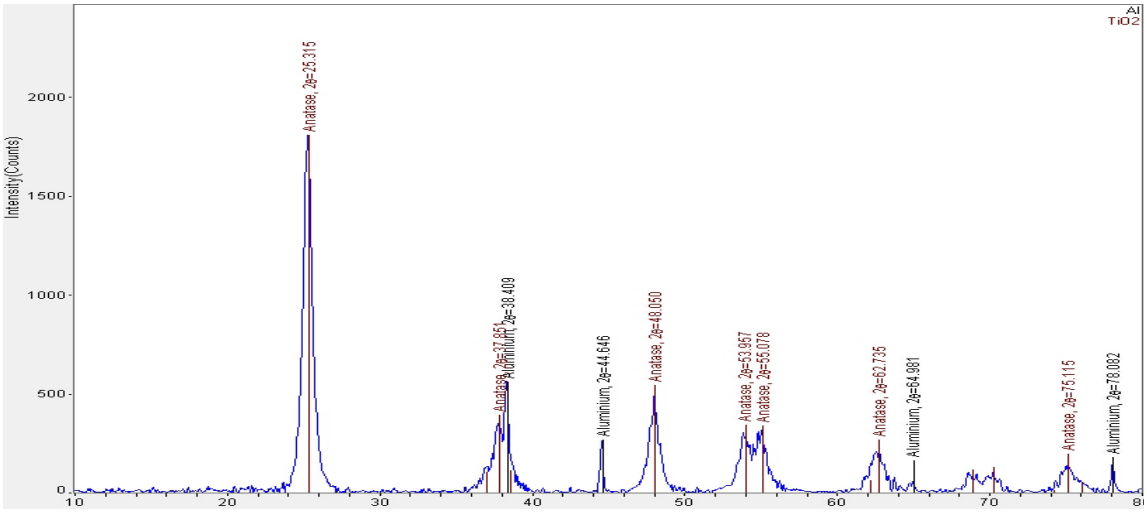

Figure 4.5: XRD of silica-titania powder.

To determine the powder composition and crystallinity at milder sintering conditions, XRD was performed on silica-titania powders that were prepared as described in section 4.1 but sintered at lower temperatures (200 °C, 300 °C and 400 °C) for 30 minutes. The XRD patterns obtained are shown in Figure 4.6. At 200 °C, there is no peak seen and the powder mostly consists of products of incomplete hydrolysis/reaction: visually the powder is light brown in color. The powders sintered at 300 °C look light grayish and seem to have a lot of crystallized powder although some amorphous material still exists. Complete crystallization seems to occur at 400 °C, resulting in a pure white powder. The XRD pattern obtained at 400 °C is consistent with other literature reports [68-70].

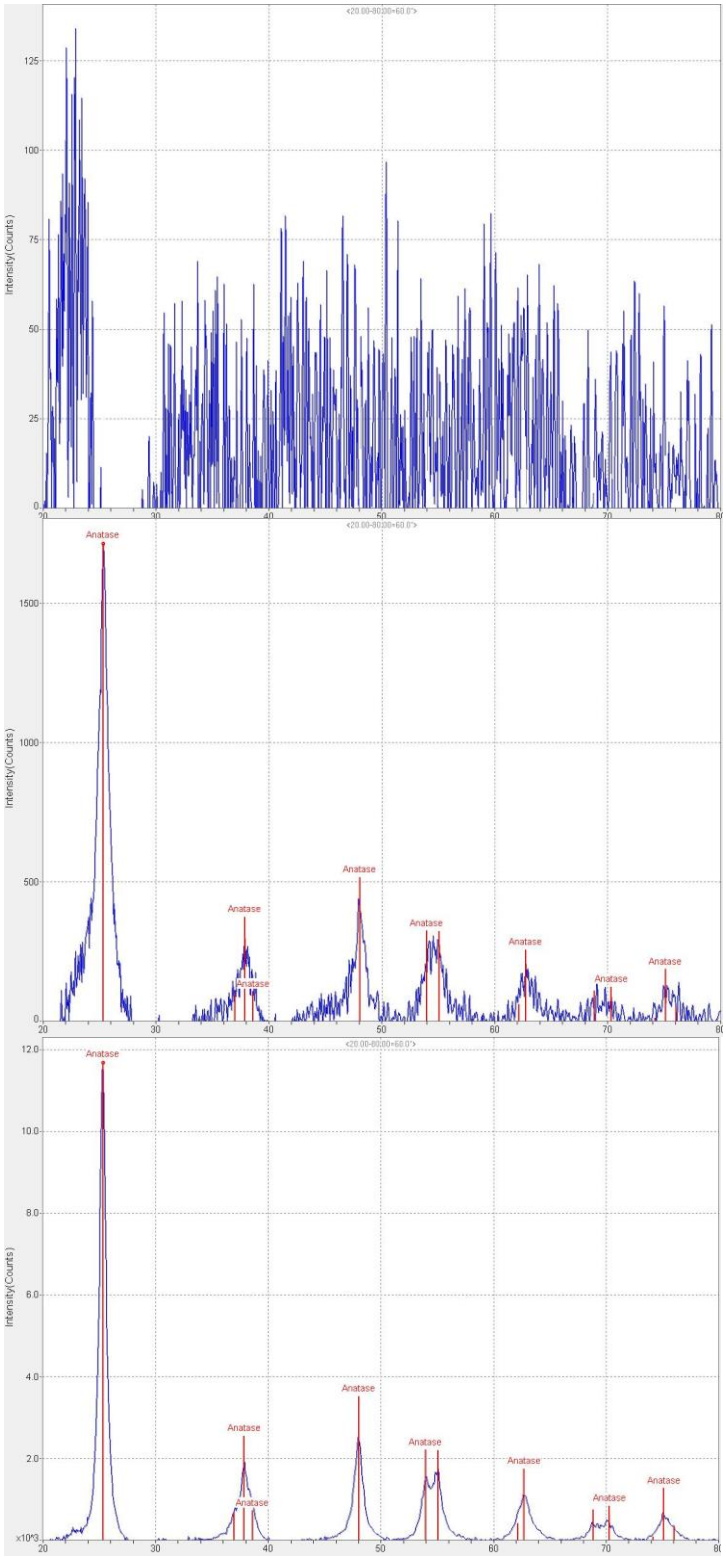

Figure 4.6: XRD of silica-titania powders obtained for sintering temperatures of 200, 300 and 400 °C (top to bottom).

4.2.2 Electrical characterization (I-V DSSC data)

The silica-titania layers prepared by the steam treatment and heat treatment process described in section 4.1 were then soaked in a ruthenium based dye solution for 12 hours. The dye is a solution of 0.21 mM ruthenium 535-bis TBA (commonly called 'N719'; chemical formula: *cis*-bis (isothiocyanato)bis(2,2'-bipyridyl-4,4'-dicarboxylato)-ruthenium(II)bis-tetrabutyl-ammonium) in ethanol. The coated glass slides were removed from the dye solution, rinsed with ethanol and dried in air and used as the anode. Platinum sputtered on FTO (fluorine-doped tin oxide) coated glass was used as the cathode. The electrodes were assembled using a 25 μm thick thermoplastic hotmelt sealing foil (Solaronix SA). The assembled cells were heat treated at 105 °C for 20 minutes to melt the sealant and thereby seal the electrodes together. The electrolyte was injected into the gap between the electrodes by capillary action and the edges were sealed with a polymer hotmelt. The electrolyte had the following composition: 0.5M LiI, 0.05M I_2, 0.05M 4-tertiary butyl pyridine in 5ml each of acetonitrile and 3-methoxypropionitrile (total solvent volume is 10 mL). The cells were tested using an Oriel Solar Simulator (equipped with AM 1.5 filter) for an input power of 90 mW/cm^2.

The I-V curve obtained for this cell is shown in Figure 4.7. The V_{oc}, I_{sc} and fill factor of the cell were 0.6V, 2.47 mA/cm^2 and 0.52 respectively. The solar cell efficiency was 0.86%. The low efficiency of the cell is attributed to the lower amounts of titania in the silica-titania layer which leads to low dye adsorption. It is expected that the efficiency of silica-titania will increase if the ratio of TTIP to silica is increased. The morphology and porosity of the silica particle also play a role – this is explained further in section 4.2.3.

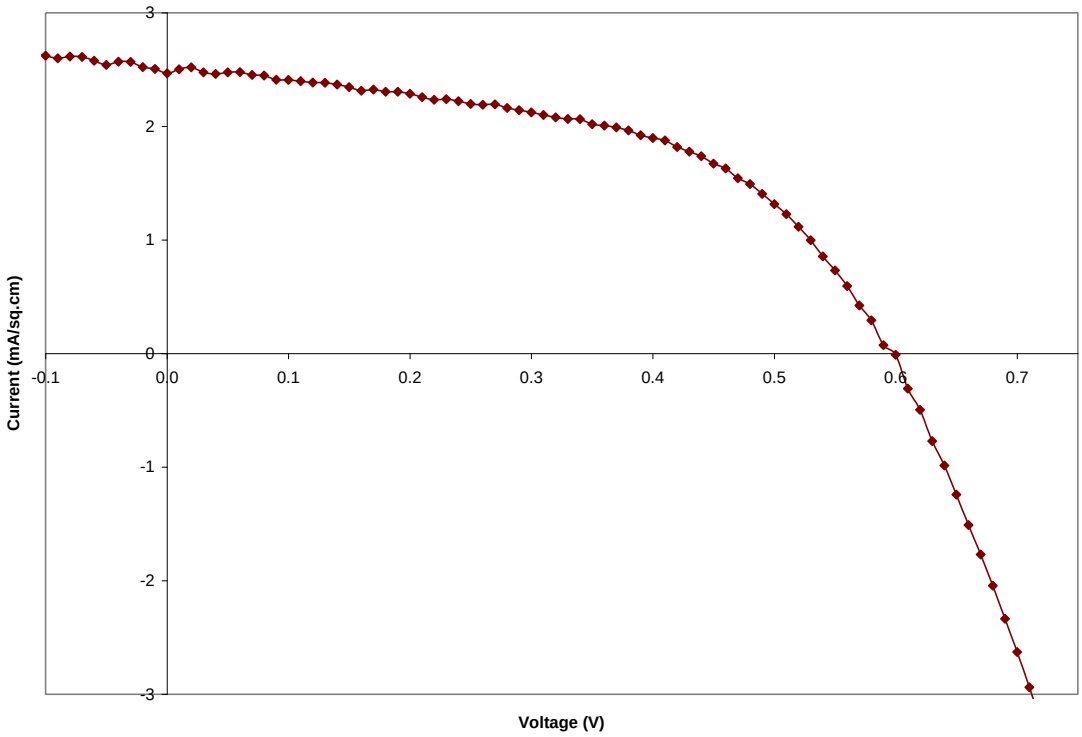

Figure 4.7: I-V curve of a silica-titania based dye sensitized solar cell.

4.2.3 The Importance of silica morphology in the performance of silica-titania DSSC

To observe the effect of silica particle structure on the performance of the silica-titania based DSSCs; we have used silica particles of different sizes and morphologies. Initially, we started off with 500 nm spherical silica particles. Since the efficiencies with the 500 nm silica particles was only around 0.86% we decided to use smaller silica particles with the expectation that the smaller silica particles would be able to support more titania and provide an increased surface area of the titania. The silica powders had a particle size of 500 nm, 20 nm and 80 nm respectively (data provided by Alfa Aesar).

Silica-titania layers using the three silica powders were prepared as described in section 4.1. Characterization was performed using SEM and BET and the layers were tested in DSSCs using the method described in section 4.2.1 and 4.2.2.

Figures 4.8, 4.9 and 4.10 are SEM images of silica-titania layers obtained using each of the silica powders. The silica-titania coating prepared using the 500 nm spherical particles (Figure 4.8) look like connected chains of particles while the coatings prepared using the 20 nm and 80 nm particles seem to be more aggregated with little long-range connectivity between the aggregates. As illustrated in Figure 4.1, a continuous chain of titania is essential for good electron conduction pathways and the morphology of the 500 nm silica based electrode has the best connectivity between particles in this respect.

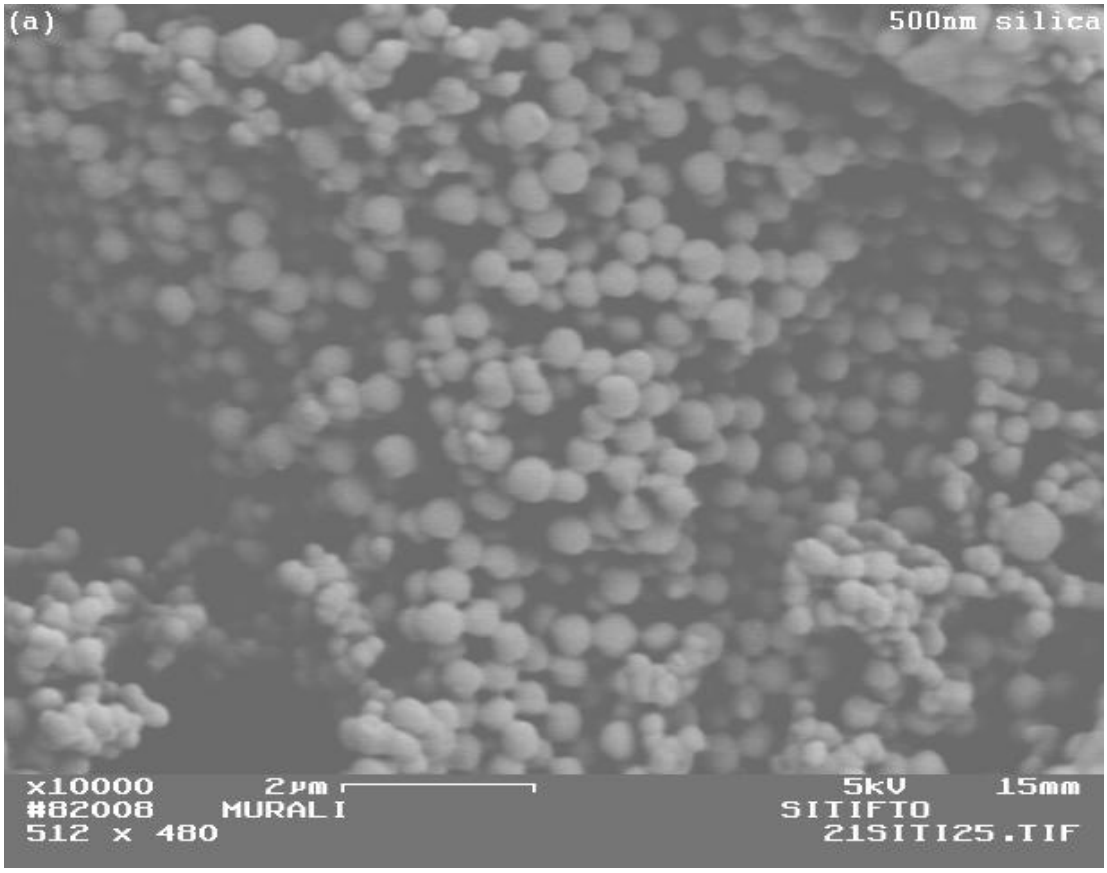

Figure 4.8: SEM image of a silica-titania layer prepared using 500 nm silica spheres.

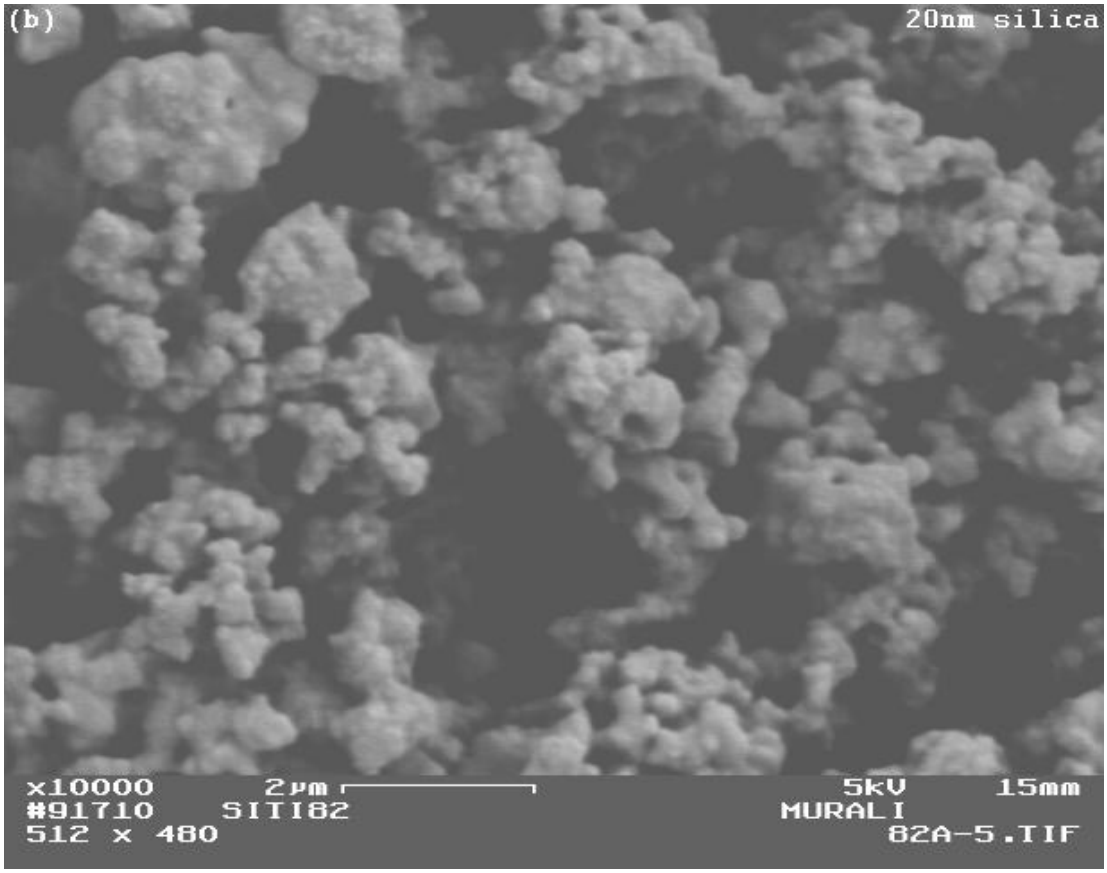

Figure 4.9: SEM image of a silica-titania layer prepared using 20 nm silica particles.

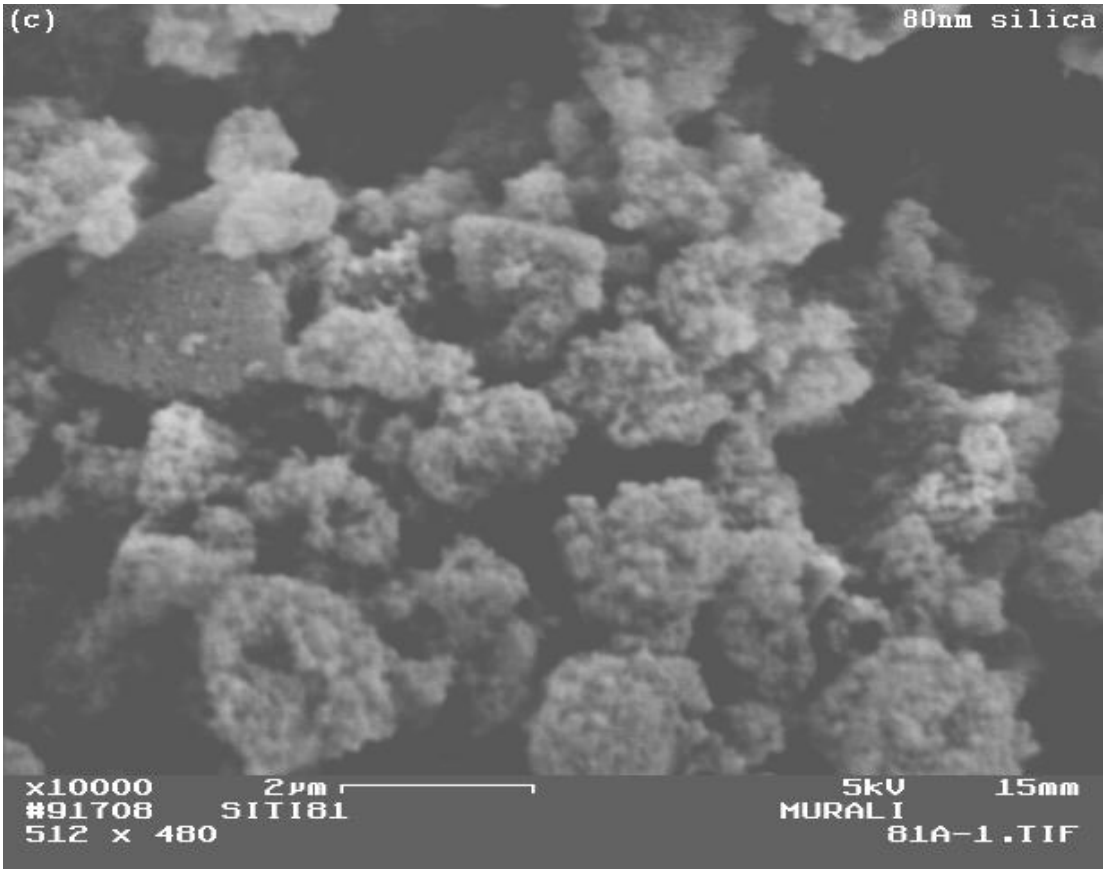

Figure 4.10: SEM image of a silica-titania layer prepared using 80 nm silica particles.

Table 4.1 shows the results of BET specific surface area measurements for the three silica-titania composites. In Table 4.1, the first column indicates the particle size and the second column is the specific surface area data provided by the vendor. The third column is the ideal specific surface area if the silica particles were perfectly spherical. The ideal specific surface area for each particle size is calculated using the formula

$$S = 3 / (\rho * R)$$

where S is the specific surface area of the material, ρ is the density and R is the particle radius. The value of ρ used for calculating S is 2.2 g/cc.

Table 4.1: BET specific surface areas of silica-titania powders

Particle size (nm) *(reported)* of commercial silica powder	Surface area (m^2/g) (*reported*) of commercial silica powder	Ideal specific surface area (m^2/g)	BET specific surface area *(experimental)* of silica-titania powder (m^2/g)
500	2-6	5.5	77
20	160	136	188
80	400	34	179

The powders prepared using the 500 nm silica particles have a tremendous increase in specific surface area when titania is added, suggesting that the titania layer formed from the alkoxide leads to a higher surface area material. The powder prepared with the 20 nm silica particles also shows a significant increase in specific surface area; suggesting that the increase is due to the formation of high surface area titania particles. For the powder prepared with the 80 nm silica particles we first notice that the ideal spherical surface area is much smaller than the actual starting sample, suggesting that the 80 nm particles are actually porous and might be built from aggregates of much smaller primary particles. The specific surface area of the silica-titania powders prepared with the 80 nm silica actually decreases most probably due to some kind of pore-filling mechanism. This can also be observed by looking at the SEM image of the silica-titania layer prepared with the 80 nm silica particles. The morphology of the layer is very spongy suggesting that the 80 nm silica particles themselves are very porous. When the titania is added, we believe the titania solution has been drawn into the tiny scale pore

structure much the way a sponge absorbs fluid. Thus, the titania is filling many of these pores causing the observed reduction in specific surface area.

Dye sensitized solar cells were prepared and tested for silica-titania layers of the three different silica particle sizes and morphologies. The thickness of the silica-titania coating was maintained in the range of 14-18 μm for all three sample types. The results of the DSSC testing are shown in Table 4.2.

Table 4.2: Photovoltaic parameters of DSSC cells prepared with 3 different types of silica particles

Silica particle size (nm)	Silica surface area (m^2/g)	V_{oc} (V)	I_{sc} (mA/cm^2)	FF	DSSC Efficiency (%)
500	2-6	0.60	2.468	0.52	0.86
20	160	0.63	0.492	0.50	0.17
80	400	0.38	0.052	0.33	0.007

The silica-titania samples prepared using the 500 nm silica particles gave the highest efficiency, though still lower than found in pure titania DSSCs. Initially we expected that the smaller silica particles with high surface areas would lead to higher efficiencies (by allowing for greater dye loading) but the actual trend goes in the opposite direction. This could be explained from the SEM images (Figures 4.8, 4.9 and 4.10) and BET data (Table 4.1). The primary causes for poor efficiencies of DSSCs prepared using the smaller (20 nm and 80 nm) silica particles appears to be poorer intergranular connections and pore filling by the resultant titania material.

4.3 Results and Discussion

The 500 nm silica particles are non-porous and have very low starting surface area (2-6 m^2/g). After the formation of titania coatings within these composites, we find nice chains of interconnected particles with the titania around the silica particles being well connected to each other. There is also a substantial increase in specific surface area that makes available a larger amount of titania surface for dye attachment and electron conduction. This is supported by the higher short circuit current and higher efficiency found in these dye sensitized solar cells.

The coatings prepared with 20 nm and 80 nm silica particles show irregular-shaped aggregates that are not well connected to each other. Although the titania has the same chemical synthesis route in all cases, its interaction with the existing silica particles in these two cases results in microstructures that deliver much lower short circuit currents and lower efficiency of DSSCs.

The 80 nm silica particles have negligible DSSC efficiency. There is a significant reduction in the specific surface area and it is apparent that most of the titania has penetrated into the pores and thus not been available for dye attachment and further electron conduction. The morphology, surface area and porosity of the silica particles play a crucial role in controlling the nature of the interparticle connections and the performance of the silica-titania based dye sensitized solar cells. It is desirable to have non-porous silica particles of spherical morphology to begin with and then form a titania layer to obtain a higher surface area with good electron conductivity. It is notable that the titania created in case 1 (silica 500 nm) causes a significant increase in the surface area, suggesting that it is not just forming a continuous smooth coating on the surface of the

spheres. Instead, it seems like the hydrolysis and condensation of the TTIP leads to deposition of material that is itself somewhat porous or perhaps nanoparticulate in nature, which is advantageous for DSSC operation.

It is useful to consider how the titania solution interacts with the different samples during drying and steam treatment, when most of the final coating morphology is established. In addition to the certainty that the titania solution is drawn preferentially into the smallest pores provided by the silica network, it is likely that the capillary forces that this solution experiences during drying and steam treatment can cause imbalances where clumps of particles densify locally, but in the process they also may pull away from their neighbors and give a lower level of long range interconnectivity. This effect was seen most dramatically in the 80 nm silica source material.

The findings of this study have useful implications for any chemical sintering process. In particular, these results could be useful for the low temperature P25-hydrothermal titania process discussed in Chapter 2. This research suggests that instead of using P25 nanoparticles we may be able to improve the efficiencies of the low temperature chemically sintered titania electrode by using larger spherical titania particles and forming a thin high surface area titania superstructure on it by hydrothermal treatments.

Chapter 5. Silica-titania sub-monolayers: microstructural characterization and image analysis

In Chapter 4, we discussed the preparation of silica-titania multilayers and the effect of the morphology of the silica particles on the performance of dye sensitized solar cells. SEM and BET analysis and efficiency data of dye sensitized solar cells suggested that to obtain a good interconnected structure in the electrode it would be beneficial to have spherical host particles with a thin coating of titania.

To probe deeper into the interconnections in the silica-titania layer – specifically the development of interparticle neck contacts -- we conducted a set of studies using single layers of silica-titania deposited on a substrate. This was performed to line up the neck regions for microscopic observation. The preparation of such sub-monolayers and the study of interconnections at a particle-particle level is the focus of this chapter.

5.1 Background

Self assembled monolayers of particles have been studied extensively due to the wide range of applications [71-73]. While monolayers of a single material (oxide or polymer) have been studied widely, to the best of our knowledge, monolayers or sub-monolayers of multi-oxide materials have not been studied to date. Examining the silica-titania submonolayers is therefore an opportunity to study the necking process at the particle-particle level.

Figure 5.1 illustrates a schematic picture of the process of the particle film formation of a monolayer [74]. In the early stage of the process, the particles can move

freely in the liquid film. As evaporation proceeds, oligomer-like deformable loose aggregates partially form in the liquid film, regardless of the particle concentration of the applied suspension, and the upper part of the aggregates protrudes from the liquid layer. The particles in the upper part of the aggregates that have protruded are drawn down by gravitation and capillary immersion force, excluding the underlying particles aside (a). Before the particles reach the substrate below, some of the underlying particles at the bottom protrude from the liquid surface, which are dragged laterally by capillary immersion force (b).

Therefore lateral and longitudinal movements of the particles occur coincidentally to organize the particle monolayer during the final stage of the process. The organization stops when all the dispersion medium evaporates (c)[74].

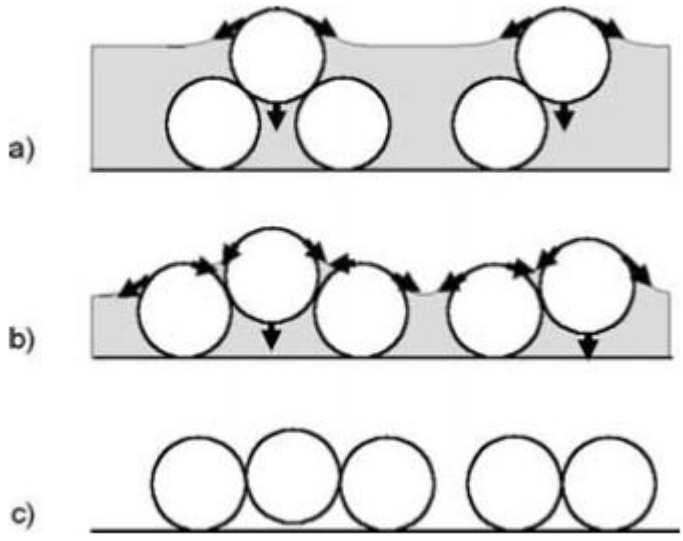

Figure 5.1: Feasible process of the particle film formation; (a) top part of the transient aggregate is drawn downward, (b) longitudinal and lateral particle movements occur coincidentally to organize the particle film and (c) all the dispersion medium evaporates and organization stops. [74].

Most of the techniques used to assemble highly packed monolayers of colloidal particles involve the convective assembling of particles, such as the dip coating method [75-77]. In these methods the substrate is immersed in a colloidal solution and withdrawn vertically or with an angle of inclination at a certain velocity. Another commonly used method is the Langmuir–Blodgett (LB) technique [78–80]. This method is frequently used to prepare monolayers when the target particles have an affinity for the air/water or air/oil interface. The particles are deposited on a liquid film and then compressed by mechanical barriers, then assembled on a substrate by dipping the formed monolayer. Other methods for fabricating particle monolayers, such as the drop coating method [81] and electrophoretic deposition [82] have been reported.

Some of the disadvantages of the above methods include the relatively slow time for the fabrication of a monolayer film, the small area of coating and the non-uniformity of the final monolayer. For a monolayer fabrication technique to be industrially applied, it must be fast, low-cost and must permit a large area (larger than Ø 2 in.) of uniform monolayers to be assembled with high surface coverage. Spin coating method is one such technique that has potential for industrial applications [83].

In sections 5.1.1 and 5.1.2 we provide a background on the particle rearrangement by spin coating and the interparticle neck formation which is related to the formation of pendular liquid bridges between spherical particles.

5.1.1 Formation of sub-monolayers by spin coating

The hydrodynamics involved in the spin coating process have been investigated by various authors [84-85]. During the initial stages of spinning, the thinning is mainly

due to the viscous effects. The centrifugal outflow is more dominant and since the particles are immersed in the solvent, they move around in response to the convective outflow. At a stage in the spin coating process, the convective effect and the simultaneous solvent evaporation are approximately equal in magnitude. This occurs at fluid depths on the order of only a few microns. Beyond this point more thinning occurs by solvent evaporation than by viscous outflow. As the solvent evaporates, the concentration of the particles rises forcing more interparticle interactions to take place [86].

Ogi et. al. [83] investigated the effects of the concentration of SiO_2 particles, the ambient temperature and the relative humidity as well as the spin speed on the surface coverage and the uniformity of monolayers of silica spheres on a sapphire substrate. Aqueous suspensions of silica particles were spin coated onto sapphire substrates in a 2-step spin coating process. Figures 5.2 and 5.3 [83] illustrates the effect of solvent evaporation rate and spin speed on the spin coating process.

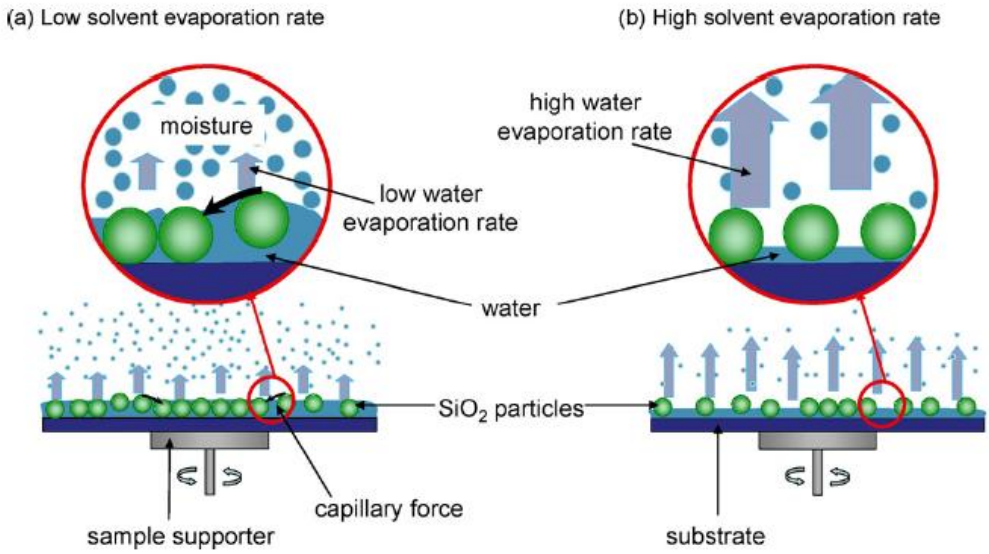

Figure 5.2: Illustration of the effect of solvent evaporation rate on the assembling of particles in a spin coating process [83].

The rate of evaporation of solvent is an important factor in controlling the formation of a particle monolayer during spin coating. When the relative humidity is high (60% RH), the flux of water from the solution to air decreased considerably, and the evaporation process is retarded so that the particles were assembled in an orderly manner by capillary forces. When the relative humidity was changed from 60 to 30%, the number of particles in island-like arrays increased and the surface coverage decreased significantly. This is because the moisture content surrounding the substrate decreased and the water flux increases, thus accelerating the evaporation process before capillary forces became dominant, resulting in island-like assembling of the particles.

It is well known that the regulation of the spin speed is an important parameter in obtaining a uniform coating over large area. Figure 5.3 is an illustration of the forces at play for different spin speeds.

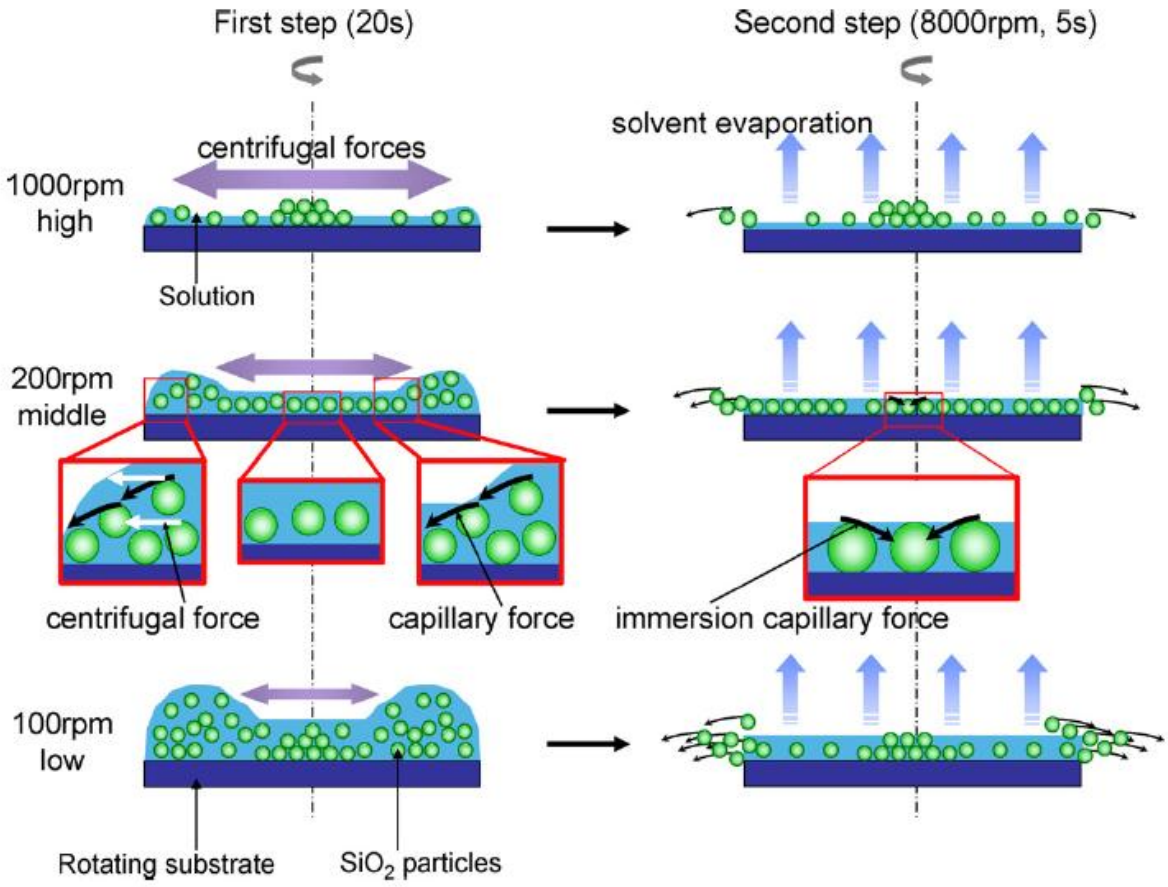

Figure 5.3: Illustration of effect of spin speed on the assembly of particles during spin coating [83].

At lower spin speeds (~100 rpm), the solution height is higher and because of low evaporation of solvent and low centrifugal force, the particle flux toward the edge of the substrate is also low, resulting in a multilayer array in the center and low surface coverage in the radial direction. If the spin speed is too high (~1000 rpm) the centrifugal forces are initially too strong and the evaporation of solvent so fast that a large number of particles are expelled from the substrate and a bilayer array is formed in the substrate center. An optimum spin speed is necessary to get monolayer coverage on the substrate.

In the next section (Section 5.1.2) we will discuss the process of formation of the interparticle necks by explaining the theory of liquid bridges.

5.1.2 Formation of interparticle necks (Pendular liquid bridges)

When liquid is introduced between two spherical particles, it could lead to the development of a stable liquid bridge which produces a resultant attractive force between the two particles. This arises from a pressure deficiency in the bulk of the liquid (the capillary force) and from the surface tension of the liquid acting on the two bodies [87]. The contact between the three phases, solid, liquid, and gas, induces the onset of forces between these particles, which will depend on physical-chemical aspects like the wettability of the particles, the geometry of the meniscus as well as the particles' sizes and the separation between them [88].

Megias-Alguacil and Gauckler [88] have presented the conditions for the formation of pendular liquid bridges between spherical bodies. Figure 5.4 [88] shows a sketch of a liquid bridge geometry. In this figure, R is the solid particle's radius, x_a and y_a are the abscissa and coordinate of the contact point between the solid and liquid profile, respectively, α is the half-filling angle, Θ is the wetting angle, ρ and L are the principal radius of the liquid meniscus, measured orthogonally, H is the surface-to-surface distance between the solid particles, and d is the wetted portion of each hemisphere. The reference system is chosen such that its origin is the middle point between the spheres and the x-axis lies along the straight line which joins the particles' centers, as shown in Figure 5.4.

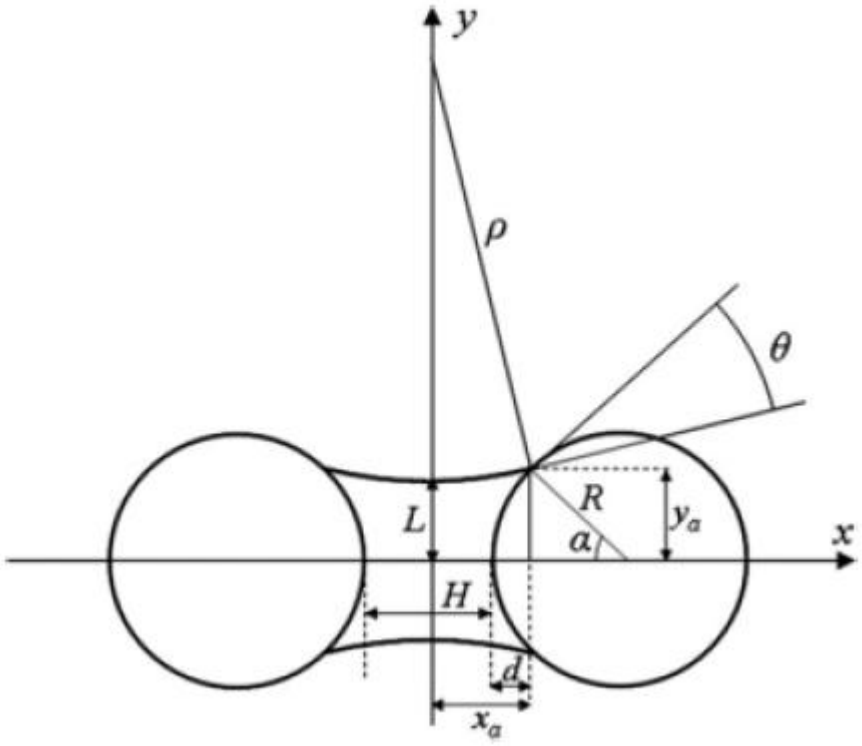

Figure 5.4: Sketch of a liquid bridge geometry [88].

The liquid volume of the bridge, V, may be determined for a given distance between particles, H, by definite integration of both the solid and liquid profiles [88] and substitution of relations for the solid and liquid profiles as is shown in figure 5.5. The liquid bridge profiles for varying H/R ratios, wetting angles and relative volumes were derived and are shown in figure 5.6.

$$V = 2\pi \int_0^{x_a} [y_L(x)]^2 dx - 2\pi \int_{H/2}^{x_a} [y_S(x)]^2 dx$$

$$\frac{V}{2\pi} = \left[(\rho + L)^2 + \rho^2\right] x_a - \frac{x_a^3}{3} - (\rho + L)\left[x_a \sqrt{\rho^2 - x_a^2} + \rho^2 \arcsin\frac{x_a}{\rho}\right] - \frac{(x_a - H/2)^2}{3}[3R - (x_a - H/2)]$$

Figure 5.5: Equations used to calculate volume of a liquid bridge [88].

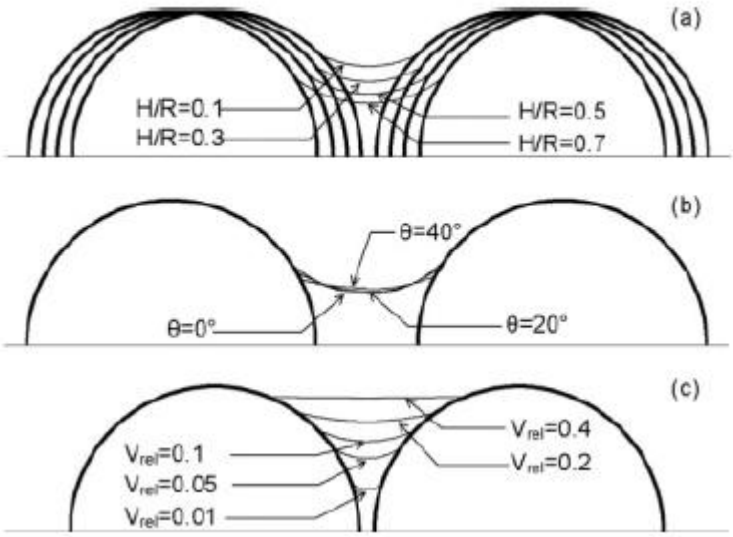

Figure 5.6: Liquid bridge profiles for various parameter values [88].

The following phenomena can be observed from figure 5.6. The overall effect of separating the particles while keeping the liquid volume constant is an elongation of the bridge, which becomes longer and thinner and less concave. Also, the curvature of the liquid bridge decreases as the wetting angle is increased. And finally, increasing the liquid volume causes a thicker meniscus (larger L) as well as an evident reduction of the meniscus curvature (larger ρ). If the amount of liquid is increased sufficiently, it may completely cover the spheres, and beyond this point, the spheres will be fully immersed in the liquid; this situation clearly does not correspond to a liquid bridge anymore. In other words, the bridge may no longer exist under this circumstance [88].

The formation of liquid bridges in a liquid phase sintering process can lead to interparticle necks between the host particles after reaction and heat treatment. From section 5.1.2, we can see that the wetting angle and the concentration of liquid precursor can have an effect on the liquid bridge profiles and thus on the neck formation. In the following sections we will discuss the preparation and characterization of silica-titania sub-monolayers with emphasis on the formation of interparticle necks and quantification of neck widths. Because of the geometry created and the net attractive forces of these pendular bridges then we are always looking at samples where the two spheres touch. This is essentially the special case of H=0 for Megias-Alguacil and Gauckler's treatment [88].

5.2 Preparation of silica-titania sub-monolayers

5.2.1 Materials and Methods

Titanium (IV) isopropoxide (97% assay) was purchased from Sigma-Aldrich. Ethanol (ACS reagent, >99.5% assay) and 1-butanol (99.9%) were obtained from Sigma-Aldrich and used without further purification. Glacial acetic acid was purchased from ACROs Organics. Silica powder (500 nm) was purchased from Alfa Aesar. The plain glass slides that were used as substrates were obtained from Fisher Scientific.

A sol of titanium isopropoxide (varying amounts) was prepared using 0.625mL acetic acid and 9.5 mL of 1-butanol. To this, 0.1g of silica powder was added. The silica powder used for preparation of the sub-monolayers consisted of 500 nm spheres. After stirring for 30 minutes, the solution was spin coated onto glass samples. The glass samples were of the size of 0.25” X 0.25” and were cut from 1mm thick plain glass slides. The glass slide pieces were cleaned with ethanol and dried thoroughly prior to deposition.

The spin coater used is a Specialty Coating Systems model P6700 coater shown in Figure 5.7. A few drops (10-12 drops) of the prepared solution are placed onto the microscope slide piece that is adhered to the coater chuck. The spin speed used is 3000 rpm for 40 seconds. At the end of the coating process, the samples are air dried and further heat treated at 500 °C for 30 minutes.

5.3 Characterization of silica-titania sub-monolayers

After heat treatment the slides were coated with a thin layer (10-20 nm) of iridium to make the samples conductive. The iridium coating was performed using a Gatan model

681 ion beam coater; the coating thickness is approximately 10 nm. A picture of the Gatan ion beam coater used for coating the submonolayers is shown in Figure 5.8. Scanning electron microscope (GEMINI ZEISS FESEM) with an Everhart-Thornley detector was used to study morphology of the sub-monolayer structures. Image analysis was performed on the SEM images using Image J (ImageJ 1.42q; National Institutes of Health, USA). Atomic force microscopy (AFM) was used to look at surface topography and test another means for measuring the size of the neck between silica particles. AFM was performed with a Nanoscope IV (Digital Instruments) in contact mode on 10 x 10 micron area of the sample. HRTEM (High Resolution Transmission Electron Microscope) micrographs were obtained at 200keV in a JEOL 2010F TEM/STEM equipped with Gatan Imaging Filter (GIF) operating in STEM-mode.

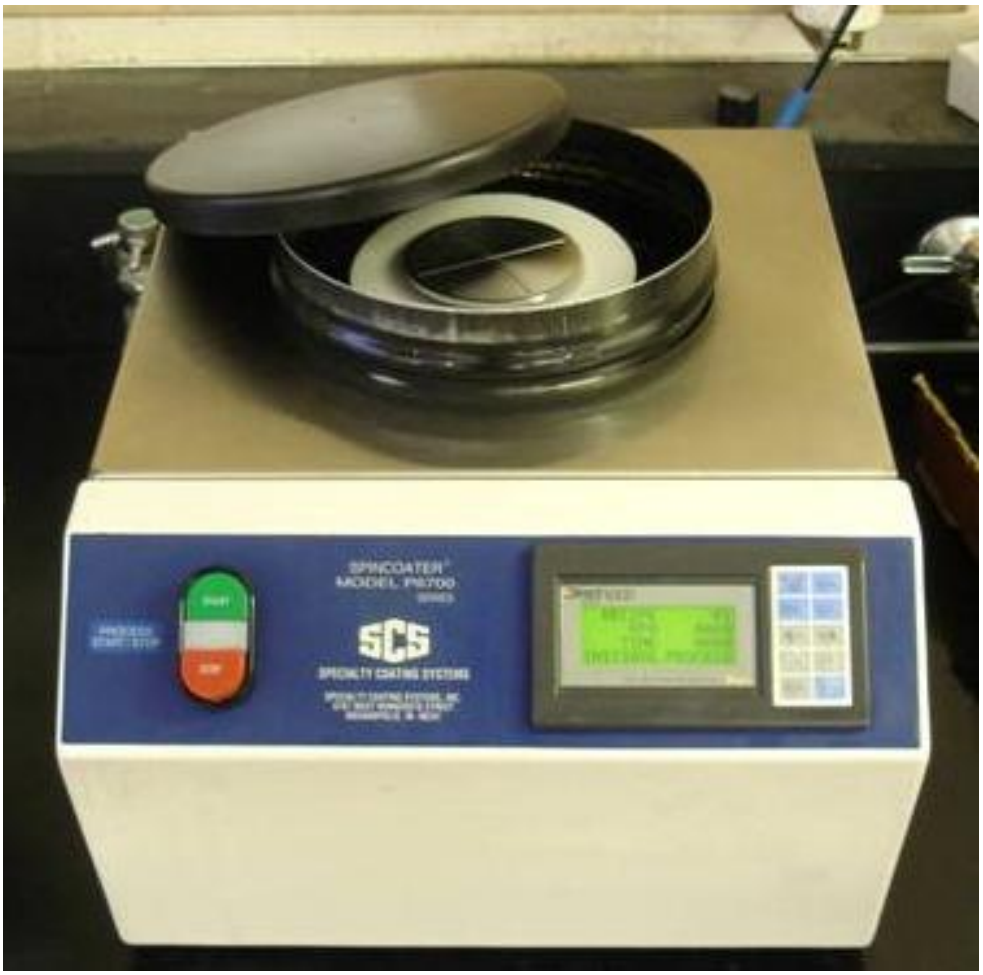

Figure 5.7: SCS P6700 model Spin coater.

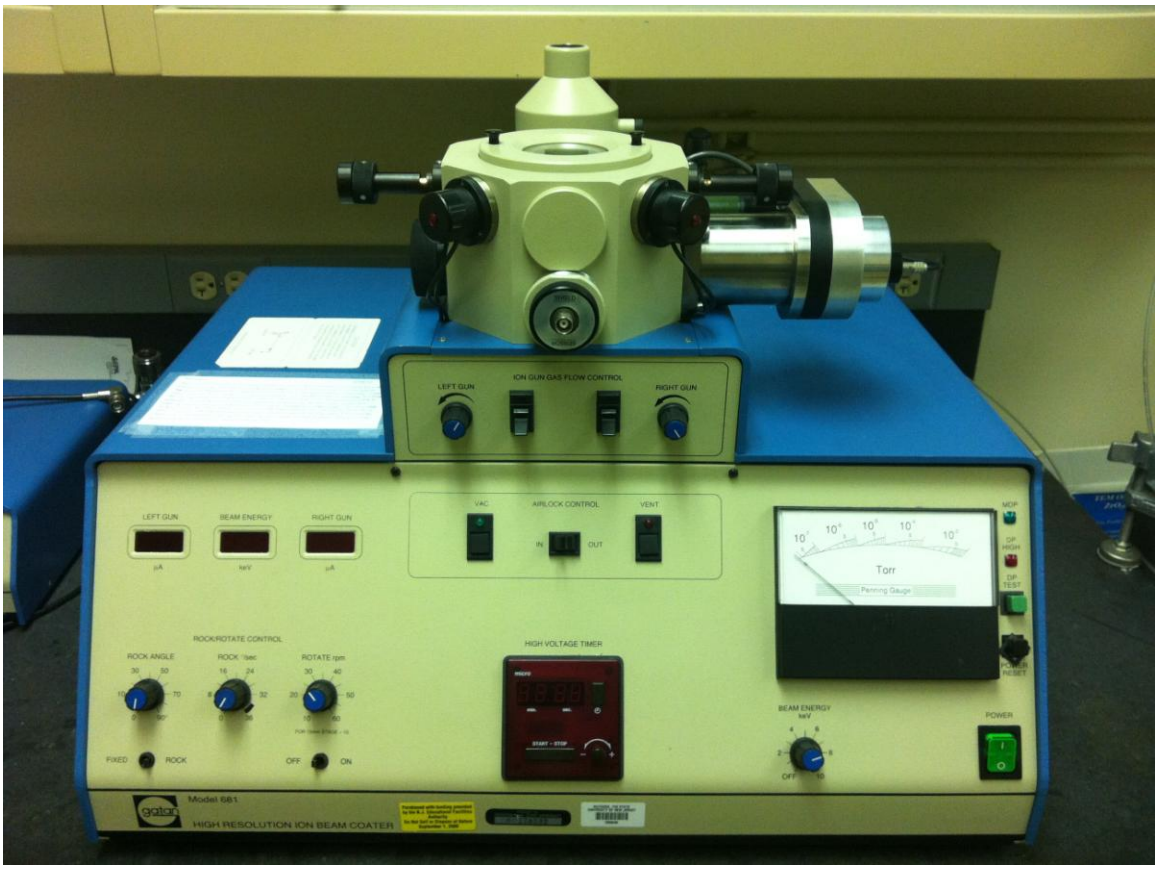

Figure 5.8: Gatan ion beam coater.

5.4 Results and Discussion

5.4.1 Morphology of the silica-titania sub-monolayers (SE detector)

The sub-monolayers of silica-titania were prepared for 7 different amounts of the titanium alkoxide precursor. The amounts of titanium isopropoxide precursor used were 0.75, 0.375, 0.25, 0.125, 0.0625, 0.03125 and 0.015625mL. Initially, we started with the 0.75 mL TTIP concentration to test the possibility of getting sub-monolayer coverage. Once that was achieved, the amount of TTIP was reduced for successive samples because the goal of the experiments was to observe the neck regions but aim for very low surface coverage of titania. For this reason, the amounts of TTIP are indicated in reverse order in the figures and table in this chapter.

The secondary electron (SE) detector of the SEM is used to obtain topographic information The SEM images of the sub-monolayers obtained using the secondary electron (SE) detector for 4 of the ratios of TTIP used are shown in Figures 5.9 and 5.10 for low and high magnification values. The images show that the silica particles are joined together in pairs, triplets and short chains by the titania. In the high magnification Figures of 5.10 we can more clearly see the silica particles joined at the neck by the titania formed by the hydrolysis of the alkoxide and subsequent heat treatment. The smooth surface shapes near the necks suggest that the titanium alkoxide precursor sol wets the silica surface well during the spin coating process.

XRD studies conducted previously on silica titania multilayers (section 4.2.1) have shown that the necks are composed of crystalline anatase titania.

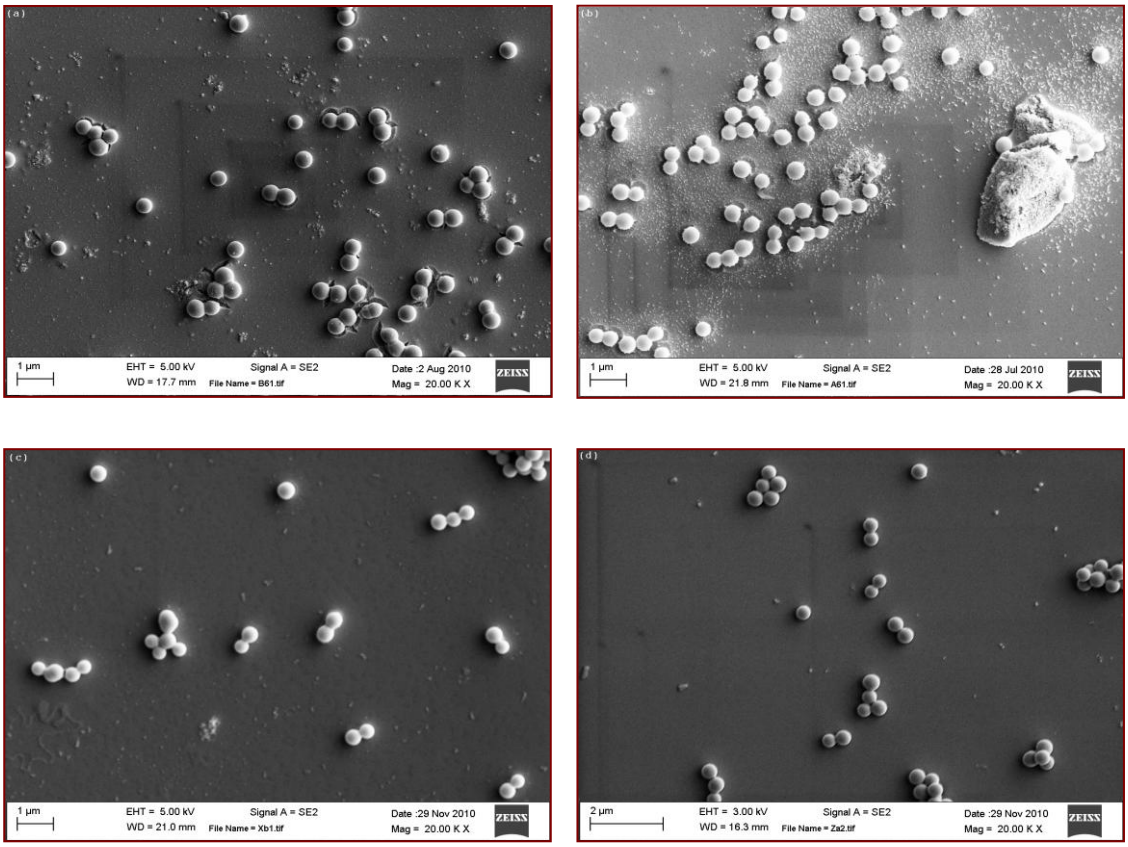

Figure 5.9: SEM images (magnification 20KX) of silica-titania sub-monolayers for 4 different titania precursor amounts (a) 0.75mL (b) 0.25mL (c) 0.0625mL and (d) 0.0156mL.

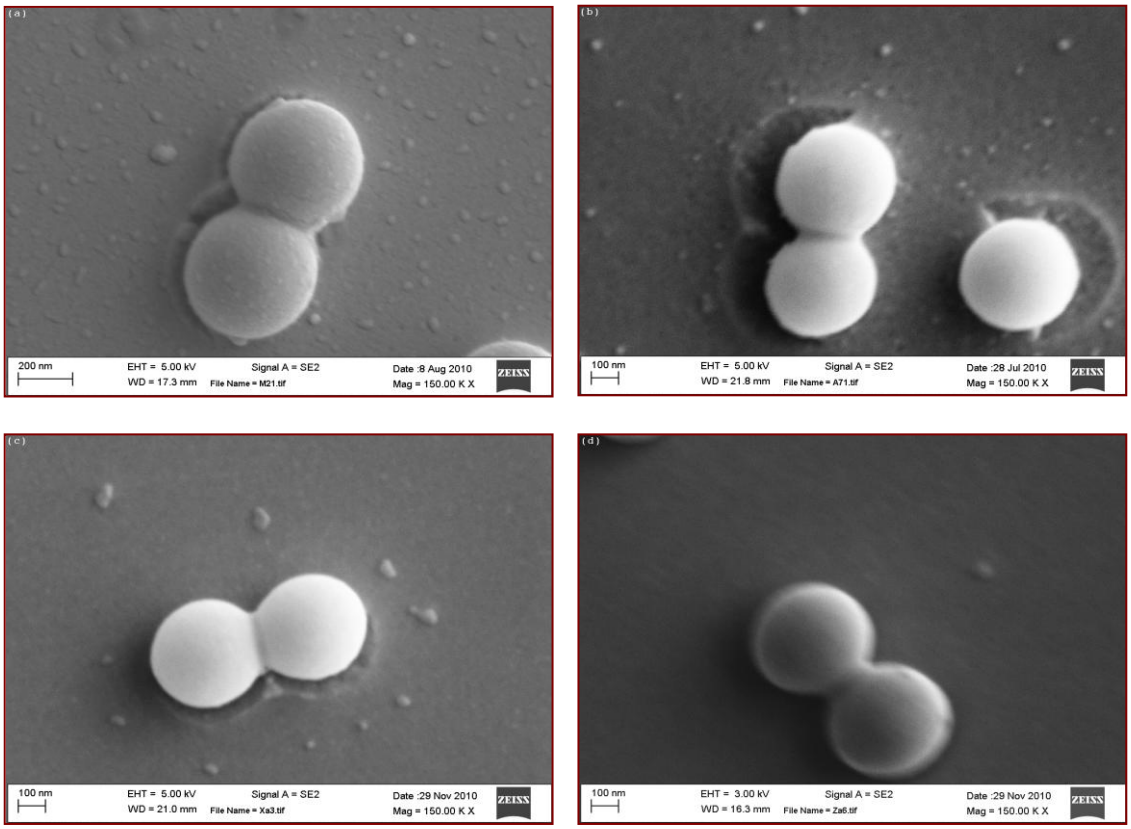

Figure 5.10: SEM images (magnification 150Kx) of silica-titania sub-monolayers for 4 different titania precursor amounts (a) 0.75mL (b) 0.25mL (c) 0.0625mL and (d) 0.0156mL.

To confirm that the neck region is indeed formed by the titania that came from the alkoxide precursor we prepared pure silica layers by spin coating a solution of the 500 nm silica powder in acetic acid and 1-butanol followed by post heat treatment at 500°C for 30 minutes. This procedure is exactly the same as described in section 5.2.1 except that no titanium alkoxide is used in the sol recipe. The SEM image of the sample prepared with no titania precursor is shown in Figure 5.11. In this image, some individual silica particles and some groups of silica particles can be observed. The absence of necking can be seen more clearly in Figure 5.12 where the SEM images of a silica-titania and silica layer have been placed side by side. In the case of the pure silica layer, the silica particles are just touching each other and it looks like the particles have come together most likely due to capillary forces [83,89]; no necking phenomenon is observed in this case which fits well with our observation that in solutions containing the titanium isopropoxide precursor, the titania formed is creating necking between the silica particles.

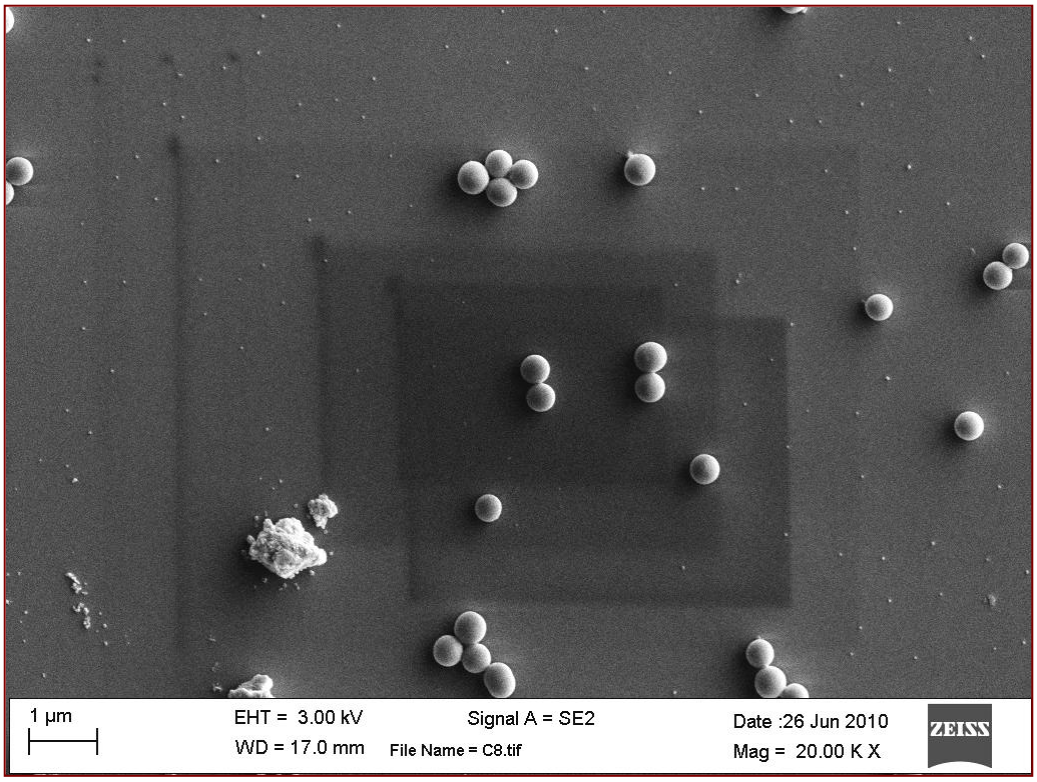

Figure 5.11: SEM image of a silica sub-monolayer prepared without a titania precursor.

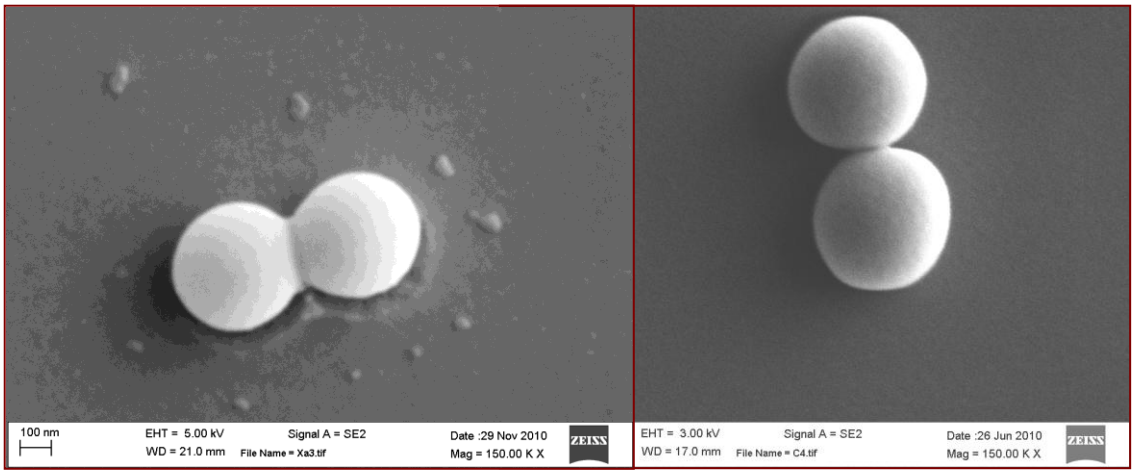

Figure 5.12: SEM image of silica-titania layer prepared with 0.0625mL TTIP (left) and pure silica layer (right).

5.4.2 Morphology of the silica-titania sub-monolayers (In-lens detector)

The in-lens detector of the GEMINI FESEM was used to obtain clearer high-contrast images of the sub-monolayers. In the in-lens detector of the SEM, due to a sophisticated magnetic field at the pole piece, the secondary electrons are collected with high efficiency. In particular at low voltages and small working distances, images with high contrast can be obtained. The drying effects occurring during spin coating and the necking of titania were more clearly observed with the inlens detector.

Figure 5.13 shows the SEM image of a silica-titania sub-monolayer prepared with 0.75mL TTIP and 0.125mL TTIP: both were obtained with the in-lens detector. For the sample prepared with 0.75mL TTIP; the silica-titania layer seems to have cracked due to the drying effect of the solvent evaporation and the post treatment at 500C and this has led to some particle chains being broken at the necks. The same cracking effect can also be seen in the samples prepared with 0.125mL TTIP although the effect is less pronounced in this case.

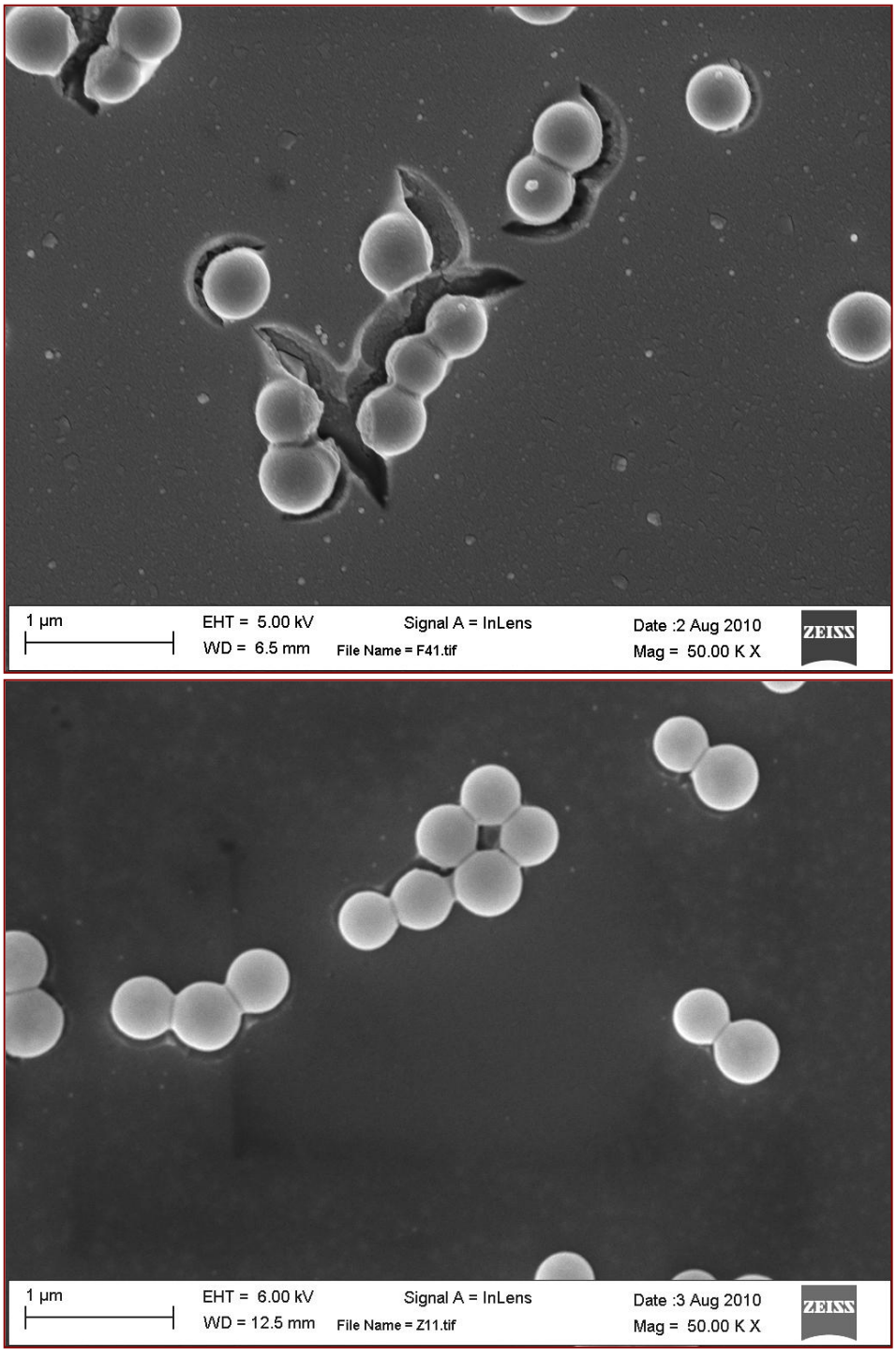

Figure 5.13: SEM image (in-lens detector) of silica-titania sub-monolayer prepared with 0.75mLTTIP (top) and 0.125mL TTIP (bottom).

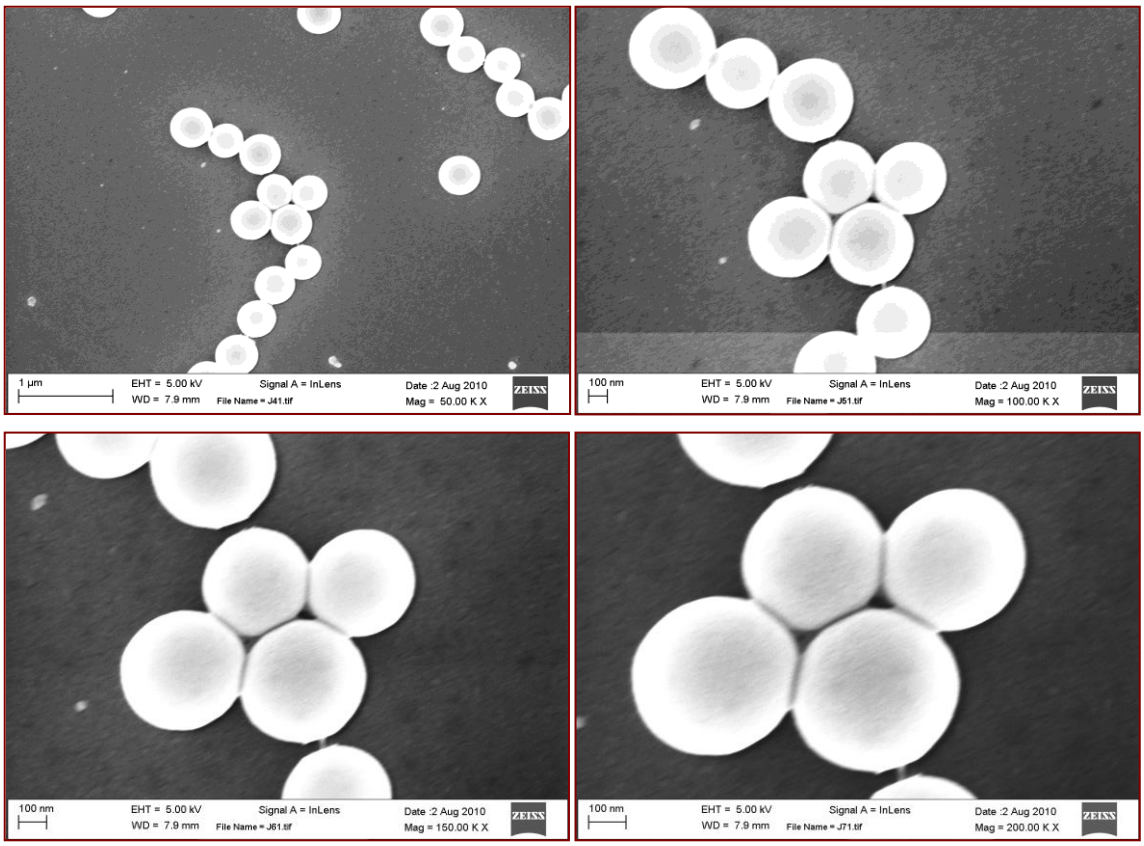

Figure 5.14: SEM image (inlens detector) of silica-titania submonolayers prepared with 0.125mL TTIP.

The in-lens detector images of Figure 5.14 show in more detail the chain formation and breakage at different magnifications. These images of silica-titania sub-monolayers were obtained for a 0.125 mL TTIP precursor in the sol. The high magnification images show the breakaway points of the necks (at the top and bottom) and the low magnification images show the long chains of particles held together by the necks.

5.4.3 Pore size distribution in the silica-titania sub-monolayers

Figure 5.15 shows the SEM images of silica-titania sub-monolayers prepared using 0.0625mL of TTIP in solution. The presence of pores of varying sizes and shapes is observed. The pore sizes were measured using the CARL ZEISS SmarTiff annotation editor (V 1.0.1.2). We can see that both mesopores and macropores are formed in the silica interconnected structure. This dual porosity pore structure combined with the pore formation within the titania itself (micropores and mesopores) shows that there is a range of porosity that can be obtained in these sub-monolayers. We expect similar distributions in pore shape and size for the three dimensional samples.

The pore structure is affected by several factors during deposition including wetting angles, ratio of silica to titania precursor, evaporation rates of solvents in the sol recipe, surface tension and spin coating parameters. By controlling these factors, the pore size distribution of the silica-titania interconnected structure can be tailored both in monolayered and multilayered structures.

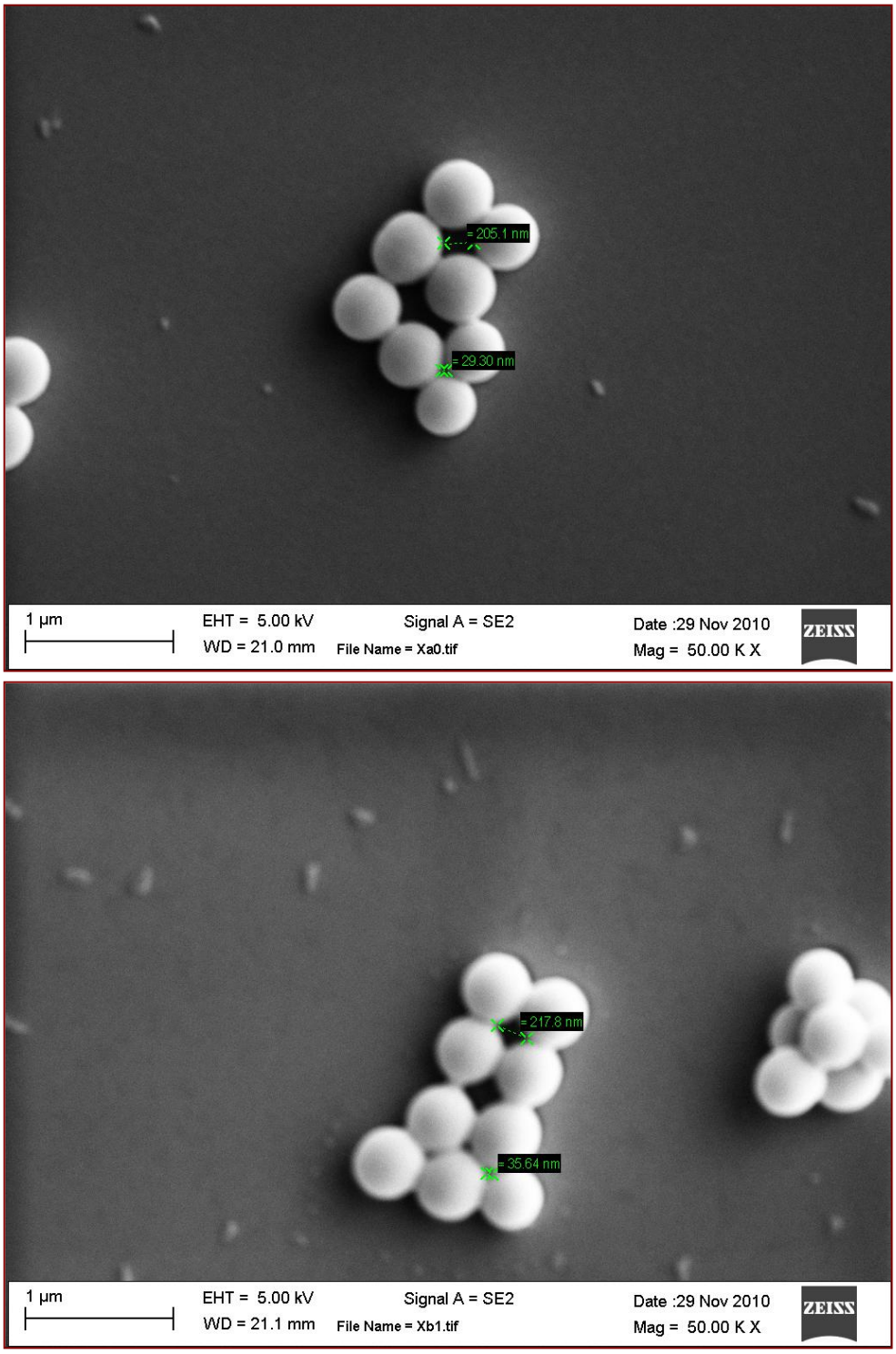

Figure 5.15: SEM image (SE detector) of silica-titania sub-monolayers prepared with 0.0625mL TTIP.

5.4.4 Image analysis of silica-titania sub-monolayers using ImageJ

The SEM images obtained for different precursor concentrations were analyzed using image analysis software. ImageJ is a public domain Java image processing program. It can be used to display, edit, analyze, process, save and print 8-bit, 16-bit and 32-bit images. It can read many image formats including TIFF, GIF, JPEG, BMP, DICOM, FITS and "raw". It supports “stacks", a series of images that share a single window. It is multithreaded, so time-consuming operations such as image file reading can be performed in parallel with other operations.

It can calculate area and pixel value statistics of user-defined selections. It can measure distances and angles. It can create density histograms and line profile plots. It supports standard image processing functions such as contrast manipulation, sharpening, smoothing, edge detection and median filtering.

It does geometric transformations such as scaling, rotation and flips. Image can be zoomed up to 32:1 and down to 1:32. All analysis and processing functions are available at any magnification factor. The program supports any number of windows (images) simultaneously, limited only by available memory.

Spatial calibration is available to provide real world dimensional measurements in units such as millimeters. Density or gray scale calibration is also available in ImageJ [90].

Figure 5.16 shows a snapshot of the ImageJ window with the option to adjust the image threshold selected (thresholding is used to automatically or interactively set lower and upper threshold values, segmenting grayscale images into features of interest and background).

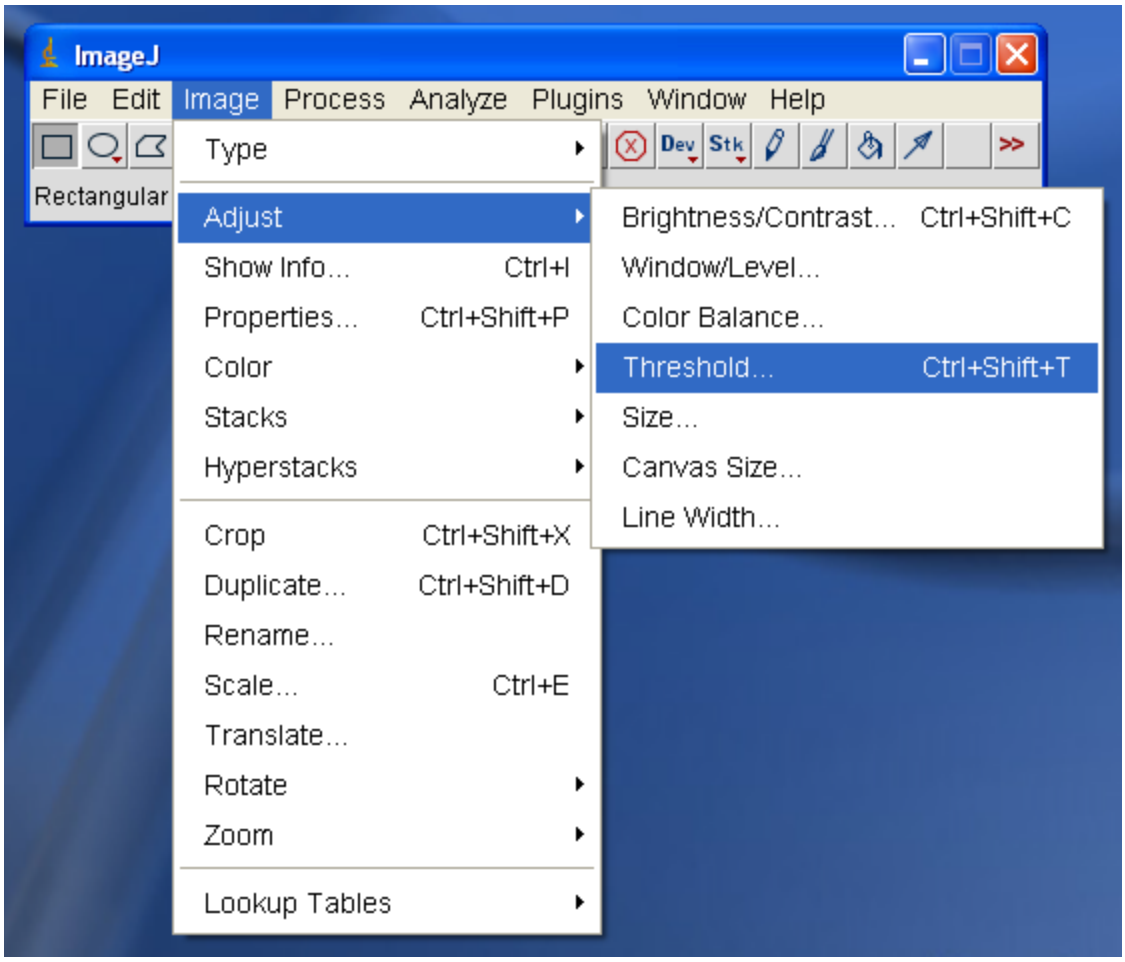

Figure 5.16: Snapshot of ImageJ window with Image/Adjust/Threshold option selected.

5.4.4.1 Measuring distances in ImageJ

ImageJ was used in this study primarily to measure distances in images (namely the neck diameter and 2-particle length of 2-particle silica chains). The three steps followed in ImageJ to calculate distances are listed here. Detailed instructions for other menu options in Image J are provided in Appendix B. To measure lengths in the image:

1. Improve brightness/contrast of image if needed by selecting Image/Adjust/Brightness/Contrast in the menubar.
2. To set the scale on the image, draw a straight line in the image just above the scale bar of the image. Select Analyze/Set Scale. In the Set Scale menu, enter known distance and unit of length. (refer Figure 5.17). The image now has the desired scale information.
3. To measure distance, draw a line using the line tool for the point to point distance that needs to be measured. In the menu bar select Analyze/Measure. The length is displayed in the Results tab (refer Figure 5.18)

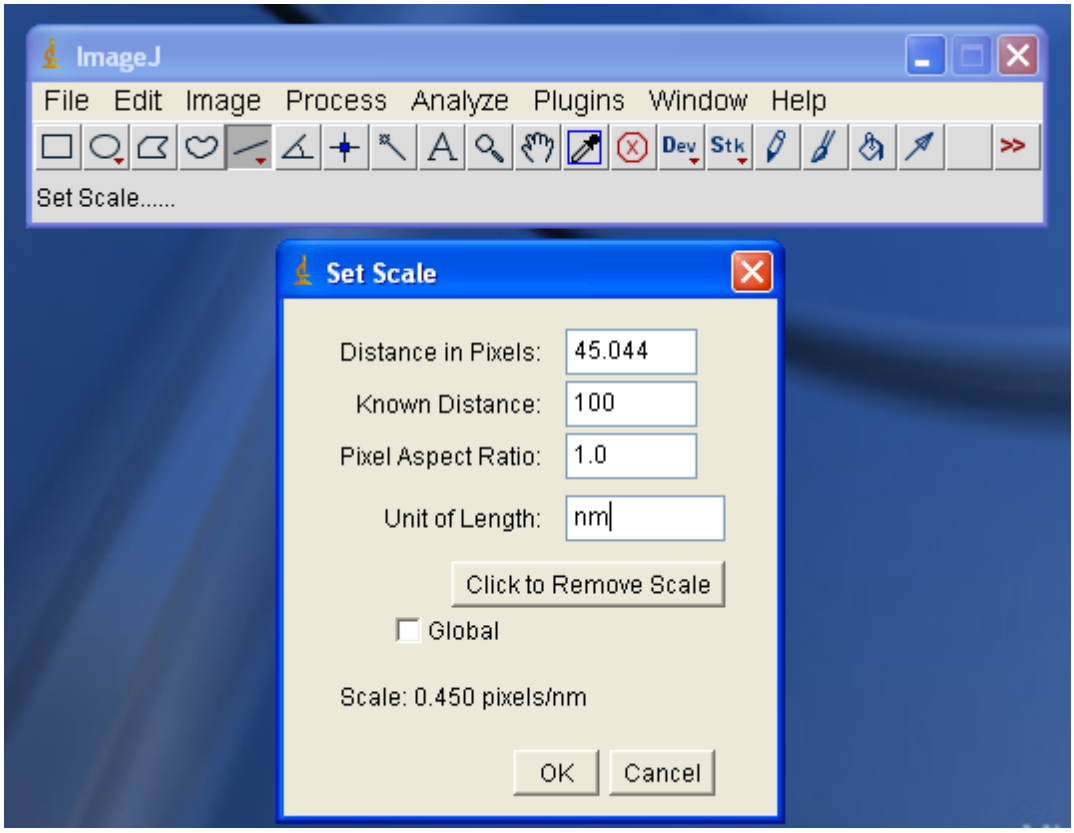

Figure 5.17: Snapshot of ImageJ with "Set Scale" function selected.

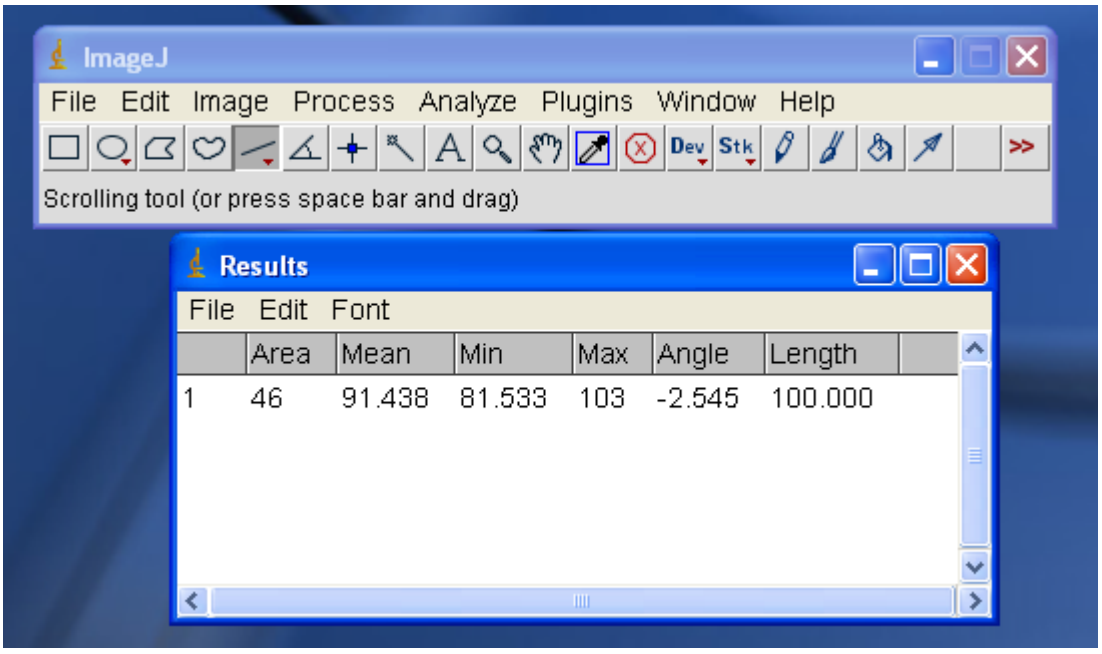

Figure 5.18: Snapshot of ImageJ with "Results" window selected.

5.4.4.2 Measurement of neck width and 2-particle length

The neck width and the 2-particle length of pairs of silica-titania structures was measured using ImageJ according to the procedure described in section 5.4.4.1. Figures 5.19 and 5.20 are illustrations of a 2-particle chain with arrows showing distances measured for neck width and 2-particle length.

For each titania precursor concentration studied, four particle pairs were measured and the average neck width and 2-particle length for these 4 particle pairs was calculated. The results of image analysis are tabulated in Table 5.1 and shown graphically in Figure 5.21. The error bars in Figure 5.21 represent the measurement error in ImageJ. The measurement error in ImageJ for each of the 4 measurements (and hence the average measurement) is ±20 nm. This error is reduced when we use high magnification images; but we were able to see fewer 2-particle chains at higher magnifications. Therefore to get average measurements of four 2-particle pairs, the 20KX SEM images as shown in Figure 5.9 were used for the ImageJ length measurements shown in Table 5.1 and Figure 5.21. From the data in Table 5.1, it can be seen that the neck width decreases by 43% and the 2-particle length decreases by 15% as we reduce the titania precursor amount in the solution from 0.75 to 0.0156mL. This means that by decreasing the titania precursor amount by a factor of almost 98% the neck width has decreased by only 43% - indicating preferential collection of titania at the neck regions. It also shows that in the context of interparticle connections in a DSSC, very low amounts of titania precursor can provide significant particle-to-particle contact material at the neck regions.

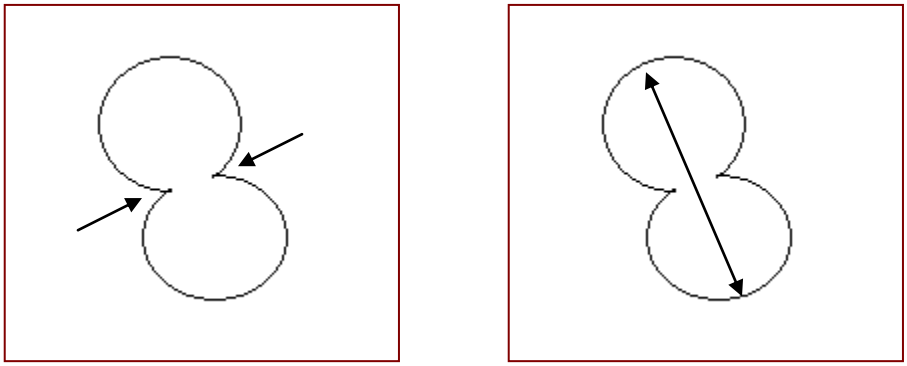

Figure 5.19: Illustration of a 2-particle chain with arrows showing distances measured (neck width and 2-particle length).

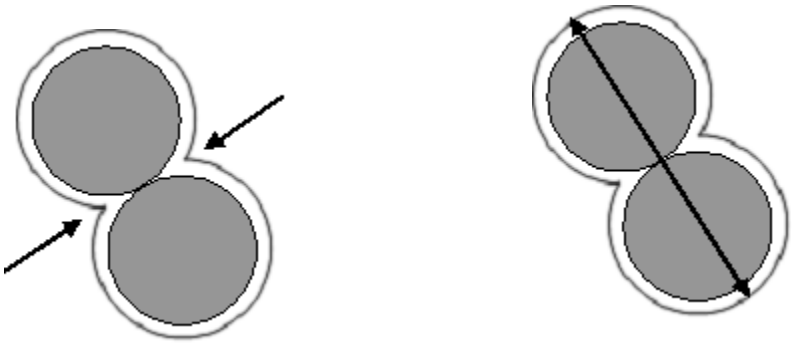

Figure 5.20: Illustration of 2-particle chain with silica particles shown (gray coloration) and with arrows showing distances measured (neck width and 2-particle length).

Table 5.1: Neck width and 2-particle length averaged for four 2-particle pairs.

TTIP amount in sol (mL)	TTIP molar concentration (M)	Neck width (nm)	2-particle length (nm)
0.75	0.2329	304	914
0.375	0.1207	222	824
0.25	0.0813	243	847
0.125	0.0412	213	821
0.0625	0.0207	227	818
0.0312	0.0104	231	795
0.0156	0.0052	173	780

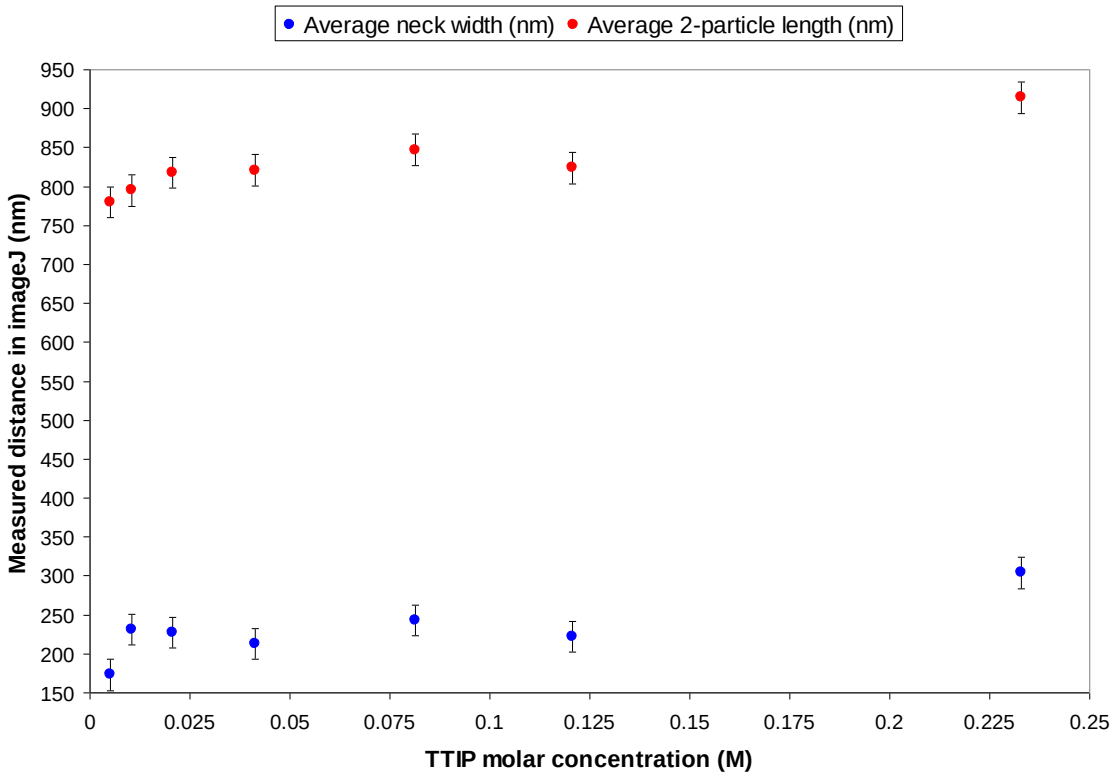

Figure 5.21: Average neck width and average 2-particle length for varying TTIP concentration.

5.4.5 Surface topography of silica-titania sub-monolayers

The surfaces of the silica-titania sub-monolayers were scanned with an atomic force microscope to obtain topography images and calculate neck depths. The AFM image along with the corresponding surface plot of a silica-titania sub-monolayer prepared with 0.0625mL TTIP is shown in Figure 5.22. The formation of silica particle chains is clearly seen from these images. The AFM images were analyzed with a sectioning tool to obtain depth information. The depth of the neck from the surface of the silica was obtained for the sample prepared with 0.0625mL TTIP and is shown in Figure 5.23. It was observed that for the three TTIP amounts tested (0.25mL, 0.0625mL and 0.0156mL), the depth of the neck from the silica surface was in the range of 80-110 nm.

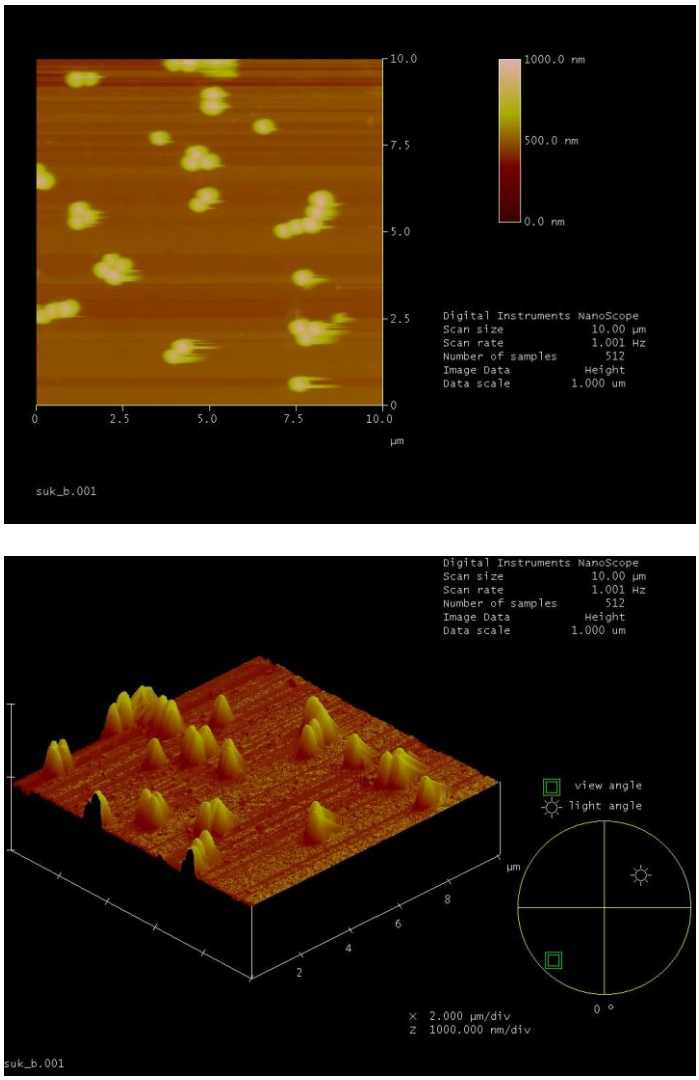

Figure 5.22: AFM images of a silica-titania sub-monolayer.

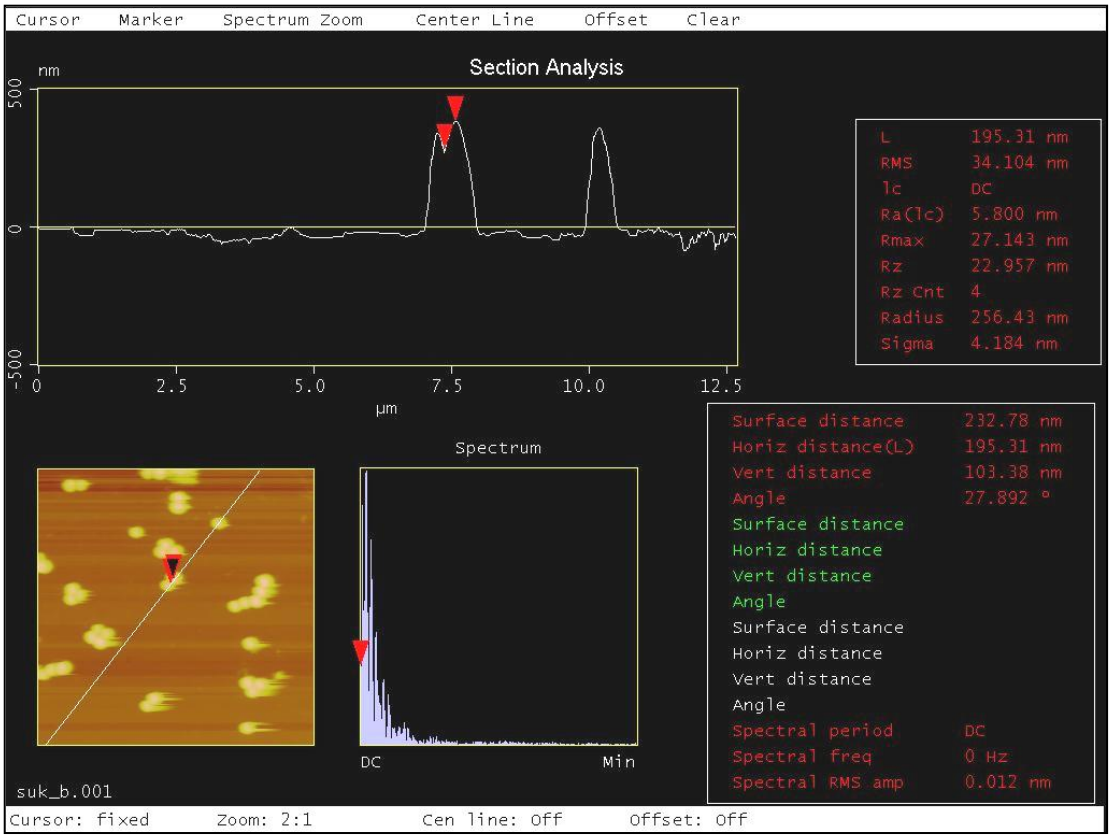

Figure 5.23: Section analysis of the AFM image of Figure 5.22 used to obtain depth information.

5.4.6 High resolution transmission electron microscopy of silica-titania sub-monolayers (Estimation of Surface coverage of silica)

The 2-particle lengths calculated in ImageJ (Table 5.1) can be used to estimate surface coverage of silica particles provided the particle size distribution of the silica is extremely narrow. Referring to figure 5.20, we can see that subtracting the silica particle sizes from the 2-particle length measurement should give us twice the titania thickness, provided the particles are monosized. But this is not the case for the commercial silica

powder used in our experiments. Although the silica particle size reported by the vendor is 500 nm we have observed in the SEM that many of the silica particles are actually closer in diameter to 400 nm (refer Figure 5.24). The sample shown in Figure 5.24 is a pure silica layer prepared by the procedure described in section 5.2.1 except that there was no titania precursor in the solution that was spin coated. The silica particle diameter was measured by using the CARL ZEISS SmarTiff annotation editor (V 1.0.1.2). The particle diameter of 4 silica particles selected at random shows the variability in particle size (from 390 nm to 450 nm). Due to this variability it was not possible to get an estimate of the surface coverage of titania by measuring the average 2-particle length of the particle pairs. A suitable silica particle with uniform particle sizes was not found to be commercially available. This combined with the lack of compositional contrast between silica and titania meant that the surface coverage of silica by the titania could not be determined by image analysis.

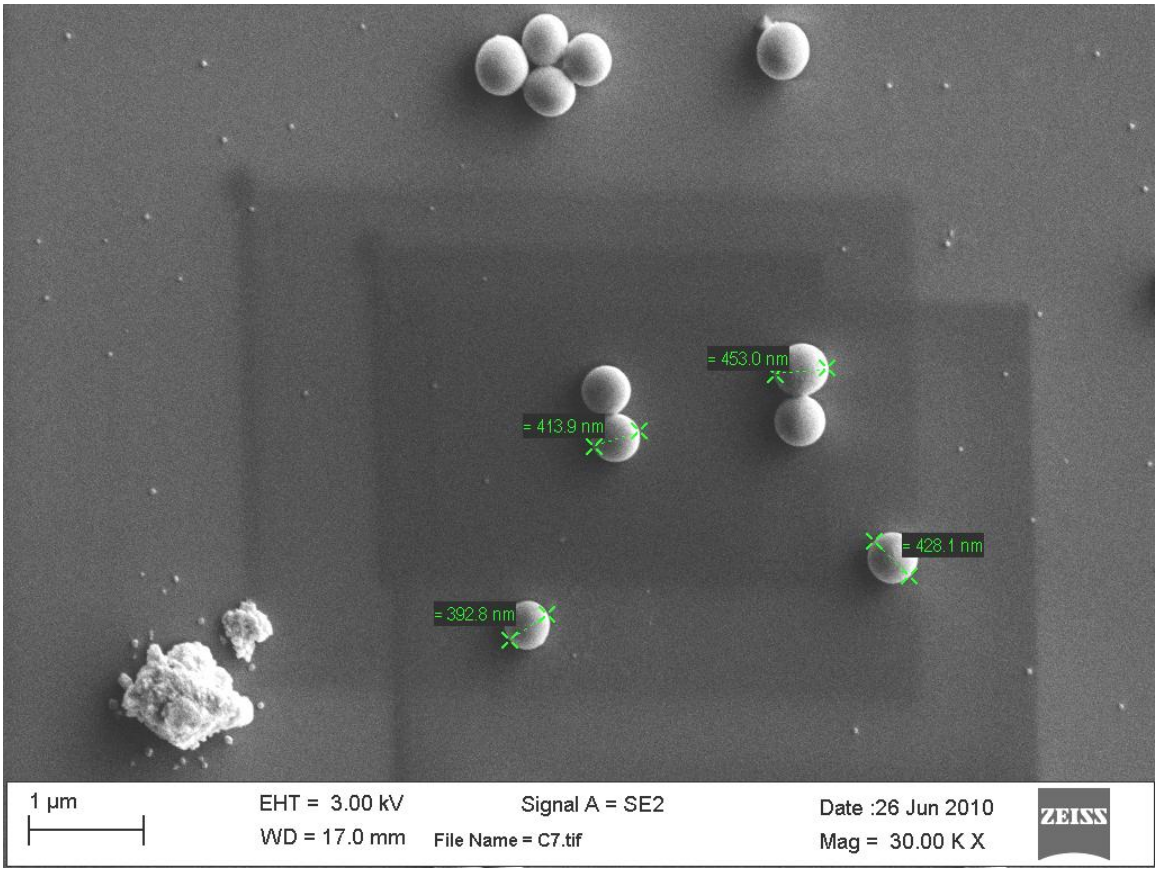

Figure 5.24: SEM image of pure silica layer showing silica particle sizes.

We have therefore used TEM (transmission electron microscopy) to determine surface coverage. The TEM samples were prepared from the spin coated glass samples by dispersing the spin-coated material in methyl alcohol and releasing a few drops of the liquid on an amorphous, 'lacey' carbon film supported on copper grid. Then, the mixture was allowed to dry leaving behind particles dispersed on the TEM grid. HRTEM images obtained thus are shown in Figure 5.25. This image was obtained for a silica-titania sub-monolayer that was prepared with 0.25mL TTIP. The image on the left shows a group of silica particles with titania formation also seen. The image on the right can be used to obtain thickness information and it shows that the titania on the surface of silica is around

5-7nm thick for this particular sample. This demonstrates that we can obtain extremely thin titania coatings on silica surfaces by the spin coating process adopted in our research.

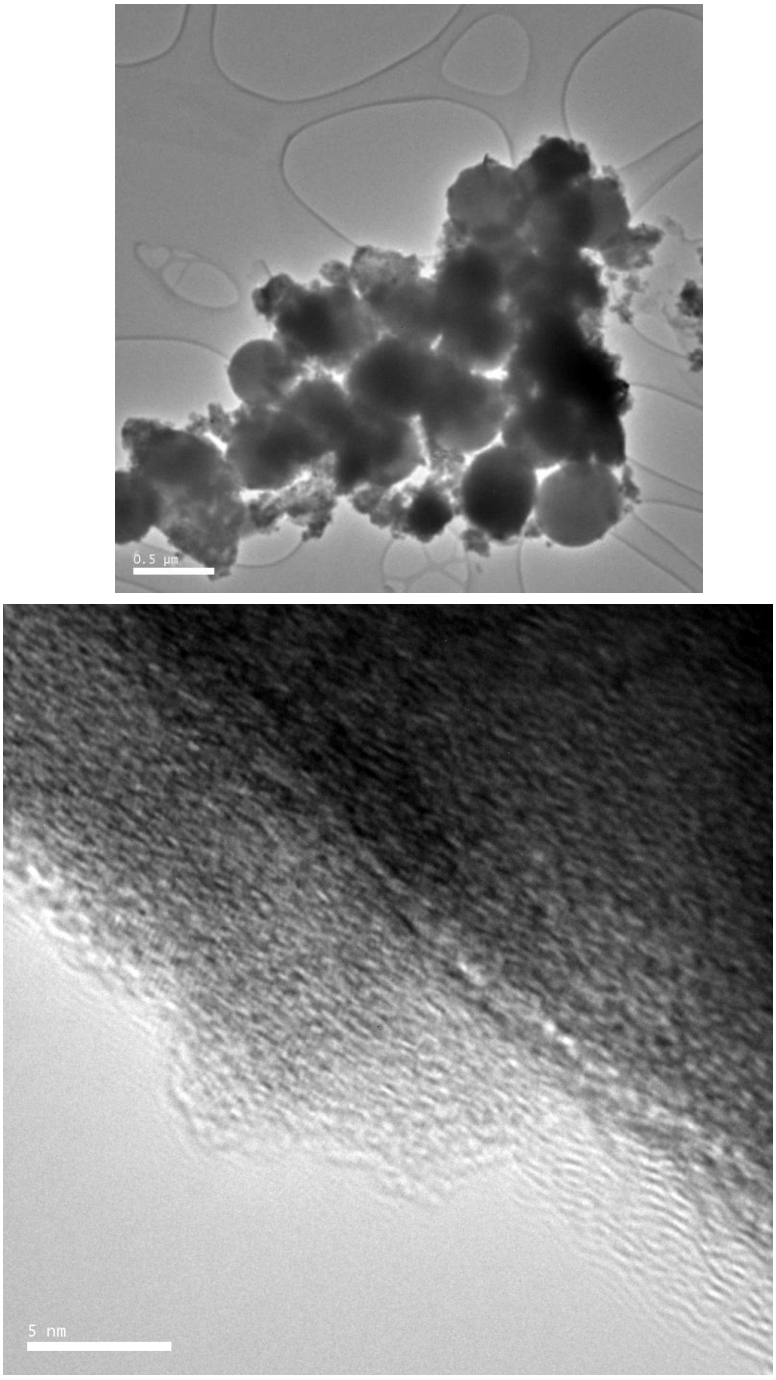

Figure 5.25: HRTEM images of a silica-titania sub-monolayer. (Courtesy: Dr. Jafar Al-Sharab, Department of Materials Science and Engineering, Rutgers, The State University of New Jersey).

5.4.7 Theory of interparticle neck formation

The SEM images of Figures 5.9, 5.10, 5.13 and 5.14 demonstrate that we have good wetting of the silica particle by the titania sol which means that the contact angles are very low. If this were not the case, we would most likely see aggregates of titania particles and individual silica particles on the surface of the glass substrate. The titania sol also seems to wet the substrate well and form a thin coating on the substrate as evidenced in the in-lens images of Figures 5.13 and 5.14; although at the highest concentration (TTIP=0.75 mL) the drying effects are pronounced. As we have seen in Section 3.3 and Figure 3.6 good wetting is essential if we need to have silica particles that are well connected to each other and to the substrate.

Based on the shapes of the interparticle necks and the relationship of the neck width with the amount of TTIP, we can hypothesize that the formation of interparticle necks begins with the formation of liquid bridges during spin coating. Further evidence of this can be found in the optical microscope of a spin coated silica-titania sol that was obtained soon after spin coating (Figure 5.26). The formation of a few silica particle chains is seen to emerge even for the lowest TTIP amount (0.0156mL). We believe that this liquid bridge upon further reaction and heat treatment at 500 °C for 30 minutes leads to the formation of the titania necks.

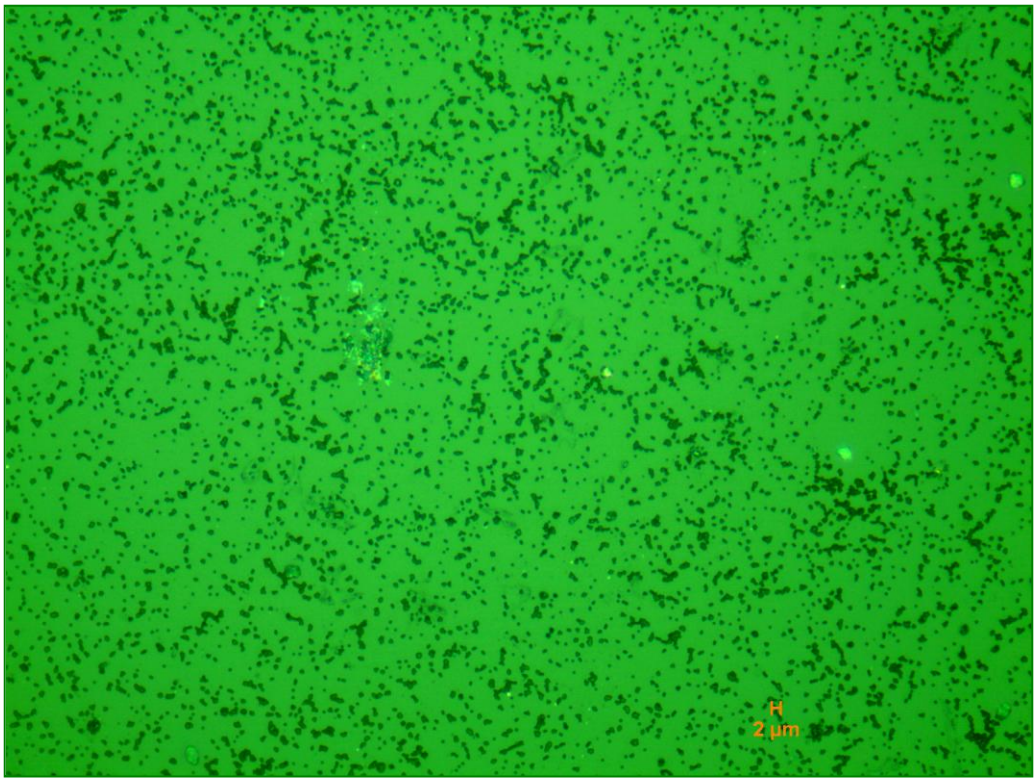

Figure 5.26: Optical microscope image of a spin coated layer of silica particle-titania sol solution (Amount of TTIP = 0.0156mL).

We described in section 5.1.2 how the formation of pendular liquid bridges depends on the wettability of the particles, the geometry of the meniscus and the particle sizes. A lot of research has been published on such liquid bridges; a chronological summary of research investigations on pendular bridges between two particles is provided by Mehrotra et al. [91]. Melrose et al. [92] present the exact geometrical parameters for the pendular ring fluid if the contact angle and the filling angle are known. Table 5.2 (adapted from Ref.[92]) gives the meniscus curvature J and the confined volume V for a contact angle Θ and filling angle ψ. (The contact angle, Θ, is specified as the angle measured through the confined phase, the filling angle, ψ, is the angle between

the axis of cylindrical symmetry and the line of meniscus contact, and *R* denotes the sphere radius).

Table 5.2: Geometrical parameters for pendular ring fluid (adapted from [92]).

ψ, deg	$JR/2$		$10^2V/R^3$	
	Exact	Ref 9	Exact	Ref 9
		$\theta = 0$		
5	126.229	126.125	0.0080	0.01
10	29.983	29.89	0.1121	0.11
15	12.485	12.40	0.5021	0.51
20	6.467	6.395	1.4128	1.44
25	3.729	3.665	3.0897	3.16
30	2.267	2.21	5.7739	5.95
35	1.3995	...	9.699	...
40	0.8460	...	15.091	...
45	0.4729	...	22.177	...
50	0.2108	...	31.193	...
55.64	0.0000	...	43.979	...

Since we have good wetting of the silica particles we can assume a contact angle of 0°. To get an approximation for the filling angle from the SEM images; we can use the angle measurement feature of ImageJ. From these values it is possible to get an estimate for the volume of the pendular bridges for different TTIP precursor concentrations.

5.4.8 Estimation of TTIP concentration needed to create necking

From Table 5.1, the dimensions of the neck obtained by image analysis can be used to back calculate the amount of TTIP needed in a 3-D electrode configuration where we have spherical titania host particles instead of spherical silica particles. This calculation is documented in Appendix C. The calculations in Appendix C show that the

weight ratio of host titania:TTIP that is required for a 65% porous titania electrode with 400nm spherical titania particles is **84**. Referring back to Chapter 2 (section 2.3.3.1) we see that the weight ratio of P25:TTIP that gave the best efficiency (DSSC efficiency=2.09%) is 1/0.25=**4**. This leads us to suggest that the amount of TTIP required to form interconnections would probably be much less if we used spherical titania in the bulk matrix instead of P25.

If we had used 200nm spherical titania particles instead of 400nm, then the volume of each particle would decrease by a factor of 8, and therefore the number of necks increases by a factor of 8. Referring to the calculations in Appendix C we would see that the weight ratio of spherical titania to TTIP would decrease by a factor of 8 when the particle size is halved. The weight ratios and molar ratios for 5 different spherical particle sizes are shown in Table 5.3.

Table 5.3: Weight ratio and molar ratio of Titania /TTIP for 5 spherical titania particle sizes

Particle size of spherical titania host particle (nm)	Weight ratio titania:TTIP	Molar ratio titania:TTIP
400	84	24
200	10.5	3
100	1.3	0.375
50	0.16	0.047
25	0.02	0.006

From Table 5.3 we can see that as the particle sizes of the spherical host titania particle decreases, we need more TTIP to fill in the necks and form the interconnections. If we use smaller host particles with improved surface area, then from Table 5.3 we can get a starting point in terms of concentration of TTIP needed to form an interconnected titania electrode structure. Therefore the 2-D microstructures obtained by spin coating can be very useful in helping us design 3-D electrode microstructures and can provide the kinds of recipes that will lead to well interconnected titania electrodes in dye sensitized solar cells.

5.5 Summary

Silica-titania sub-monolayers were obtained by spin coating a titanium isopropoxide sol containing silica particles onto plain glass substrates. The sub-monolayers were characterized by SEM to observe the morphology and the pore structure of the silica-titania interconnected chains. SEM imaging using the secondary electron detector provides topographical distribution of the silica-titania chains. Imaging with the in-lens detector enables better observation of the drying process in the layer and better observation of the neck formation and chain breakage. It is believed that the formation of liquid bridges between the silica particles during spin coating and further reaction/heat treatment give rise to interparticle necks composed of titania. Image analysis was used to measure the average neck width and 2-particle length in the sub-monolayers for 4 concentrations of the titanium isopropoxide. AFM was used to look at surface topography. Both SEM and AFM show that the morphology of sub-monolayers consists of short chains of silica particles joined at the necks by titania. Image analysis confirms

preferential collection of titania at the necks between the silica particles. TEM analysis pointed to extremely thin titania layers on silica particles.

Chapter 6. Conclusions and Future Work

6.1 Conclusions

Dye sensitized solar cells (or Grätzel cells) were developed by Michael Grätzel and Brian O'Regan in 1991. In contrast to the all-solid conventional semiconductor solar cells, the dye-sensitized solar cell is a photoelectrochemical cell i.e. it uses a liquid electrolyte or other ion-conducting phase as a charge transport medium. Unlike a silicon solar cell, the task of light absorption and charge carrier transport are separated in a DSSC. Light is absorbed by a sensitizer, which is anchored to the surface of a wide band-gap semiconductor, such as titanium dioxide. Charge separation takes place at the interface via photo-induced electron injection from the dye into the conduction band of the semiconductor. Carriers are transported in the conduction band of the semiconductor to the charge collector.

DSSCs are extremely promising because they require low cost materials and can be fabricated with cost effective approaches onto glass or flexible substrates. However a lot of challenges in commercialization of this technology remain. These include:

- Exploring new dye photo-sensitizers with optimum HOMO/LUMO and broader absorption spectrum to increase efficiency.
- Exploring new room temperature ionic liquids to replace electrolytes containing volatile solvents, to improve stability of the cell.
- Developing low temperature approaches to manufacture titania electrodes onto flexible substrates – This research work has been focused on the development of low temperature sintering methods for titania electrodes to improve the stability

and efficiency of flexible DSSCs, and at understanding the microstructure evolution processes that apply for reactive sintering processes in general.

Initially the low temperature approach pursued in this study consisted of using a nanoparticle titania (Degussa P25) and a titanium alkoxide precursor. The hydrothermal treatment of the titania precursor (under neutral pH) converted it to titania through a sol-gel condensation process and this titania formed interconnections between the P25 particles. This low temperature sintering process has led to better performance in dye sensitized solar cells. The efficiency of DSSCs was highest when the weight ratio of P25:TTIP was 1:0.25. The increase in efficiency is attributed mainly to the increase in I_{sc} which shows that the electron transport has improved by addition of TTIP. Beyond a wt% of 50% however the efficiency dropped: probably due to high amounts of incompletely converted titania from the TTIP. This observation is supported by electrochemical impedance spectroscopy studies which show reduced impedance and improved electron lifetime in the titania layer for an addition of 25% wt% TTIP to P25.

In order to further study the process by which the titania precursor led to the formation of titania interconnections, it was necessary to replace the P25:TTIP system, since it did not allow for good titania signal contrast in I-V response, SEM or XRD. Therefore we used amorphous silica as a nominally inert host particle matrix – within which the titania can react and its effects be measured: to help understand how and where the reacting titania is formed. When spherical 500 nm silica particles were used and a post heat treatment process added to the hydrothermal processing steps, anatase titania particles are formed in silica-titania coatings and these show photoactivity in solar cells and moderate new surface area creation. The efficiency of the silica-titania based DSSCs

are very low (<1%) but it can be improved by increasing the amount of titania (varying the silica-titania ratio).

Silica particles of three different morphologies were tested to determine the influence of host silica framework morphology on the efficiency of DSSCs. The efficiency is shown to be higher when larger non-porous silica particles are used and thin nanocrystalline titania is coated on this superstructure. This observation is supported by the BET data which showed marked improvement in specific surface area in the silica-titania powders for the 500 nm silica particles. If the host silica particles are themselves highly porous (as seen in the 20 nm and 80 nm silica particle cases) surface tension effects during coating and precursor reaction seem to draw the material into the necks and tiny pore regions; and not enough reactive material is left to build good conduction pathways on the surface.

To probe deeper into the silica-titania framework and look closely at the neck regions, we have spin coated thin sub-monolayers of silica-titania onto glass substrates and used SEM, AFM and TEM characterization techniques to probe the sub-monolayers. During the spin coating process, surface tension pulls nearby hard-sphere silica particles into direct contact. Liquid bridges are formed leading to necks after reaction and heat treatment. This novel approach of forming sub-monolayers enabled us to directly measure the titania neck formation between pairs of silica particles and the pore sizes in silica particle clusters by image analysis. The neck width decreases by 43% and the 2-particle length decreases by 15% as we reduce the titania precursor amount in the solution from 0.75 to 0.0156 mL. This means that by decreasing the titania precursor amount by a factor of almost 98% the neck width has decreased by only 43% - indicating

preferential collection of titania at the neck regions. It also shows that in the context of interparticle connections in a DSSC, very low amounts of titania precursor can provide relatively good particle-to-particle contact material at the neck regions.

Towards low temperature sintering methods for dye sensitized solar cells, the results obtained in this research enable us to propose an electrode configuration in which spherical titania particles are used instead of the P25 nanoparticles and are joined at interparticle necks by the hydrolysis/condensation of a titanium alkoxide precursor. We have shown that very little amounts of titanium alkoxide precursor are enough to create interparticle contacts and used the 2-D microstructure data to extract quantitative information to design 3-D microstructures.

The unique approach we have followed in obtaining silica-titania submonolayers to probe interparticle interconnections can be applied to a wide variety of mixed oxide and core-shell type of materials. The liquid phase locations in these microstructures are very closely related to other liquid phase arrangements found in composites, either by reactive sintering or liquid phase sintering: there are similar surface tension effects driving microstructural changes; and, similar shrinkage and contact morphologies matter for many systems.

Also, the observational tools and the model system approach we have developed could be applied to many systems that are also of interest for numerous optical and mechanical applications.

6.2 Future work

The focus of this research work has been on understanding the reactive sintering process with respect to its application to dye sensitized solar cells. While much progress was made in probing the process of formation of interparticle necks, there is a lot of scope for applying the insights gained in this research to further testing. In particular there is a need to test an electrode configuration consisting of spherical titania particles covered in a thin hydrothermally formed titania superstructure in dye sensitized solar cells. A majority of cells tested in this research were made on glass substrates but there is a need to expand testing to flexible substrates such as PET (polyethylene terephthalate). Both efficiency and mechanical stability of cells prepared using a low temperature sintering method on flexible substrates needs to be determined.

Surface area and pore size distribution:

Surface area and pore size distribution of the low temperature sintered powders prepared using P25 and titanium isopropoxide needs to be known to determine the change in the pore structure of P25 due to the hydrothermal treatment. The surface area of commercial P25 powder is approximately 50.0 m^2/g. The surface area of the P25+TTIP powders prepared by steam treatment will depend on whether the titania formed during the process coats the P25 particles in addition to forming interconnections. An increase in surface area could be beneficial for increasing the short circuit current (and efficiency) because it will lead to an increase in the amount of adsorbed dye. On the other hand, if the TTIP forms amorphous titania which coat the crystalline P25 particles, it might lead to a decrease in cell efficiency.

Another important property that can be studied is the pore size distribution. It will be interesting to see how the titania formed at the interconnections changes the micropore/mesopore configuration of the P25/titania coating. Song et al. [93] studied the hydrolysis of TTIP at different water concentrations and found that the titania powders dried at 150 °C and for all molar ratios of H_2O/TTIP used (5, 20, 200 and 1000) showed bimodal pore size distributions; consisting of intra-aggregated pores with maximum pore diameters from micropores to 3.3 nm and interaggregated pores with maximum pore diameters of ca. 60 nm. They compare the pore-size distribution of one of powders (the R20 powder prepared with molar ratio H_2O/TTIP=20) calcined at 500 °C to the Degussa P25 powder. Both the powders had comparable surface areas (~50-60 m^2/g). The pore-size distributions they report suggest that the P25-titania powders made by steam treatment should possess micropores in addition to the mesopores from the P25. This will be an interesting result because it will show that in addition to the formation of interconnections, the porosity changes due to the addition of TTIP would play an important role in enhancing the efficiency of DSSCs.

Nanoindentation:

The microstructural properties of the titania films will depend on the processing conditions and the nature of interparticle connections. Nanoindentation is a technique that can estimate mechanical properties of thin films such as hardness and elastic modulus. Indentation techniques have been applied to study steam treated titania coatings on NiTi surfaces [94] and sol-gel titania coatings on glass and copper substrates [95].

As a future progression of the work that we have done on silica-titania sub-monolayers, nanoindentation can be used to study mechanical properties of silica-titania and P25 based titania films for different processing temperatures and titania precursor concentrations.

Applications of silica-titania materials:

Titania-silica materials have been extensively used as photocatalysts [96,97] , as protective coating on stainless steel to resist oxidation and chemical attack [98], antireflection coatings for optical glasses [99], and as very interesting glass materials with ultralow thermal expansion coefficients [100,101] and high refraction indices [102]. Such advanced titania-silica materials not only take advantage of both TiO_2 (an n-type semiconductor and an active catalytic support) and SiO_2 (high thermal stability and excellent mechanical strength), but also extends their applications through the generation of new catalytic active sites due to the interaction of TiO_2 with SiO_2.

The silica-titania materials that have been obtained in this study show modest efficiencies in dye sensitized solar cells. But their potential for applications in the aforementioned areas needs to be explored. Heterogeneous photocatalysis has shown a high efficiency in the removal of highly toxic and non-biodegradable pollutants commonly present in air and in domestic or industrial wastewaters and silica-titania based materials have shown a lot of promise in this field [103,104]. Therefore, there is a lot of scope for future work on using the silica-titania materials we have developed as promising cost efficient photocatalysts with applications in water purification.

APPENDIX A

List of Abbreviations

DSSC	Dye sensitized solar cell
TCO	Transparent conducting oxide
FTO	Fluorine doped tin oxide
ITO	Indium tin oxide
Voc	Open circuit voltage
Isc	Short circuit current
FF	Fill factor
TTIP	Titanium tetra isopropoxide
EIS	Electrochemical impedance spectroscopy
PET	Polyethylene terephthalate
PEN	Polyethylene naphthalate
MLCT	Metal to Ligand Charge Transfer
AFM	Atomic force microscopy
BET	Brunauer-Emmett-Teller
SEM	Scanning electron microscopy
HRTEM	High Resolution Transmission electron microscopy
XRD	X-ray diffraction
RH	Relative Humidity

APPENDIX B

ImageJ Instructions

(Adapted from :http://rsbweb.nih.gov/ij/docs/pdfs/ImageJ.pdf)

Courtesy: Larry Reinking

Department of Biology, Millersville University

Millersville, PA 17551

larry.reinking@millersville.edu

ImageJ Basics

(Version 1.38)

ImageJ is a powerful image analysis program that was created at the National Institutes of Health. It is in the public domain, runs on a variety of operating systems and is updated frequently. You may download this program from the source (http://rsb.info.nih.gov/ij/) or copy the ImageJ folder from the C drive of your lab computer. The ImageJ website has instructions for use of the program and links to useful resources.

Installing ImageJ on your PC (Windows operating system)

Copy the ImageJ folder and transfer it to the C drive of your personal computer. Open the ImageJ folder in the C drive and copy the shortcut (microscope with arrow) to your computer's desktop. Double click on this desktop shortcut to run ImageJ. See the ImageJ website for Macintosh instructions.

ImageJ Window:

The ImageJ window will appear on the desktop; do not enlarge this window. Note that this window has a Menu Bar, a Tool Bar and a Status Bar.

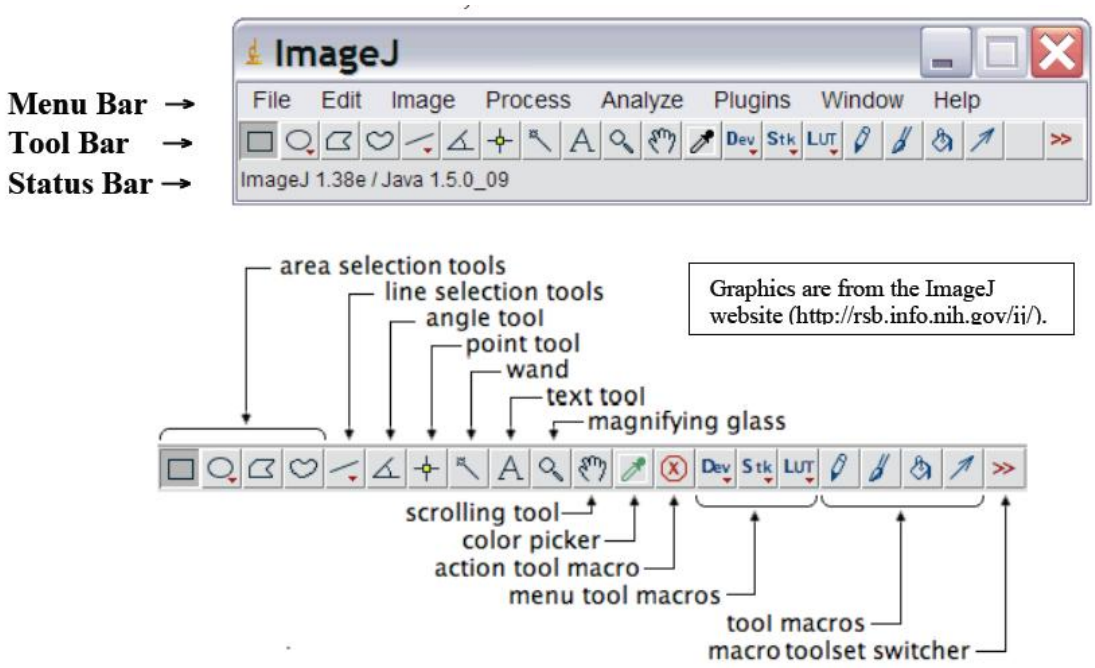

Adjusting Memory Allocation: Use the ***Edit*** → ***Options*** → ***Memory*** command to adjust the default memory allocation. Setting the maximum memory value to more than about 75% of real RAM may result in poor performance due to virtual memory "thrashing".

Opening an Image File: Select ***File*** → ***Open*** from the menu bar to open a stored image file.

Tool Bar: The various buttons on the tool bar allow you measure, draw, label, fill, etc. A right-click or a double left-click may expand your options with some of the tool buttons.

Area Selection Tools: The first four buttons on the tool bar allow you to surround an area on the image with a rectangle, oval, polygon or freehand shape. After selection, these areas may be altered, analyzed, copied, etc. using the menu commands. Note that the status bar, below the tool bar, gives information such as the coordinates (xx, yy) of the selection on the frame.

Line Selection Tools: This button allows you to create straight, segmented or freehand lines (right-click to select line type). Information about the line is displayed on the status bar. Double-click on the button to alter the line width, select A***nalyse*** → ***Measure*** (or Ctrl+M) to record a line length and ***Edit*** → ***Draw*** (or Ctrl+D) to make a line permanent.

Angle Tool: Draws two intersecting lines and measures the formed angle.

Point Tool: When 'Auto-Measure' is selected, this tool allows you to mark locations on an image; with each click the coordinates of the mark (xx, yy) and brightness values (0-255) are recorded in a data window. Color images will have three brightness readings displayed on the status bar, one each for the red, green and blue channels, however only a single grayscale brightness value will appear in the data window.

Wand Tool: This tool automatically finds the edge of an object and traces its shape. It works best with high contrast images (see Thresholding, next page). Place the wand to the left of an edge; click and the algorithm will search to the right for an edge. It will then trace along the edge of the object until it returns to the starting point.

Text Tool: Double click on this button to select a font and size. A large font size will probably be required for an image from a high resolution digital camera. Single click the button, click-drag a text box and type the label. Move the box to the desired location and permanently set the text in place with ***Edit*** → ***Draw*** (or Ctrl+D)**.** Use the color picker tool to select font color.

Magnifying Glass: Left-click on the image to magnify; right-click to reduce the image size.

Scrolling Tool: This button allows you to move an image if it is larger than the window. Pressing the keyboard space bar is a shortcut that temporarily activates this tool.

Color Picker: This tool sets the foreground drawing/text color when a color on an image is 'picked up' with the eyedropper. Colors also may be selected from the *Colors* window by double-clicking the color picker button (or via ***Image → Color → Color Picker***). Use Alt+click to change the background color. The icon for this tool (eye dropper) shows the current foreground color while the frame around it shows the background color.

Other Tools: The remaining tool buttons are similar to those found in drawing programs (spray can, flood fill, etc.) and can be easily used after a bit of experimentation.

Image Editing and Analysis

The following is a small sampling of processing techniques that are possible with ImageJ. ImageJ can be used in conjunction with a photo editing program such as Adobe Photoshop. During analysis, measured values can be easily transferred to a spreadsheet with a 'cut and paste'. It is a very good idea to make a backup copy of your image before doing any processing. Refer to the ImageJ and NIH Image websites for more information

Undo. ***Edit → Undo*** reverses the preceding action. Only one back-step is possible.

Revert. ***File → Revert*** converts all changes back to the original saved version.

Cropping. Surround the area with the rectangular selection tool followed by ***Image → Crop***.

Clear Outside. Make a perimeter with an area selection tool followed by ***Edit → Clear Outside*****.** This technique is useful for clearing extraneous objects near an area of interest. ***Edit → Clear*** clears inside of the perimeter.

Enhancing Brightness and Contrast. ***Image → Adjust → Brightness/Contrast***; click 'Auto' or set manually with the sliders. Also try **Process → *Enhance Contrast***.

Removing Noise**. *Process* → *Noise* → *Despeckle*** or try ***Process* → *Filters* → *Median***

Rotating an Image. ***Image* → *Rotate*** and select type of rotation

Converting to Grayscale. ***Image* → *Type* → *8-bit*** converts the image to 256 shades (8-bit) of gray. In this scale 0 = pure black and 255 = pure white…. a grayscale reading of 128 would be a medium gray.

Thresholding (Binary Contrast Enhancement). This is commonly used when detecting edges, counting particles or measuring areas. A grayscale image is converted to binary (a.k.a. halftone or black & white) by defining a grayscale cutoff point. Grayscale values below the cutoff become black and those above become white. The procedure: First convert the image to 8-bit grayscale as described above (***Image* → *Type* → *8-bit***). Create a 'thresholded' binary image by selecting ***Process* → *Binary* → *Make Binary***. A less automated procedure involves:

Image* → *Adjust* → *Threshold; use the slider to adjust the threshold. The red areas will become the black portions in the binary image. Click 'Apply' to complete the conversion. 'Brightness slicing' is a similar procedure that uses both upper and lower threshold values.

Measuring and Counting Objects

Setting Measurement Scale. Draw a line between two points of known distance such as a ruler on the photograph. Go to ***Analyze* → *Set Scale***. In the *Set Scale* window the length of the line, in pixels, will be displayed. Type the known distance and units of measure in the appropriate boxes and click OK. Measurements will now be shown using these settings. If the pixel:length relationship is known from a previous measurement you may

directly type this information in the *Set Scale* window. Check 'global' to apply this scale to other image frames.

Set Measurements. Choose parameters to be measured via ***Analyze → Set Measurements***.

Measuring Distance Between Points. Draw a line between two points. The status bar will show the angle (from horizontal) and the length. ***Analyze → Measure*** (or Ctrl+M or simply type M on the keyboard) transfers the values to a data window.

Measuring Area. Surround an area with a perimeter. This can be done with an area selection tool, the wand (for high contrast images) or with ***Analyze Particles*** (see below). ***Analyze →Measure*** (or keyboard M) transfers the area measurement to a data window.

Counting Particles. As described above, convert the image to 8-bit grayscale and then 'threshold' the image.

Go to ***Analyze → Analyze Particles***, type the upper and lower limits for the particle size, toggle 'show outlines' and check ‘Display Results’. Click OK and each counted particle will be outlined and numbered in a new widow (numbers may be very small).

The data window contains measurements for each particle.

Saving Files. Images from digital cameras are usually saved as JPEG files. JPEG is a type of memory compression that results in the loss of some data. A JPEG image degrades each time it is opened, edited and resaved. It is best to save a file in a 'lossless' format such as a TIFF during the editing process (***File → Save As → Tiff***).

Printing. Should you encounter printing problems, save the processed image and print with a photo editor. Saved images also may be inserted into MS Word for printing.

APPENDIX C

Calculation of molar ratio of TTIP needed for interconnections in 10 micron thick titania electrode in a DSSC:

Consider the smallest neck (neck width=173nm) that was obtained in our experiments for a TTIP concentration = 0.015625mL in solution or moles/liter TTIP = 0.0052

Calculation of number of interparticle necks:

Consider a solar cell (cell area exposed to light = 0.25 cm^2) tested in the solar simulator:

Volume of the solar cell = 0.25cm^2 * 10 micron = 2.5* 10^{-10} m^3 = **Vcell**

Assume the average diameter of a silica particle is 400nm.

Volume of 1 silica particle = $(4/3)*\pi*R^3$ = 3.351 * 10^{-20} m^3

Consider a porosity of ~65% (optimum porosity for a titania electrode in a DSSC is around 60-70%)

Volume of silica for a porosity of 65% = 0.35*Vcell =8.75 *10^{-11} m^3 = **Vsilica**

Number of silica particle in a cell with 65% porosity

= Vsilica/ volume of one silica particle

= 2.611 * 10^9 = N

Average coordination number for a film with a porosity of 65% is between 3.5 and 4[105]. For the sake of simplicity we have considered a coordination number of 4.

This means that each silica particle has 4 nearest neighbors and therefore 4 interparticle necks which means the number of necks per silica particle is 2N

Therefore number of interparticle necks in the solar cell electrode **~ $5.222 * 10^{9}$**

Calculation of the volume of titania in the necks:

For a neck width of 173nm and neck height of 30nm (obtained from image analysis) we can approximate the neck to a cylinder and obtain its volume

Volume of a neck = $\pi*R^2*h= \pi*(86.5)^2*30= 7.0519*10^{-22}$ m^3 = **Vneck**

Total volume of titania necks in the solar cell = Vneck*2N ~ **$3.6825*10^{-12}$ m^3**

Calculation of TTIP molar concentration:

Number of moles of titania in a volume of **$3.6825*10^{-12}$ m^3** can be calculated using its density (3.9g/cc) and its molecular weight (79.90). This gives

Number of moles of titania present in the interparticle necks= $3.6825*3.9*79.9*10^{-6}$

= 0.001155 moles

Since 1 mole of TTIP is needed per mole of titania we get the number of moles of TTIP needed to form interconnections in the solar cell = **0.001155 moles TTIP or**

Weight of TTIP required= **$4.064*10^{-6}$g=W1 (molecular weight of TTIP=284.22)**

If we used spherical 400nm titania particles in place of the 400nm silica particles in the matrix then we can estimate the molar ratio or the weight ratio of 400nm titania/TTIP as follows:

Volume of 400nm titania particles = 8 .75 *10^{-11} m^3 (same as Vsilica)

Weight of 400nm titania = 8 .75 *10^{-5}*3.9 = **3.4125*10^{-4} g =W2**

Weight ratio of 400nm titania:TTIP = W2/W1 = 83.96 ~84

Molar ratio of 400nm titania:TTIP= 84*79.9/284.22 = 23.61

The weight ratio of spherical 400nm titania to TTIP is approximately **84**. Referring back to Chapter 2 (section 2.3.3.1) we see that the weight ratio of P25:TTIP that gave the best efficiency is 1/0.25=**4**. This shows that the amount of TTIP required to form interconnections would probably be much less if we used spherical titania in the bulk matrix instead of P25.

BIBLIOGRAPHY

1. http://www.eia.doe.gov/energyexplained/index.cfm?page=about_home

2. http://www.eere.energy.gov/basics/renewable_energy/pv_cells.html

3. Q. Zhang and G. Cao. Nanostructured photoelectrodes for dye-sensitized solar cells. *Nano Today* 6, 91-109 (2011).

4. M. Raugei and P. Frankl. Life cycle impacts and costs of photovoltaic systems: Current state of the art and future outlooks. *Energy* 34, 392–399 (2009).

5. http://www.gtmresearch.com/report/third-generation-thin-film-solar-technologies

6. B. O'Regan and M. Grätzel. A low-cost, high-efficiency solar cell based on dye-sensitized colloidal TiO_2 films. *Nature* 353, 737-740 (1991).

7. M. Grätzel. Dye-sensitized solar cells. Review. *J. Photochem. Photobiol., C* 4, 145-153 (2003).

8. M. Junghänel. Novel aqueous electrolyte films for hole conduction in dye sensitized solar cells and development of an electron transport model. *Thesis.* Freie Universität Berlin. (2007).

9. J. Halme. Dye-sensitized nanostructured and organic photovoltaic cells: technical review and preliminary tests. *Thesis*. Helsinki University of Technology. (2002).

10. D. Matthews, P. Infelta and M. Grätzel. Calculation of the photocurrent-potential characteristic for regenerative, sensitized semiconductor electrodes. *Sol. Energy Mater. Sol. Cells* 44, 119-155 (1996).

11. F.T. Kong, S.Y. Dai and K.J. Wang. Review of Recent Progress in Dye-Sensitized Solar Cells. *Advances in OptoElectronics* Article ID 75384 (2007).

12. M. Murai, A. Furube, M. Yanagida, K. Hara and R. Katoh. Near-IR transient absorption spectra of N3 dye as a probe of aggregation on nanocrystalline semiconductor films. *Chem. Phys. Lett.* 423, 417–421 (2006).

13. M. Grätzel. Conversion of sunlight to electric power by nanocrystalline dye-sensitized solar cells. *J. Photochem. Photobiol., A* 164, 3–14 (2004).

14. K. Sayamaa, S. Tsukagoshi, T. Mori, K. Hara, Y. Ohga, A. Shinpou, Y. Abe, S. Suga and H. Arakawa. Efficient sensitization of nanocrystalline TiO_2 films with cyanine and merocyanine organic dyes. *Sol. Energy Mater. Sol. Cells* 80, 47–71 (2003).

15. G. Hodes (Editor). Electrochemistry of Nanomaterials. Wiley-VCH. Page 221. 2001.

16. G.K. Mor, O.K. Varghese, M. Paulose, K. Shankar and C.A. Grimes. A review on highly ordered, vertically oriented TiO_2 nanotube arrays: Fabrication, material properties, and solar energy applications. *Sol. Energy Mater. Sol. Cells* 90, 2011–2075 (2006).

17. S. Kitazawa, Y. Choi, S. Yamamoto and T. Yamaki. Rutile and anatase mixed crystal TiO_2 thin films prepared by pulsed laser deposition. *Thin Solid Films* 515, 1901-1904 (2006).

18. N. Yamanaka, R. Kawano, W. Kubo, N. Masaki, T. Kitamura, Y. Wada, M. Watanabe and S. Yanagida. Dye-Sensitized TiO_2 Solar Cells Using Imidazolium-Type Ionic Liquid Crystal Systems as Effective Electrolytes. *J. Phys. Chem. B* 111, 4763-4769 (2007).

19. R. Kawano, H. Matsui, C. Matsuyama, A. Sato, M.A.B.H. Susan, N. Tanabe, M. Watanabe. High performance dye-sensitized solar cells using ionic liquids as their electrolytes. *J. Photochem. Photobiol., A* 164, 87–92 (2004).

20. P. Chen, C. Lee, R. Vittal and K. Ho. A quasi solid-state dye-sensitized solar cell containing binary ionic liquid and polyaniline-loaded carbon black. *J. Power Sources* 195, 3933–3938 (2010).

21. M. Berginc, U.O. Krasovec, M. Jankovec and M. Topic. The effect of temperature on the performance of dye-sensitized solar cells based on a propyl-methyl-imidazolium iodide electrolyte. *Sol. Energy Mater. Sol. Cells* 91, 821–828 (2007).

22. A. Hagfeldt and M. Grätzel. Molecular Photovoltaics. *Acc. Chem. Res.* 33, 269-277 (2000).

23. A. Luque and S. Hegedus (Editors). Handbook of Photovoltaic Science and Engineering. John Wiley & Sons, Ltd. 2003.

24. http://www.g24i.com/pages,manufacturing,77.html

25. http://www.solaronix.com/products/dyesolarcells/

26. http://www.dyesol.com/index.php?page=Dyesol+Designs

27. A. DuPasquier. An approach to laminated flexible Dye sensitized solar cells. *Electrochim. Acta* 52, 7469–7474 (2007).

28. J. Halme, J. Saarinen and P. Lund. Spray deposition and compression of TiO_2 nanoparticle films for dye-sensitized solar cells on plastic substrates. *Sol. Energy Mater. Sol. Cells* 90, 887–899 (2006).

29. G. Boschloo, H. Lindström, E. Magnusson, A. Holmberg and A. Hagfeldt. Optimization of dye-sensitized solar cells prepared by compression method. *J. Photochem. Photobiol., A* 148, 11–15 (2002).

30. S. Uchida, M. Tomiha, H. Takizawa and M. Kawaraya. Flexible dye-sensitized solar cells by 28 GHz microwave irradiation. *J. Photochem. Photobiol., A* 164, 93–96 (2004).

31. C. Longo, J. Freitas, M.A. De Paoli. Performance and stability of TiO_2/dye solar cells assembled with flexible electrodes and a polymer electrolyte. *J. Photochem. Photobiol., A* 159, 33–39 (2003).

32. T.N. Murakami, Y. Kijitori, N. Kawashima and T. Miyasaka. UV Light-assisted Chemical Vapor Deposition of TiO_2 for Efficiency Development at Dye-sensitized Mesoporous Layers on Plastic Film Electrodes. *Chem. Lett.* 32, 1076–1077 (2003).

33. D. Zhang, T. Yoshida and H. Minoura. Low Temperature Synthesis of Porous Nanocrystalline TiO_2 Thick Film for Dye-Sensitized Solar Cells by Hydrothermal Crystallization. *Chem. Lett.* 9, 874–875 (2002).

34. D. Zhang, T. Yoshida and H. Minoura. Low-temperature Fabrication of Efficient Porous Titania Photoelectrodes by Hydrothermal Crystallization at the Solid/Gas Interface. *Adv. Mater.* 15, 814-817 (2003).

35. D. Gutiérrez-Tauste, I. Zumeta, E. Vigil, M.A. Hernández-Fenollosa, X. Domènech and J.A. Ayllón. New low-temperature preparation method of the TiO_2 porous photoelectrode for dye-sensitized solar cells using UV irradiation. *J. Photochem. Photobiol., A* 175, 165–171 (2005).

36. S. Nakade, M. Matsuda, S. Kambe, Y. Saito, T. Kitamura, T. Sakata, Y. Wada, H. Mori and S. Yanagida. Dependence of TiO_2 Nanoparticle Preparation Methods and Annealing Temperature on the Efficiency of Dye-Sensitized Solar Cells. *J. Phys. Chem. B* 106, 10004-10010 (2002).

37. K.J. Kim, K.D. Benkstein, J. Lagemaat and A.J. Frank. Characteristics of Low-Temperature Annealed TiO_2 Films Deposited by Precipitation from Hydrolyzed $TiCl_4$ Solutions. *Chem. Mater.* 14, 1042-1047 (2002).

38. T. Miyasaka, M. Ikegami and Y. Kijitori. Photovoltaic Performance of Plastic Dye-Sensitized Electrodes Prepared by Low-Temperature Binder-Free Coating of Mesoscopic Titania. *J. Electrochem. Soc.* 154, A455-A461 (2007).

39. T. Kasuga, M. Hiramatsu, A. Hoson, T. Sekino and K. Niihara. Titania Nanotubes Prepared by Chemical Processing. *Adv. Mater*. 11, 1307–1311 (1999).

40. J.N. Nian and H. Teng. Hydrothermal Synthesis of Single-Crystalline Anatase TiO_2 Nanorods with Nanotubes as the Precursor. *J. Phys. Chem. B* 110, 4193-4198 (2006).

41. D. Zhang, T. Yoshida, K. Furuta and H. Minoura. Hydrothermal preparation of porous nano-crystalline TiO_2 electrodes for flexible solar cells. *J. Photochem. Photobiol. A* 164, 159–166 (2004).

42. http://www.newport.com/150---300-W-Solar-Simulators/376933/1033/catalog.aspx

43. M.J. Ross and K.R. William. Impedance Spectroscopy: Emphasizing Solid Materials and Systems. *New York: John Wiley & Sons.* 1987.

44. http://www.facstaff.bucknell.edu/mastascu/eControlHTML/Freq/Freq5.html

45. Q. Wang, J.E. Moser and M. Gratzel. Electrochemical Impedance Spectroscopic Analysis of Dye-Sensitized Solar Cells. *J. Phys. Chem. B* 109, 14945-14953 (2005).

46. L. Han, N. Koide, Y. Chiba and T. Mitate. Modeling of an equivalent circuit for dye-sensitized solar cells. *Appl. Phys. Lett.* 84, 2433-2435 (2004).

47. R. Kern, R. Sastrawan, J. Ferber, R. Stangl and J. Luther. Modeling and interpretation of electrical impedance spectra of dye solar cells operated under open-circuit conditions. *Electrochim. Acta* 47, 4213- 4225 (2002).

48. M. Gratzel. Conversion of sunlight to electric power by nanocrystalline dye-sensitized solar cells. *J. Photochem. Photobiol., A* 164, 3-14 (2004).

49. S. Swetha, S.M. Santhosh and R. Geetha Balakrishna. Synthesis and Comparative Study of Nano-TiO_2 Over Degussa P-25 in Disinfection of Water. *Photochem. Photobiol.* 86, 628–632 (2010).

50. W. Li, C. Ni, H. Lin, C. P. Huang and S.I. Shah. Size dependence of thermal stability of TiO_2 nanoparticles. *J. Appl. Phys.* 96, 6663-6668 (2004).

51. J. Jiu, S. Isoda, F. Wang and M. Adachi. Dye-Sensitized Solar Cells Based on Single-Crystalline TiO_2 Nanorod Films. *J. Phys. Chem. B* 110, 2087-2092 (2006).

52. M. Wei, Y. Konishi, H. Zhou, H. Sugihara and H. Arakawa. Utilization of Titanate Nanotubes as an Electrode Material in Dye-Sensitized Solar Cells. *J. Electrochem. Soc.* 153, A1232-A1236 (2006).

53. S. Chappel, S.G. Chen and A. Zaban. TiO_2-Coated Nanoporous SnO_2 Electrodes for Dye-Sensitized Solar Cells. *Langmuir* 18, 3336-3342 (2002).

54. Y. Diamant, S. Chappel, S.G. Chen, O. Melamed and A. Zaban. Core–shell nanoporous electrode for dye sensitized solar cells: the effect of shell characteristics on the electronic properties of the electrode. *Coord. Chem. Rev.* 248, 1271–1276 (2004).

55. X. Gao and I.E. Wachs. Titania-silica as catalysts: molecular structural characteristics and physico-chemical properties. *Catal. Today* 51, 233-254 (1999).

56. S.H. Lim, N. Phonthammachai, S.S. Pramana and T. J. White. Simple Route to Monodispersed Silica-Titania Core-Shell Photocatalysts. *Langmuir* 24, 6226-6231 (2008).

57. X. Li, H. Lin, J. Li, N. Wang, C. Lin and L. Zhang. Chemical sintering of graded TiO_2 film at low-temperature for flexible dye-sensitized solar cells. *J. Photochem. Photobiol., A* 195, 247–253 (2008).

58. A.V Shroff and D.L Shah. Soil Mechanics and Geotechnical Engineering. *A.A.Balkema* page 49 (2003).

59. T.M. Shaw. Liquid Redistribution during Liquid-Phase Sintering. *J. Am. Ceram. Soc.* 69, 27-34 (1986).

60. L. Qi, J. D. Sorge, and D. P. Birnie, III. Dye Sensitized Solar Cells Based on TiO_2 Coatings with Dual Size-Scale Porosity. *J. Amer. Ceram. Soc.* 92,1921-1925 (2009).

61. S. Phadke, J. Ho, and D. P. Birnie, III.Emulsion Templating to Obtain Dual-Size-Scale Mesoporous Titania Coatings. *Mater. Lett.*, 63, 2619-2621 (2009).

62. U. Bach, D. Lupo, P. Comte, J.E. Moser, F. Weissortel, J. Salbeck, H. Spreitzer and M. Gratzel. Solid-state dye-sensitized mesoporous TiO_2 solar cells with high photon-to-electron conversion efficiencies. *Nature* 395, 583-585 (1998).

63. N. Kopidakis, K.D.Benkstein, J. Lagemaat and A.J. Frank. Transport-Limited Recombination of Photocarriers in Dye-Sensitized Nanocrystalline TiO_2 Solar Cells. *J. Phys. Chem. B* 107, 11307-11315 (2003).

64. R.M. German, P. Suri, and S.J. Park. Review: liquid phase sintering. *J. Mater. Sci*. 44, 1-39 (2009).

65. A. Hanprasopwattana, S. Srinivasan, A. G. Sault, and A. K. Datye. "Titania Coatings on Monodisperse Silica Spheres (Characterization Using 2-Propanol Dehydration and TEM)" *Langmuir* 12, 3173-3179 (1996).

66. K. M. S. Khalil, A. A. Elsamahy, and M. S. Elanany. Formation and Characterization of High Surface Area Thermally Stabilized Titania/Silica Composite Materials via Hydrolysis of Titanium(IV) *tetra*-Isopropoxide in Sols of Spherical Silica Particles. *J. Colloid Interface Sci.*, 249, 359-365 (2002).

67. X. Fu and S. Qutubuddin. Synthesis of titania-coated silica nanoparticles using ono-ionic water-in-oil *Colloids Surf., A* 178, 151-156 (2001).

68. S. Ngamsinlapasathian, S. Sakulkhaemaruethai, S. Pavasupree, A. Kitiyanan, T. Sreethawong, Y. Suzuki and S. Yoshikawa. Highly Efficient dye-sensitized solar cell using nanocrystalline titania containing nanotube structure. *J. Photochem. Photobiol., A* 164, 145–151 (2004).

69. K.Y. Jung and S.B. Park. Anatase-phase titania: preparation by embedding silica and photocatalytic activity for the decomposition of trichloroethylene. *J. Photochem. Photobiol., A* 127, 117–122 (1999).

70. M.S. Lee, G.D. Lee, C.S. Ju and S.S. Hong. Preparations of nanosized TiO_2 in reverse microemulsion and their photocatalytic activity. *Sol. Energy Mater. Sol. Cells* 88, 389–401 (2005).

71. S. Hayashi, Y. Kumamoto, T. Suzuki and T. Hirai. 1991. Imaging by polystyrene latex-particles. *J. Colloid Interface Sci.* 144, 538–547 (1991).

72. Y. Xia, B. Gates, Y. Yin and Y. Lu. Monodispersed colloidal spheres: Old materials with new applications. *Adv. Mater.* 12, 693–713 (2000).

73. F. Burmeister, C. Schäfle, T. Matthes, M. Böhmisch, J. Boneberg, and P. Leiderer. Colloid Monolayers as Versatile Lithographic Masks. *Langmuir* 13, 2983-2987 (1997). .

74. T. Okubo, S. Chujo, S. Maenosono and Y. Yamaguchi. Microstructure of silica particle monolayer films formed by capillary immersion force. *J. Nanopart. Res.* 5, 111–117 (2003).

75. A.S. Dimitrov and K. Nagayama. Steady-state unidirectional convective assembling of fine particles into two-dimensional arrays. *Chem. Phys. Lett.* 243, 462–468 (1995).

76. B.G. Prevo and O.D. Velev. Controlled, rapid deposition of structured coatings from micro- and nanoparticle suspensions. *Langmuir* 20, 2099–2107 (2004).

77. J.A. Lee, L. Meng, D.J. Norris, L.E. Scriven and M. Tsapatsis. Colloidal crystal layers of hexagonal nanoplates by convective assembly. *Langmuir* 22, 5217–5219 (2006).

78. H.W. Deckman, J.H. Dunsmuir, S. Garoff, J.A. McHenry and D.G. Peiffer. Macromolecular self-organized assemblies. *J. Vac. Sci. Technol., B* 6, 333–336 (1988).

79. M. Szekeres, O. Kamalin, R.A. Schoonheydt, K. Wostyn, K. Clays, A. Persoons and I. Dekany. Ordering and optical properties of monolayers and multilayers of silica spheres deposited by the Langmuir–Blodgett method. *J. Mater. Chem.* 12, 3268–3274 (2002).

80. S. Reculusa and S. Ravaine. Synthesis of colloidal crystals of controllable thickness through the Langmuir–Blodgett technique. *Chem. Mater.* 15, 598–605 (2003).

81. C.L. Haynes, A.D. MacFarland, M.T. Smith, J.C. Hulteen and R.P. Van Duyne. Angle-resolved nanosphere lithography: manipulation of nanoparticle size, shape, and interparticle spacing. *J. Phys. Chem. B* 106, 1898–1902 (2002).

82. J.S. Ahn, P.T. Hammond, M.F. Rubner and I. Lee. Self-assembled particle monolayers on polyelectrolyte multilayers: particle size effects on formation, structure, and optical properties. *Colloids Surf., A* 259, 45–53 (2005).

83. T. Ogi, L. Balam Modesto-Lopez, F. Iskandar and K. Okuyama. Fabrication of a large area monolayer of silica particles on a sapphire substrate by a spin coating method. *Colloids Surf., A* 297, 71–78 (2007).

84. T. Ohara, Y. Matsumoto and H. Ohashi. The film formation dynamics in spin coating. *Phys. Fluids A* 1, 1949-1959 (1989).

85. A.G. Emslie, F.T. Bonner and L.G. Peck. Flow of a viscous liquid on a rotating disk. *J. Appl. Phys.* 29, 858-862 (1958).

86. S.A. Phadke. Dye sensitized solar cells with templated TiO_2 coatings. *PhD Thesis.* Rutgers, The State University of New Jersey. Page 93. 2010.

87. G. Lian, C. Thornton and M.J. Adams. A Theoretical Study of the Liquid Bridge Forces between Two Rigid Spherical Bodies. *J. Colloid Interface Sci.* 161, 138-147 (1993).

88. D. Megias-Alguacil and L.J. Gauckler. Capillary Forces Between Two Solid Spheres Linked by a Concave Liquid Bridge: Regions of Existence and Forces Mapping. *AIChE J.* 55, 1103-1109 (2009).

89. S.C. Rodner, P. Wedin, and L. Bergstrom. Effect of electrolyte and evaporation rate on the structural features of dried silica monolayer films. *Langmuir* 18 9327-9333 (2002).

90. http://rsb.info.nih.gov/ij/docs/intro.html

91. V.P. Mehrotra and K.V.S. Sastry. Pendular bond strength between unequal sized spherical particles. *Powder Technol.* 25, 203-214 (1980).

92. J.C. Melrose and G. Wallick. Exact Geometrical Parameters for Pendular Ring Fluid. *J. Phys. Chem.* 71, 3676-3678 (1967).

93. K.C. Song and S.E. Pratsinis. Synthesis of bimodally porous titania powders by hydrolysis of titanium tetraisopropoxide. *J. Mater. Res.* 15, 2322-2329 (2000).

94. K.Y. Chiu, M.H. Wong, F.T. Cheng and H.C. Man. Characterization and corrosion studies of titania-coated NiTi prepared by sol–gel technique and steam crystallization. *Appl. Surf. Sci.* 253, 6762–6768 (2007).

95. A.O. Olofinjana, J.M. Bell and A.K. Jamting. Evaluation of the mechanical properties of sol–gel-deposited titania films using ultra-micro-indentation method. *Wear* 241, 174–179 (2000).
96. G. Dagan, S. Sampath and O. Lev. Preparation and Utilization of Organically Modified Silica-Titania Photocatalysts for Decontamination of Aquatic Environments. *Chem. Mater.* 7, 446-453 (1995).

97. C. Anderson and A.J. Bard. Improved Photocatalytic Activity and Characterization of Mixed TiO_2/SiO_2 and TiO_2/Al_2O_3 Materials. *J. Phys. Chem. B* 101, 2611-2616 (1997).

98. M. Atik, P.D.L. Neto, M.A. Aegerter and L.A. Avaca. Sol-gel TiO_2-SiO_2 films as protective coatings against corrosion of 316L stainless steel in H_2SO_4 solutions. *J. Appl. Electrochem.* 25, 142-148 (1995).

99. K. Yu-Zhang, G. Boisjolly, J. Rivory, L. Kilian and C. Colliex. Characterization of TiO_2/SiO_2 multilayers by high resolution transmission electron microscopy and electron energy loss spectroscopy. *Thin Solid Films* 253, 299-302 (1994).

100. Z. Deng, E. Breval and C.G. Pantano. Colloidal sol/gel processing of ultra-low expansion TiO_2/SiO_2 glasses. *J. Non-Cryst. Solids* 100, 364-370 (1988).

101. M. Aizawa, Y. Nosaka and N. Fujii. Preparation of TiO_2-SiO_2 glass via sol-gel process containing a large amount of chlorine. *J. Non-Cryst. Solids* 168, 49-55 (1994).

102. S. Satoch, K. Susa and I. Matsuyama. Sol-gel-derived binary silica glasses with high refractive index. *J. Non-Cryst. Solids* 146, 121-128 (1992).

103. K.Y. Jung and S.B. Park. Anatase-phase titania preparation by embedding silica and photocatalytic activity for the decomposition of trichloroethylene. *J. Photochem. Photobiol., A* 127, 117-122 (1999).

104. W. Wang and M. Song. Photocatalytic activity of titania containing mesoporous SBA-15 silica. *Microporous Mesoporous Mater.* 96, 255-261 (2006).

105. J. Lagemaat, K. D. Benkstein, and A. J. Frank. Relation between Particle Coordination Number and Porosity in Nanoparticle Films: Implications to Dye-Sensitized Solar Cells. *J.Phys Chem. B* 105, 12433-12436 (2001).

CURRICULUM VITA

SUKANYA MURALI

EDUCATION

Rutgers, The State University of New Jersey, **New Brunswick, NJ**
Ph.D. Materials Science and Engineering, May 2011
M.S. Materials Science and Engineering, Jan 2009

University of Illinois at Chicago, Chicago, Illinois
M.S. Chemical Engineering, May 2003

Birla Institute of Technology and Science, Pilani, India
B.E. (Hons). Chemical Engineering, June 1999

EXPERIENCE

Rutgers, The State University of New Jersey, Piscataway, New Jersey
Research Assistant, Sep 2006-Dec2008; June 2008-August 2009; Jul 2010-May 2011
Teaching Assistant, Jan 2008-May 2008

Cabot Corporation, Albuquerque, NM
Process Development Engineer, Dec 2003-March2005

American Air Liquide, Countryside, IL
Research Assistant, May 2002-Dec2002

University of Illinois at Chicago, Chicago, IL
Graduate Assistant, Sep 2000-Apr 2002

PUBLICATIONS

S. Murali, A. Deshpande and C. G. Takoudis Modeling of the Metalorganic Chemical Vapor Deposition of Tantalum Oxide from Tantalum Ethoxide and Oxygen. *Ind. Eng. Chem. Res.*; 2005; 44(16); 6387-92